論文 / 著書情報
Article / Book Information

題目(和文)	気象予報モデルへの詳細な都市地表面パラメーターの導入が無降雨日の気象に及ぼす影響
Title(English)	The Meteorological Effects of Detailed Urban Parameter Inclusion to Weather Research and Forecasting Model on Dry Days
著者(和文)	VarquezAlvin Christopher Galang
Author(English)	Alvin Christopher Varquez
出典(和文)	学位:博士（工学）, 学位授与機関:東京工業大学, 報告番号:甲第9637号, 授与年月日:2014年9月25日, 学位の種別:課程博士, 審査員:神田　学,花岡　伸也,高木　泰士,木内　豪,中村　恭志
Citation(English)	Degree:, Conferring organization: Tokyo Institute of Technology, Report number:甲第9637号, Conferred date:2014/9/25, Degree Type:Course doctor, Examiner:,,,,
学位種別(和文)	博士論文
Type(English)	Doctoral Thesis

2014

Doctoral Dissertation

Title:
The Meteorological Effects of Detailed Urban Parameter Inclusion to Weather Research and Forecasting Model on Dry Days

---

Alvin Christopher Galang Varquez

Supervisor: Professor Manabu Kanda

Department of International Development Engineering
Tokyo Institute of Technology
Tokyo, Japan

(page intentionally left blank)

Abstract

The importance of new aerodynamic roughness parameter inclusion into weather models was investigated. Previous models, such as the Weather Research and Forecasting Model (WRF), have improved representativeness of urban areas due to urban canopy coupling. Success of previous models to simulate temperature and heat has been reported since then. However, accuracy of wind speed still needs improvement. Thus, the aim of the study is to further improve wind speed simulation in WRF using a recently proposed roughness parameterisation.

A new aerodynamic roughness parameterisation for zero-plane displacement and aerodynamic roughness length was recently derived from large-eddy simulation using real urban morphology. A nationwide database of urban parameters – derived from a combination of recently-derived parameterisation, processed urban building geometry data, and open source satellite images – were incorporated into the urban canopy model of WRF. Three major studies were conducted to validate and apply the model to real and ideal scenarios.

The first study was to test the performance of the model on a sea-breeze simulation in Kanto region. Before focusing on a specific sea-breeze event, a 2-month simulation was conducted to compare the new WRF model from the default and purely vegetation WRF model version. Statistical analysis of wind speeds reveals better accuracy in the new model than those using conventional roughness parameters. Slight overestimation in temperature was simulated in the new model due in part to the increase level of urbanisation assumed and possible misrepresentation by observation gauges. However, over-all the wind speed

improvement was found to be very significant. Focusing on the sea breeze distribution, surface drag was more apparent in the new case than in the default and vegetation cases. This large reduction of sea breeze intensity at densely built-up areas was also confirmed by a wind speed measurement network in Kanto region. Because of the surface drag from buildings, sea-breeze delay was simulated; and the new case showed better accuracy in the fronts when compared to real cloud images taken from a satellite. The sea breeze delay also reduces advection of heat above urban areas resulting to stronger mixing above urban canopies. Thus, a higher boundary layer height was simulated in the new case. This also resulted to horizontal wind speed reduction at several hundreds of meters above ground and within the boundary layer.

The second study was conducted to apply the new WRF model at other cities such as Osaka and Nagoya. Furthermore, the study also focuses on the comparison between the significance of anthropogenic heating and aerodynamic roughness. In this study, a nationwide distribution of roughness parameters and anthropogenic heat was included. The new, default, and vegetated models were used to simulate 3-days of August 2013. Near ground wind speeds were also simulated well in the new case when compared with ground observations. Differences in accuracy between the new and default model were proportional to the degree of roughness assumed in the evaluated grid. In other words, larger roughness shows better accuracy in wind speed. Further comparisons between new model and default model were conducted using simulated near ground wind speed and convergence. In Osaka, the sea breeze front becomes distorted due to the effect of buildings. Similar to the previous study, horizontal wind speed reductions were also found at

significant hundreds of meters above ground and within the boundary layer. Finally, aerodynamic roughness has a more dominant influence to near ground wind speed than aerodynamic heating. In this study, it was also found that Nagoya has a more complex atmospheric environment compared to Osaka and Tokyo because only slight improvement was found in the new case.

Lastly, an idealization of WRF was introduced to test the model's sensitivity to urban parameters. The domain was set up having a linear boundary between the sea and land. The land was assumed urban with uniform surface boundaries. Sea breeze was triggered by introducing higher temperature over land than sea. The same meteorological background with no winds as the sea breeze date and a periodic lateral boundary was applied. Sensitivity cases were conducted by varying the zero-plane displacement height, d, roughness length for momentum, z_o, and sky-view factor, SVF. From the trend of heat flux, moisture, and wind speed; it was found that z_o has the largest influence to wind speed and heat flux. The near ground wind speed is largely reduced and heat is emitted less at higher z_o. As a result, large difference in boundary layer evolution was also found. The delay in sea breeze at larger z_o resulted to a larger boundary layer height later in the day. Decreasing SVF at urban areas results to lower heat flux and lower wind speed similar but not as significant as increasing z_o. d has a similar effect to a hill and was found to have the least impact to the meteorological parameters.

Table of Contents

List of Figures and Tables

1 Introduction

1.1 Urbanization and Weather

The ratio of population at urban and rural areas has risen in the last 5 decades due to the shift from agriculture-based economy to mass industry, technology and service. By 2050, the population at urban areas is projected to double that of 2009. Approximately, urbanization has been increasing by 3% annually since 1950 (Global Health Observatory, World Health Organization). Along with increasing population, globalization promotes economic growth and overseas migration. The rise in economy corresponds to increase in work spaces like industrial and commercial buildings. The increase and shift in population also results to an increase in urban settlements such as high-rise buildings, low-rise and middle-rise residential areas. The implication of rapid urbanization to weather is tremendous.

Initially, a noticeable warming at urban areas has been observed for decades (Arakawa, 1937; Oke, 1973; Yamashita, 1994). When plotting isothermal at the urban environment, an isolated region could be form above the city referring to it as the "urban heat island". This causes various socio-economic and environmental problems. According to reports from the Intergovernmental Panel on Climate Change, heat stroke is a common occurrence during summer. Indirectly, temperature differences affect the wind and moisture circulation around and above urban areas. This leads to unexpected thunderstorms in the suburban areas, flooding, and sea breeze delays. Disease-carrying organisms could also thrive in an urban environment where moisture is stagnated due to poor ventilation. The vulnerability is high but to mitigate it is difficult because of the limited understanding and resources. Various approaches to its understanding include observation, theoretical approaches, and modelling. The approach used in this research is modelling.

1.2 Weather Modelling at Urban Areas

As an alternative to observations which can be cost-intensive and impractical in the long-term especially at developing cities, numerical weather models (NWP) are very useful in mitigation and planning. It is the mathematical approach to forecasting (Abbe, 1901). In fact as a tool of atmospheric research, modelling goes hand-in-hand with observation and theoretical studies (Warner, 2011). NWPs, with its long history, have evolved to adequately represent real environmental weather conditions (Lynch, 2008) owing to the development of sophisticated land surface models such as the Noah land surface model (Ek et al., 2003) and the urban canopy models. Along with the advancement in computational capacity and meteorological knowledge, models have been upgraded to improve performance at urban areas where vulnerability is highest (Chen et al., 2011). The motivation for doing this is because urbanization is phenomenal to modify the existing and surrounding environment (Duh et al., 2008; Changnon, Jr., 1973; Shafir and Alpert, 1989). The Weather Research and Forecasting Model (WRF) by Skamarock et al. (2005), among highly sophisticated mesoscale NWP system collaboratively designed to meet operational forecasting and atmospheric needs, provides urban physics option such as the single-layer Urban Canopy Model (UCM) of Kusaka et al. (2001) and Kusaka and Kimura (2004). The UCM is to-date the most widely used model for urban representation due to its sophisticated parameterisations without sacrificing calculation efficiency. Prior to the UCM, slab models, (Liu et al., 2006) which assume bulk values for urban parameters, were used. Details of the urban canopy model and its parameters are mentioned in the later chapters.

1.3 Sea Breeze and Urban Area Interaction

Sea breeze is generally caused by the local pressure gradient prevalent during daytime between the land and the sea. Land warms faster than the sea during daytime. The warming of land will cause air mass directly above it to mix further above. This mixing, called free convection, directly affects the height of the boundary layer, the region in the atmosphere directly influenced by the surface. The rising of air leads to a pressure drop on land. Because the temperature above the sea varies less throughout the day, the sea level pressure will remain constant. The difference in pressure between land and sea triggers the sea breeze flow. Nowadays, increased urbanization causes a non-uniform distribution of heating on land. The warmer urban areas have a tremendous effect to the sea breeze flow.

Sea breeze circulation is directly affected by urban areas since most urban areas lie very close to the land and sea boundary. Urban areas tend to affect sea breeze, thermodynamically and aerodynamically. Likewise, sea breeze also has a significant role to the atmospheric condition of urban areas. Specifically, studies have already been conducted regarding Kanto’s urban heat island and their influence on its sea breeze flow.

Sea breeze advancement can be delayed by additional heating from urban areas (Yoshikado et al., 1989; Chuan-Yao et al., 2008) and reduced nocturnal cooling. Kimura and Takahashi (1991) investigated the effects of land cover and anthropogenic heating on the surface temperature in Tokyo. Kanda et al. (2001) applied the idea further by investigating the formation of cloud lines above a major street in the Tokyo metropolitan area as a function of sea breeze convergence and urban heating. From numerical experiments, the position of cloud lines during the day was also found to be a factor in sea breeze behaviour (Inoue and Kimura, 2007). Prior to penetrating to inland regions of Kanto (e.g., Saitama and its surroundings (Fig. 1) and coastal cities such as Tokyo), the distance from the shore line acts as a heat sink, weakening sea breeze capacity, thus maintaining high temperatures inland during summer (Sato et al., 2008). This was also observed in a study conducted by Chen et al. (2011a) in the Greater Houston area of the USA. Scalar emission from urban areas also affects sea breeze flow. According to Hosoi et al. (2011), two thermal lows tend to occur in western and northern Kanto on sunny days, promoting a southerly sea breeze and transporting photochemical oxidants. This thermal low is largely influenced by urban areas triggering sea breeze penetration. Tokyo acting as an upwind area during summer influences the heat advected inland (Aoyagi). All the mentioned past mesoscale modelling in Kanto, idealized or real, were not able to fully replicate the sea breeze due to the misrepresentation of actual roughness distribution at highly urbanized cities.

Some observational studies and idealised simulations from foreign researchers have mentioned specifically the aerodynamic effect of buildings to sea breeze (Martilli, 2003; Prtenjak, 2002). Investigations in New York (Childs and Raman, 2005) and Athens (Dandou et al., 2009) sea breeze simulations using weather models obtained similar findings as above but the roughness parameters used were coarsely (or uniformly) distributed and underestimated.

1.4 Research Problem

The coarseness and underrepresentation of urban areas can be problematic in simulation of real weather. Thus, improvements which are discussed in the later chapters are still necessary. The focus of this study is on how weather models, such as WRF, can be improved especially in the aerodynamic aspect (e.g. wind field, surface drag).

Although coupling WRF and UCM improves the accuracy of simulated temperature, recent evaluation studies remain to detect overestimation of surface wind speeds at urbanized areas. Kondo et al. (2008) confirmed that urban canopy model performance depend on wind direction and consistently overestimates canopy wind speeds at an area within and almost down-wind of a highly dense area within Tokyo (values of roughness length for momentum, z_o, range from 0.5-1.0 m). Consistent overestimation were also found in a WRF/Urban model simulation over greater Paris, using single set of parameters for the whole area, regardless of planetary boundary layer schemes used (Kim et al., 2013). Although sensitive to surface type, low roughness parameter assumptions such as 0.7(1.4) – 1.6(11) m for $z_o(d)$ still overestimate wind speed based from sensitivity tests in a US-Canada border (Flagg and Taylor, 2011). Using the simple rule-of-thumb method prescribed by Burian et al. (2002), WRF coupled with the Noah land surface model and single-layer urban canopy model improves reproducibility of urban heat island on a summer day in Beijing but still slightly overestimated urban canopy wind speed compared with observed during daytime (Miao et al., 2009). Other researchers suggest other factors affecting modelled wind inaccuracies. Lee et al. (2010) noticed overestimation of wind speed and underestimation of vertical gradient of wind speed due to excessive turbulent mixing when applying WRF with urban canopy model to Houston-Galveston Metropolitan Area. Despite this, urban canopy model is still detrimental to the simulated wind speed at surface level above urban areas.

Some researches would resort to recommending more complex models such as the multi-layer urban canopy models (Martilli et al., 2002; Kondo et al., 2005; Salamanca et al., 2011). However, multi-layer urban canopy models are resource-demanding and its parameters, which are not readily available, may vary highly per location. Multi-layer schemes, when not properly set-up, may even perform worse in wind speed simulations compared to single-layer (Holt and Pullen, 2006). According to comprehensive review by Chen et al. (2011b) regarding WRF and urban canopy model coupling, initialization of state variables is still left with little attention by the urban modelling community. Further, if mesoscale models are to be used anywhere globally, simple but highly accurate parameterisation in urban canopy models is necessary. The wind speed overestimation issue above urban areas need to be addressed, first, prior to creating more complex models and applying it to highly urbanised locations.

1.5 Objectives and Originality of the Study

The main objective of this study is to improve urban representation in weather models to further understand impacts of urbanization to weather. The objectives can be subdivided to as follows:

1. To incorporate distribution of new aerodynamic roughness parameters into a numerical weather model (chapter 3);

2. To further improve parameterisation within single-layer urban canopy model (chapter 3);
3. To evaluate the performance of updated model (chapter 4);
4. To improve and understand urban roughness effects to sea breeze and wind field at major cities in Japan (chapter 5);
5. To understand how each roughness parameter and another urban parameter affect the simulation results of the numerical weather prediction model (chapter 6).

In line with this, this research has achieved the following points of originality:

1. FIRST-EVER application of new aerodynamic roughness parameters into a numerical weather prediction model coupled by the single-layer urban canopy model (chapter 4 and 5);
2. Simulation of sea breeze using nation-wide urban parameter distribution, prepared by Makabe et al. (2014), derived from real building morphology (chapter 5);
3. Modification of single-layer urban canopy model in WRF to read distributed parameters (chapter 3);
4. Better understanding of sea breeze/wind field changes at urban areas in terms of urban heating and roughness (chapter 4);
5. Comparisons of relative influence of zero-plane displacement height, aerodynamic roughness length for momentum, and sky-view factor (chapter 6).

1.6 Dissertation Outline

This chapter is succeeded by the theoretical background, followed by the discussion on the model improvements, the model validation, and application. Chapter 1 is about the introduction and problem statement. The application of weather models to urban areas and the introduction of urban-sea breeze interaction are included. Chapter 2 deals about the theoretical background relevant to the study. Dynamical downscaling, urban canopy modelling, and the aerodynamic roughness parameters, and other urban parameters are discussed. Chapter 3 is about the model building from incorporating urban geometric parameters to physics improvements. Chapter 4 discusses the testing and application of the improved WRF model on a sea breeze case in Kanto region. Chapter 5 is the expanded application of the improved WRF in a nationwide scale with focus on major cities of Tokyo, Osaka, and Nagoya. Aside from the application, chapter 6 discusses how each improvement influences the model outputs using an ideal world scenario in WRF.

2 Theoretical Background

2.1 Dynamical Downscaling

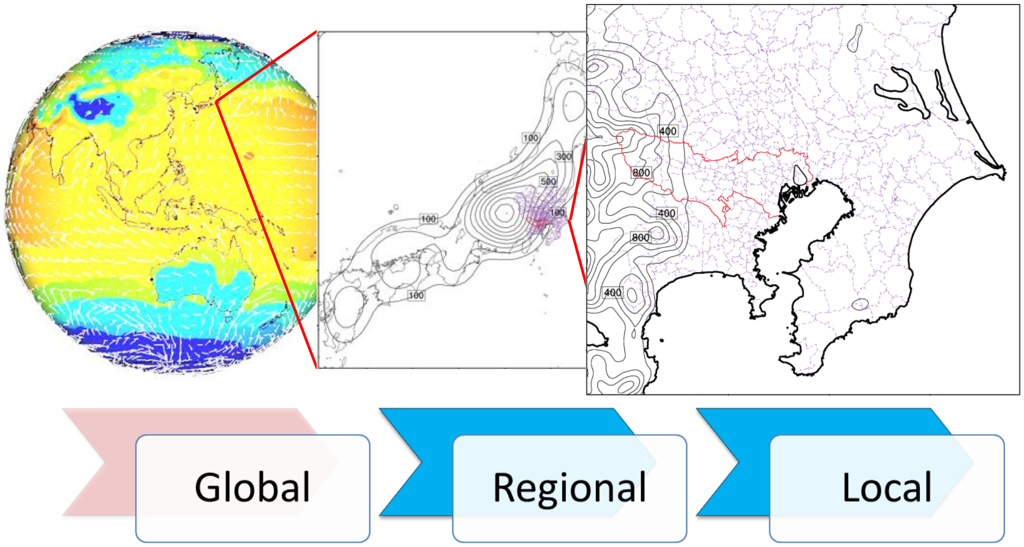

Figure 2-1 Scales of dynamical downscaling

The study of urban meteorology is conducted via numerical or observational approaches. This research involves a numerical approach specifically called regional climate downscaling. Before going deeper into this study, it is necessary for the general readers to understand briefly the concept behind downscaling. Various scales in meteorology have been introduced in the past by Orlanski (1975). Downscaling is the forecasting of small-scale features of a region, estimated from large-scale structures. The large-scale structures, often fed by temporally and spatially coarse global datasets, are used as lateral boundaries. Thus, the accuracy of regional climate models is highly dependent on the lateral boundaries. These lateral boundaries are usually in the scale of 30 arc-seconds to 1.0 degrees. Among leading source agencies of lateral boundaries are National Center for Environmental Prediction (NCEP), European Centre for Medium-Range Weather Forecasts (ECMWF), and the Japan Meteorological Agency (JMA). The large-scale structures are not necessarily simulated solely by a model but in fact derived, using assimilation methods, from external or observation sources. From the lateral boundaries, mathematical models allow the reproduction of finer scale structures. A sequence of downscaling from global to local scale is shown in Figure 2-1. The most common application of downscaling is long-term forecasting from general circulation models. The concern of urban meteorology, however, is on the understanding of mesoscale processes such as extreme rainfall and the urban heat island. The downscaling model used in this research is a well-known NWP called the Weather Research and Forecasting Model. Instead of forecasting future weather, the focus is on the improved simulation of past events, called hind-casting.

2.2 Single-layer Urban Canopy Model

As the resolution of NWP increases, the influence of the surface to the simulation results increases. In WRF, land surface schemes and urban schemes are necessary settings to parameterize the surface. For non-urban surfaces, the Noah land surface model (Tewari et al., 2008) is widely used. To consider urban surfaces, various options are available (Chen et al., 2011). Among them is the single-layer urban canopy model, henceforth called UCM, proposed by Kusaka et al. (2001) and Kusaka and Kimura (2004). This model assumes an infinitely-long street canyon (for each calculation grid) parameterized to represent urban geometry with a three-dimensional nature. The heat fluxes from the roof, wall, and ground are calculated using the widely used Monin-Obukhov similarity theory and the Jurges formula. Currently available as a default option in WRF, it was known to improve accuracy of simulated temperature at urban areas especially when coupled with the Noah land surface model. Although the UCM prescribes the condition within the urban canopy layer, its main purpose in WRF is to provide a realistic simulation of the urban boundary layer, the region above the urban canopy layer.

UCM has the following features:

1) 2-D street canyon parameterisation to represent effects of urban geometry on urban canyon heat distribution.
2) Shadowing from buildings and reflection of radiation in the canopy layer
3) Canyon orientation and diurnal cycle of solar azimuth angle
4) Man-made surface consisting of eight canyons with different orientation
5) Inoue's model for canopy flows
6) The multi-layer heat equation for the roof, wall, and road interior temperatures
7) Anthropogenic heating associated with energy consumption by human activities
8) Very thin bucket model for evaporation and runoff from road surface

Below is a list of urban parameters used in WRF (Ching et al., 2009),

- Urban fraction
- Building height
- Roughness for momentum above the urban canopy layer
- Roughness for heat above the urban canopy layer
- Zero-displacement height above the urban canopy layer
- Percentage of urban canopy

- Sky-view factor
- Building coverage ratio
- Normalized building height
- Drag coefficient by buildings
- Building volumetric parameter
- Anthropogenic heat
- Heat capacity of the roof, wall, and road
- Heat conductivity of the roof, wall, and road
- Albedo of the roof, wall, and road
- Emissivity of the roof, wall, and road
- Roughness length for momentum of the roof, wall, and road
- Roughness length for heat of the roof, wall, and road

The current UCM model, however, provides very limited assumptions for aerodynamic roughness length, displacement heights, and anthropogenic heat emission. In other words the parameters were assumed from uniform arrays, and its application unjustifiably less representative of real urban environment. The urban parameters, listed above, are read from a table in the model. In the table, parameters vary based on three urban classifications: low intensity residential, high intensity residential, and commercial districts. The default parameters in the table, which can immediately be edited by the user to suit the region of study, were based on reports of Burian and Han (2003) and Burian et al. (2003). The report was created from National Land Cover Data for the United States (NLCD) and U.S. Geological Survey (USGS).

Other versions of the urban canopy model, beyond the scope of this study, have been developed as well. One of them are the mutli-layer urban canopy models (Martilli et al., 2002; Kondo et al., 2005; Salamanca et al., 2011; Chen et al., 2011). With a more sophisticated modelling, it allows direct interaction with the planetary boundary layer schemes unlike the UCM. It considers the three-dimensional nature of urban surfaces and the vertical distribution of heat/moisture sources and sinks. Another is an improvement of the UCM developed in Princeton University, called "PUCM", which also includes the effect of vegetated surfaces in the surface energy budget (Wang et al., 2013). A comparative diagram from the UCM and multi-layer urban canopy models are shown in Figure 2-2.

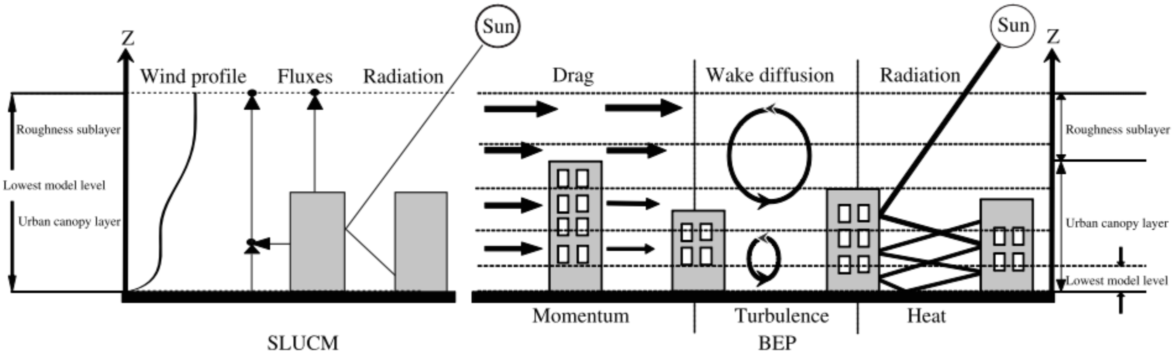

Figure 2-2 A schematic of the single-layer urban canopy model (represented by SLUCM) and mutli-layer urban canopy model (represented by BEP) acquired from Chen et al. (2011)

A sensitivity study of using a distribution of the parameters above for Houston, Texas was conducted by Salamanca et al. (2011) using the multi-layer urban canopy models. Distributed (nationwide) urban parameter testing using the single-layer urban canopy model is yet to be conducted with up-to-date aerodynamic roughness paremeterisations.

2.3 Aerodynamic Roughness Parameterisation

2.3.1 Definition

To appreciate the concept of aerodynamic roughness, its background importance is discussed. Near the surface, the atmosphere is subjected to various forcings. The lowest layer of the atmosphere directly affected by the surface is commonly referred to as the planetary boundary layer (or atmospheric boundary layer). This layer can be visible on a clear day and characterized by strong mixing (e.g. pollutants, cloud formations) above cities. Occasionally, the layer can be judged visually from the clear separation of pollutants a few hundreds to a kilometre near the surface. On cloudy days, the height is commonly estimated from the bottom of the clouds. The evolution of the boundary layer is affected by two types of convection: free and forced. Free convection is the rise of heated air from the surface. Forced convection, two-dimensional in nature, is the result of the drag effect of surfaces to winds. The drag is brought about by the shape of roughness elements above the ground. Examples of these roughness elements near the surface are gravity waves, grass, trees, and man-made structures. The rougher the surface, the more turbulent the urban boundary layer becomes thus contributing to the whole boundary layer.

The drag can be visualized using the wind profile. The profile, logarithmic in form, is related to the transport of momentum and heat from the surroundings. In neighbourhood scale, the drag can be measured directly when realistic urban geometry is used. However in mesoscale simulations where urban geometry cannot be resolved explicitly, aerodynamic roughness parameterisation is needed. In urban boundary layer, aerodynamic roughness length for momentum, z_o, and zero-plane displacement height, d, are the necessary roughness parameters. The logarithmic wind profile applicable to the urban boundary layer can be generalized by the equation,

$$u = \frac{u*}{k}\left[ln\left(\frac{z-d}{z_o}\right) + \phi \right], \tag{1}$$

where u is the horizontal wind speed, $u*$ is the friction velocity, k is the Von Karman constant, z is the elevation from ground, and ϕ is the stability parameter function. ϕ is zero under neutral conditions.

The definition of d and z_o can be understood from eqn. 1. The displacement height, d, determines the contributed effect of roughness elements to displace the surface of the logarithmic wind upward within a grid. For example, trees packed close enough will appear like a displaced surface from above. Similarly, building density influences the height of the displaced wind profile. This is the reason why d is subtracted to z. On the other hand, z_o, smaller in magnitude than d and actual roughness elements, is the parameter that affects the shape of the wind profile. Traditionally, it is determined by extrapolating the measured logarithmic wind profile to zero when plotted on a semi-log graph.

It is to be noted that the large d and z_o in some locations do not necessarily mean zero wind values inside the canopy. The actual winds within the canopy layer (close to average building heights) are much more complicated and would require higher resolution model to resolve the values realistically. For the purpose of this study, the d and z_o are used in the UCM to prescribe the winds above the urban canopy layer (or within the urban boundary layer).

WRF is capable in simulating wind and temperature values within the urban canopy layer diagnostically using the Monin-Obukhov similarity theory. These diagnostic parameters are representative of the assumed urban canopy layer configuration in the grid and useful for practical applications.

2.3.2 Building Database Construction

The building parameters used to derive the roughness parameters are initially discussed. Makabe et al. (2014) created a 1-km spatial resolution database of building height from a Geographic Information System (GIS) dataset. The dataset provided by the Environmental Systems Research Institute, Inc. (ESRI) contains building floor information together with the area occupied by the building in vector format in 0.05 arc seconds (approximately 1.5 m). Assuming 4 m floor height, the heights were estimated. The data was grouped into meshes (approximately 1 km per side) and building statistics were derived which is defined later in the chapter 3. The following information were also provided in the database:

a. average building height (units in meters), H_{ave}
b. maximum building height, H_{max}
c. standard deviation of building heights, σ_H
d. plane area index, λ_p
e. frontal area index, λ_f

H_{ave} is the average height of all buildings within the grid. H_{max} is the height of the tallest building within the grid. σ_H is the standard deviation of all heights of buildings within the grid. λ_p is a dimensionless parameters defined as the fraction of area occupied by buildings within a grid. To put it simply, it determines how much of the area is covered by the buildings. On the other hand, λ_f is calculated from the frontal area of all the buildings divided by the total grid area. The frontal area here is assumed to be oriented along the direction wind. From this definition, λ_f contributes to how much of an incoming wind is affected by the buildings. Ideally, this value varies with wind direction but current WRF only considers one value, averaged for 8 directions.

2.3.3 Roughness Parameter Derivation

The aerodynamic roughness parameters, roughness length for momentum and displacement height are essential canopy parameters for accurate wind field distribution. The method discussed here only applies to buildings. Various methodologies for estimating the roughness parameters used in urban canopy models (for other urban parameters refer to p. 10) have been extensively reviewed by Grimmond and Oke (1999). Derived from experiments using simple building arrays, previous parameterisations were proven to account for larger heat storage of cities but do not physically estimate the drag due to complex urban morphology. In terms of urban canopy modelling in standard WRF, assumed z_o and d is still estimated using the conventional parameterisations (Burian et al., 2002; Burian and Ching, 2009; Macdonald et al., 1998, henceforth denoted as MD1998) leading to the issue mentioned earlier. A new aerodynamic roughness parameterisation recently introduced by Kanda et al. (2013), henceforth denoted as KA2013, is proposed for integration with the urban canopy model. The highlight of this new parameterisation is in the sophistication and straightforwardness of estimating d and z_o. The formulated equation was derived from a large eddy simulation using real building configurations in Tokyo and

Nagoya. The recent method provides more representative and pronounced feedback from *d* and z_o values.

The difference between KA2013 and MD1998 lies in the consideration of two gridded parameters, H_{max} and σ_H, for the calculation of *d* and z_o. In the default single-layer urban canopy model, the equations for *d* and z_o are calculated as follows according to MD1998;

$$\frac{d(\mathrm{mac})}{H_{ave}} = 1 + A^{-\lambda_p}\left(\lambda_p - 1\right), \tag{2}$$

$$\frac{z_o(\mathrm{mac})}{H_{ave}} = \left(1 - \frac{d}{H_{ave}}\right)\exp\left[-\left\{0.5\beta\frac{C_{\mathrm{lb}}}{\kappa^2}\left(1 - \frac{d}{H_{ave}}\right)\lambda_f\right\}^{-0.5}\right], \tag{3}$$

where *A* and β are experimental constant with values of 4.43 and 1.0, respectively, C_{lb} = 1.2 is the drag coefficient of an obstacle, and κ = 0.4 is the von Karman constant, for building arrays with uniform height.

KA2013 expands the parameterisation further to accommodate variability in building heights through

$$\frac{d}{H_{max}} = c_0 X^2 + (a_0 \lambda_P{}^{b_0} - c_0)X\ , \tag{4a}$$

where *d* is the proposed displacement height, *X* as

$$X = \left(\frac{\sigma_H + H_{ave}}{H_{max}}\right),\ 0 \le X \le 1.0\,, \tag{4b}$$

and a_0, b_0, and c_0 are the dimensionless regressed constant parameters, i.e., 1.29, 0.36, and -0.17, respectively. Eqn. 4a also provides displacement height for regularly arrayed cubes at the upper limit of $X = 1$ as,

$$\frac{d}{H_{\max}} = \frac{d}{H_{ave}} = a_0 \lambda_P{}^{b_0} , \tag{4c}$$

The roughness length for momentum, z_o, is estimated using

$$\frac{z_o}{z_o(mac)} = b_1 Y^2 + c_1 Y + a_1 , \tag{5}$$

where a_1, b_1 and c_1 are the dimensionless regressed constant parameters, i.e., 0.7076, 20.2067, and -0.7711, respectively. Y is estimated by

$$Y = \left(\frac{\lambda_P \sigma_H}{H_{ave}} \right), \; 0 \le Y , \tag{6}$$

which also provides z_o for regularly arrayed cubes at lower limit of $Y = 0$ as,

$$\frac{z_o}{z_o(mac)} = a_1 \tag{7}$$

Based from the findings of the large eddy simulations conducted by KA2013 method, the value for their proposed d is slightly larger than MD1998 when height variability within grids is not considered. Furthermore, neglecting height variability results to a smaller z_o (by a factor of a_1) in the KA2013 method. Most often, KA2013 results to larger roughness parameter values when height variability, represented by H_{max} and σ_H, is considered. Influence of each geometrical parameter can be found in Appendix A.

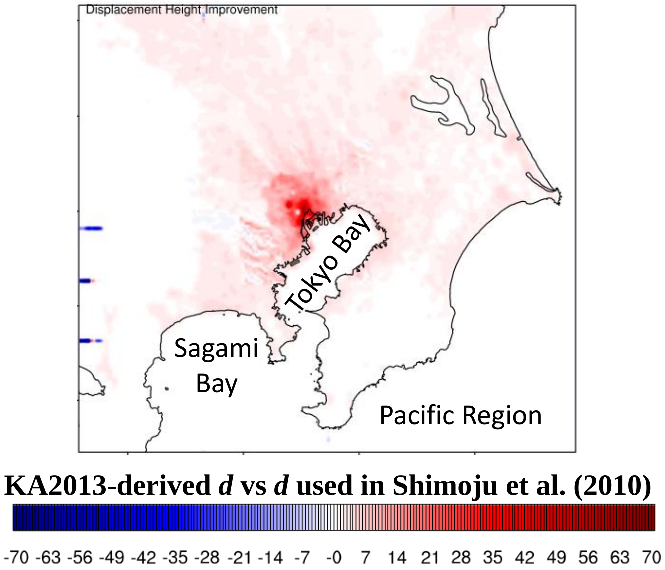

Figure 2-3 Comparison of zero-plane displacement height used in this study to previously used distribution

Shimoju et al. (2010) was able to incorporate a distribution of *d* using the MD1998 into the WRF model. Comparing with their previously derived distribution, the *d* used in this study is much larger than previously used, as shown in Figure 2-3. Further, no distribution of z_o was considered in WRF simulations in Japan prior to this study.

2.4 Other Urban Parameters

Necessary urban parameters, also mentioned later, are defined briefly below:

- Anthropogenic heat emission

The additional heat emitted by urban areas due to anthropogenic activity. This can come from many sources such as car combustion, air conditioning, heating, and so on. In this paper, it was estimated from the hourly energy consumption.

- Roughness length for heat

The aerodynamic heat transport parameter, proportional to roughness length for momentum. This parameter directly influences the heat transfer coefficient used in the urban canopy model.

- Sky-view factor

The visible fraction of the sky viewed from a reference point from the ground. This parameter influences the amount of radiation trapped within the canopy. Actual sky-view factor is difficult to be calculated in WRF since building configurations are not explicitly resolved. This can be empirically estimated from the λ_p and λ_f.

- Urban fraction

The fraction of the urban areas within a grid. Unlike the λ_p where only the buildings are considered, this parameter considers all anthropogenic elements (e.g. roads and buildings). The urban fraction was depends on the input land use classification. Within a grid, various land use information (e.g. water bodies, urban, croplands, grasslands, mixed forests, savanna) are available. The urban fraction can be calculated by dividing the area assigned urban over the total area of the grid. This parameter determines the percent contribution of the urban areas to momentum and heat exchange within the grid.

2.5 Chapter Summary

In this chapter, dynamical downscaling and single-layer urban canopy model are discussed. These background concepts are essential since this study revolves entirely on their usage and modifications. The roughness parameters were then introduced along with its database construction. Finally, brief descriptions of other essential parameters were provided.

3 Model Description and Improvement

3.1 Weather Research and Forecasting Model

The Weather Research and Forecasting Model (WRF) by Skamarock et al. (2005) is a highly sophisticated mesoscale model collaboratively designed to meet operational forecasting and atmospheric needs. The version of WRF used in the lab was initially improved to accommodate distributed anthropogenic heat emission data. Originally, WRF has two dynamical cores defining the governing equations formulation, prognostic variables, horizontal and vertical gridding, terrain formulation, time integration method, and spatial discretization. They are the WRF Nonhydrostatic Mesoscale Model and the Advanced Weather Research and Forecasting Model (ARW). The difference between two dynamical cores is not of concern for this study. Due to its wide usage and popularity, ARW (version 3.3.1) is equivalent to the WRF used in this dissertation. Similar to all mesoscale models, below are some limitations of WRF and the reason why parameterisations are necessary:

- Weather features smaller than the grid size, such as spatial heterogeneity of meteorological fields, cannot be resolved. Usual grid size is usually larger than 1 km.
- The resolution of topography is also dependent on the grid spacing. In other words, if a grid is selected much larger than Mt. Fuji, the grid will not be able to accurately resolve the height of Mt. Fuji. This condition also applies to roughness.
- Turbulence and individual cumulus clouds cannot be explicitly resolved.

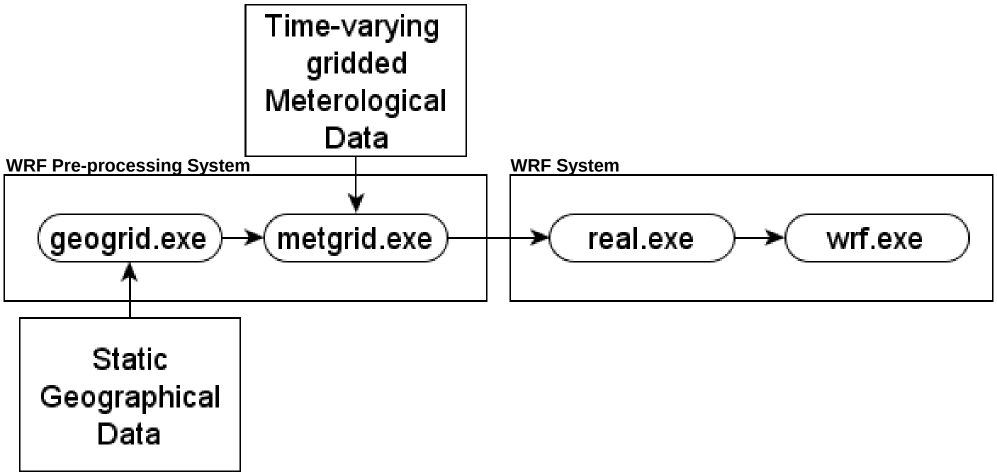

Figure 3-1 Flowchart of WRF simulation

WRF was improved further to accommodate distributed anthropogenic heat emission which was directly added into the planetary boundary layer scheme. This method had been employed by in the studies of Shimoju et al. (2010) and Nakano et al. (2013). This version of WRF, where distributed anthropogenic heat emission is included, will be referred to as the default version compared in this study.

A basic understanding of the relevant aspects of the WRF model is necessary. Running WRF has two essential components: the WRF pre-processing software (WPS) system and the WRF system (Figure 3-1). They are called “systems” because within them are uniquely sourced executable files interacting with each other. Inside the WPS system, geogrid.exe processes the static input boundaries (e.g. land use, vegetation fraction, topography) by interpolating them to the desired resolution and size of domain. The urban fraction is also calculated in the geogrid.exe. The metgrid.exe combines the output of the geogrid.exe and processes the time-dependent global meteorological inputs (e.g. pressure distribution, sea surface temperature) suitable to the desired resolution and size of domain. The outputs of the metgrid.exe, at low time-resolution, will be processed by real.exe as a final step prior to running the wrf.exe. The individual metgrid.exe outputs will be combined as a time-varying lateral boundary (only for the parent domain) and surface boundaries for all domains. Finally, the wrf.exe reads the result from real.exe and simulates the weather based on the desired physics, dynamics, and boundaries.

Most of the improvements in this study are on the static geographical data and the UCM physics contained in the WRF system. Section 3.2 talks about the aerodynamic roughness parameters inclusion as a static input. Section 3.3 talks about necessary changes in the UCM to optimize the usage of the aerodynamic roughness parameters.

3.2 Incorporating New Aerodynamic Roughness Parameters

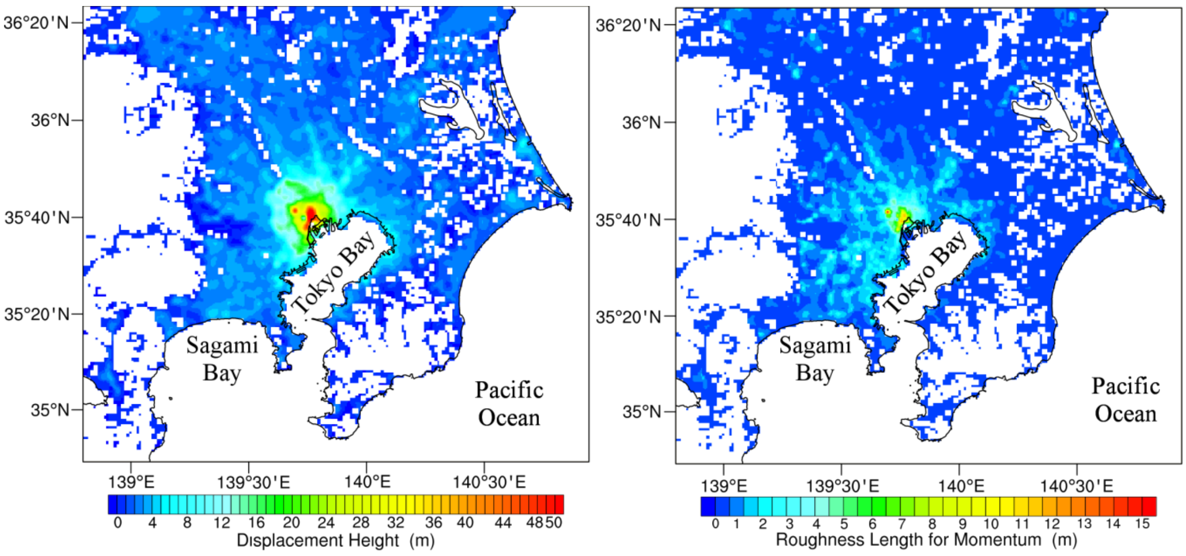

Figure 3-2 Estimated displacement height, *d* (Left), and roughness length for momentum, z_o (Right). Water bodies and areas with missing information are filled in white.

The following gridded urban parameters with 1 km resolution, which are recommended for our purpose, can easily be estimated for cities with readily available high-resolution building morphology data prepared by Makabe et al. (2014).

The parameters listed in section 2.3.2 were used to derive the distribution of d and z_o from eqn. 4c and 5. Static d and z_o were estimated for urban areas Central Japan, as shown in Figure 3-2. Compared with the commonly used estimation from MD1998, the updated d was approximately three times larger at densely built-up areas. The maximum d (74.20 m) and z_o (17.34 m) were found solely in Shinjuku district, which has the most number of skyscrapers within the 23 wards. Table 4-1 summarises the substituted fixed parameters used in the urban canopy model for the default WRF model. The derived parameters from the were read directly into the urban canopy model, except for d. When applying WRF to urban meteorology, the first atmospheric level as close as possible to the surface is preferred. Approximately 30 m first atmospheric level height above ground was suitable to justify a 1.2 km horizontal grid spacing for the second domain. This level is also high enough not to fall within most buildings heights of the selected domain. However, the d, derived from the new aerodynamic parameterisation, for some highly urbanised grids tend to be larger than 50 m, which may potentially cause some issues when a very low first atmospheric level used. To avoid this problem, d was added directly to the model topography. To avoid redundancy of d, the displacement height considered in the urban canopy model was set to zero. This approach is based on the assumption that within the urban canyon, wind speed and ambient temperature is constant. The validity of this assumption is discussed later.

The derived distribution were written in geogrid binary format (refer to section 3.1) as a static input. The specific methodology can be found in the WRF user manual or through the online tutorial,

http://www2.mmm.ucar.edu/wrf/users/docs/user_guide_V3/users_guide_chap3.htm#_Writing_Static_Data

3.3 Additional Modifications in the Single-Layer Urban Canopy Model

The changes discussed in the succeeding sub-sections were also deemed necessary to accommodate the bulk roughness parameters. The following improvements were based on previous researches and have much less impact to the model than the aerodynamic roughness parameter distribution.

3.3.1 Bulk Transfer Coefficient Revision

The default urban canopy model relies on two z_o values, for the roof and the canyon. Both are calculated from fixed building morphology using the method of Macdonald et al. (1998). Because the urban parameters were fixed depending on the default building classification, two fixed values were assigned for a homogeneous classification. For example, in high-density residential areas, z_o values of 0.13 m and 0.33 m were used for the roof and canopy, respectively. Consequently, the local bulk transfer coefficients for the roof and canyon were also calculated separately (Chen et al., 1997).

New aerodynamic parameters were derived to represent the canopy as a whole, disregarding the individual effects of the roof and canyon. For consistency in applying the distributed z_o, a top-down scheme (Kanda et al., 2005) was employed wherein the surface layer bulk transfer was estimated and used to calculate, via weighted averaging, the transfer coefficients for each individual surface (roof, wall, and ground). This scheme is valid for applications generally focused on the surface layer at the mesoscale.

3.3.2 Modified Urban Fraction

The accuracy of urban fraction in a calculation grid is also critical for simulation accuracy (Lo et al., 2007). The urban fraction (*urb_frc*) is related to the resolution of land use category. By default, urban canopy model is employed for urban dominant grids. In this case, the grid will assume three possible *urb_frc* values, (0.5, 0.9 and 0.95, as specified in the urban parameter table of WRF), depending on the assigned building classification for the grid. Excess of the assigned *urb_frc* (i.e. 1.0 – *urb_*frc) is automatically assigned cropland/grassland category and will be handled by the land use model. For non-urban dominant calculation grids, only the dominant category was considered and other categories which can be present are disregarded. Each land use category assumes various parameter values when distribution is not available. A few examples of the parameters used in the land surface models available for each internationally recognised land use category are roughness length of momentum, green vegetation fraction, albedo, leaf area index, and emissivity – the accuracy of these assumptions is beyond the concern of this study.

The simulations conducted in this study use a 100 m resolution 15 category land-use scheme from the National Land Numerical Information adjusted to match the standard U.S. Geological Survey land use. Due to its high spatial resolution, determining a more precise land use fraction, as well as *urb_frc*, was possible. Thus, calling the urban canopy model subroutine no longer relies mainly on the dominant category but instead on the actual calculated *urb_frc*. In other words, grids will use the actual fraction calculated from the land use category and, likewise, proportion the influence of both urban canopy model and land use model in the grid. Since 100 m is not enough to accommodate vegetation within urban spaces (which is approximately equal to 0.10 according to local government measurements in Tokyo), an *urb_frc* upper limit and vegetation fraction (*veg_frc*) of 0.9 and 0.1 were set, respectively.

In addition to using actual land use fractions, a second dominant land use category scheme was introduced for grids with *urb_frc* > 0. The reason behind this was to ensure that the energy and momentum flux contribution of other land use categories are considered in a calculation grid. This was achieved considering only the urban category, most dominant, and second dominant land use categories for each grid. First, the grid is classified as urban dominant (*urb_frc* > other land use factors) or non-urban dominant (other land use factors > *urb_frc*). If a grid is urban dominant, only the area occupied by urban and the area occupied by the next dominant land use category were considered. For non-urban dominant grids, only the area of the most dominant land-use category and the urban area were considered. The ratio of *urb_frc* to the sum of the *urb_frc* and the other considered land use category affects how much the urban canopy model contributes to the surface fluxes in the grid. The other land use category is handled by the land surface model as mentioned earlier.

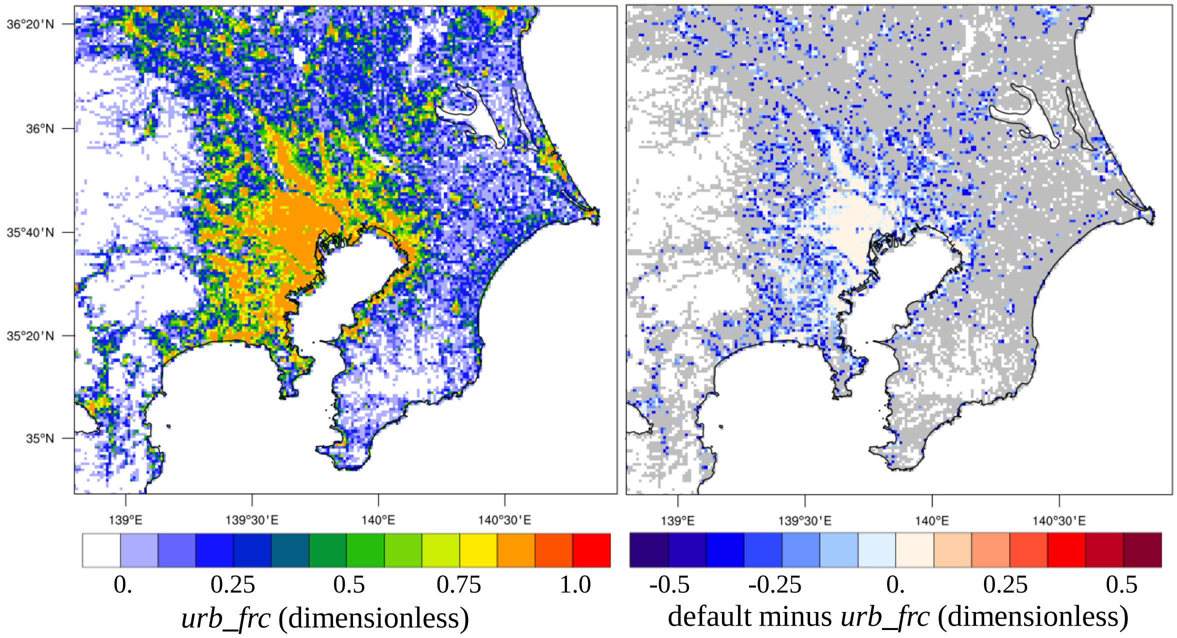

Figure 3-3 The modified urban fraction, *urb_frc* (Left). The difference between the default urban fraction (0.90) at urban dominant grids and *urb_frc* (Right). Grey represents non-urban dominant grids.

There were two advantages to this procedure compared with default WRF. First, the effect of other land use category in urban dominant grids was considered (Figure 3-3); likewise, the urban contribution to fluxes from the *urb_frc* in non-urban dominant grids was also considered.

3.3.3 Consideration of 3-D Urban Surfaces

To a certain extent, 2-D urban canopy features is inconsistent with the new 3-D surface-derived feedback parameters. As a supplement to using 3-D-generated roughness parameters, a gridded sky-view factor was also introduced and calculated based on H_{ave}, λ_p, and λ_f, using an equation regressed from a highly accurate 3-D scheme (Kanda et al., 2005a).

Because the equation assumed infinitely long street canyons, the parameterisation of sky-view factor was consistent with the default model's sky-view factor definition. The sky-view factor, from the floor to the sky, determined the amount of total solar radiation reaching the wall and ground within the canopy. λ_p is also essential because the direct solar radiation was evaluated from a weighted average according to the relative area of different canyons. The diffuse solar and downward longwave radiation values were assumed to be isotropic.

The algorithm to calculate the sky-view factor was included in the urban module in the wrf.exe (refer to p. 22). Because of this, λ_p and λ_f are necessary static inputs similar to the d and z_o. The distributed sky-view factor in Kanto region is shown in Figure 3-4. Large values, signifying areas with more radiation exchange between atmosphere and ground, are at the suburbs and at reclaimed areas on Tokyo bay. Consequently, small values are found at the Tokyo metropolitan area, Chiba, and Kanagawa.

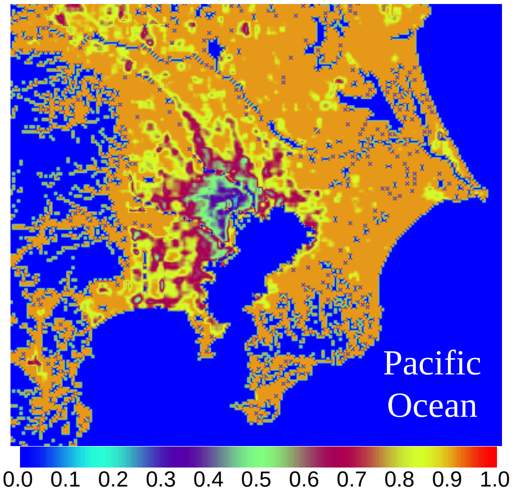

Figure 3-4 1-km gridded sky-view factor derived for Kanto region following Kanda et al. (2005). Blue areas have missing or zero values.

The differences of the assumed sky-view factors between the proposed WRF model and the default WRF model for major cities throughout Japan are shown in Figure 3-5. Default setting tends to overestimate the sky-view factor at the city centers but underestimate it at the outskirts (Figure 3-5). In spite the widening of urban area being considered at non-urban dominant grids, the over-all effect of sky-view factor improvements is not as significant to roughness – where a totally new aerodynamic roughness parameterisation is introduced. The large sky-view factors (> 0.9) shown at non-urban dominant grids suggest the urban area’s capacity (at non-urban dominant areas) to trap radiation is similar to rural grids (i.e. has an almost negligible effect). However, differences can be seen at urban dominant grids. Default assumes a uniform value of 0.48 as a sky-view factor at urban dominant grids. It results in the underestimation of radiation trapping within the city center and overestimation at the suburbs. An idealized case is presented in chapter 6 to assess the model’s sensitivity to the sky-view factor.

A direct comparison between the 2-dimensional assumption and 3-dimensional corrected sky-view factor is available in appendix B (not used in this study).

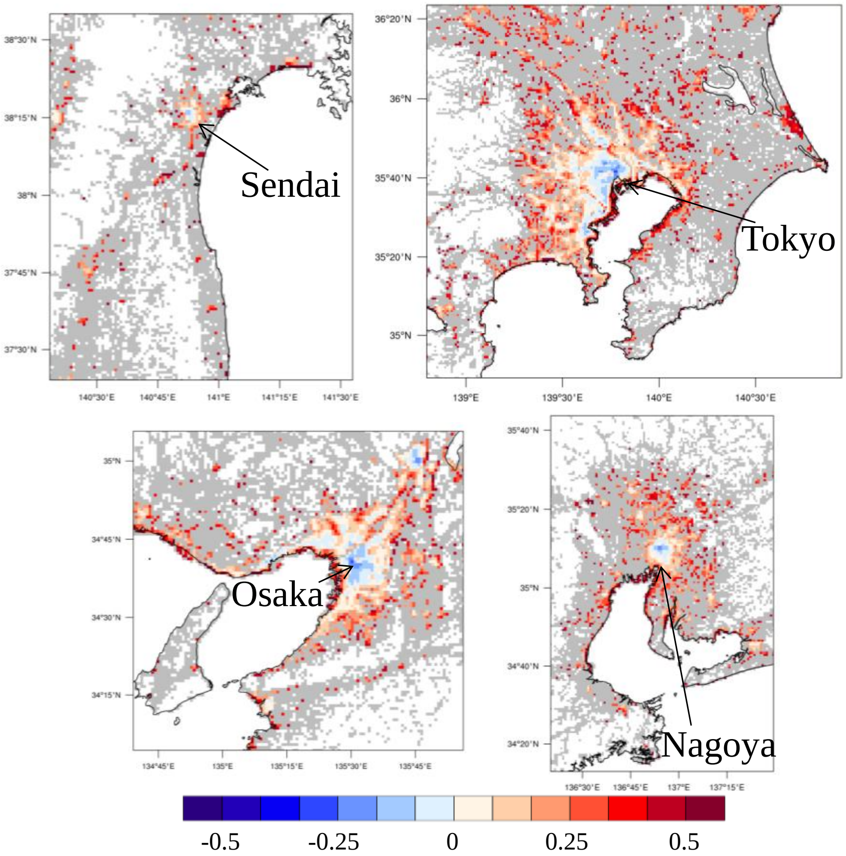

Figure 3-5 Sky-view factor difference between proposed WRF model and default WRF model. Red shows underestimation of default WRF. Blue shows overestimation of default WRF. Grey-fill shows non-urban dominant grids with urban fraction greater than 0 (i.e. no urban effect calculated in the default WRF).

3.3.4 Vegetation Effect on Transfer Coefficients

The roughness length for heat is parameterised by default as a function of the roughness length for momentum. This function utilizes on the Reynolds number, z_o. and roughness length for heat to estimate the transfer coefficient. Kawai et al. (2009) introduced an updated parameterisation of roughness length for heat, which considers the advection effect, or the enhancement of the transfer coefficients due to vegetation. This updated parameterisation was included into the urban canopy model along with the inclusion of a high spatial resolution vegetation fraction.

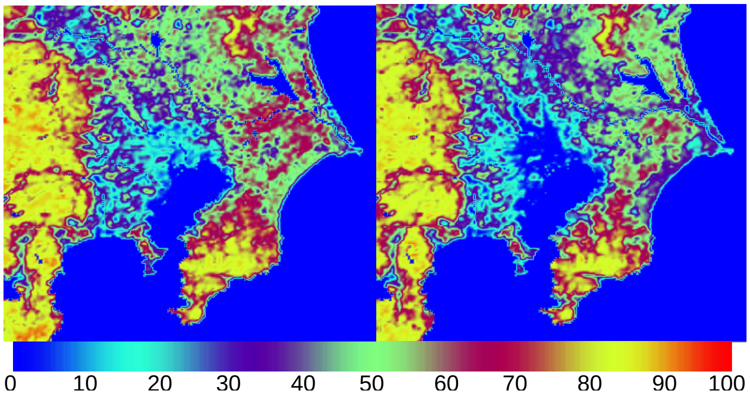

Figure 3-6 Input vegetation fraction for August (left) and September (right). Blue areas have zero or missing values.

A 1 km distribution of vegetation fraction (or greenness fraction in other literatures) was derived for the year 2011 from the NASA MODIS global vegetation indices data product using the method of Carlson and Ripley (1997). The vegetation index used was the Normalized Difference Vegetation Index (NDVI) which provided the monthly input of vegetation fraction. This is an improvement from the low-resolution vegetation fraction provided in the earlier versions of WRF. The updated vegetation fractions for August and September are shown. A minimum value of 10% at urban areas was set to accommodate urban greenery. This value is common for Tokyo urban vegetation not captured in MODIS.

3.4 Chapter Summary

This chapter contains the details of the WRF, its flow, limitations, and improvement. The incorporation of the distribution of the new aerodynamic roughness parameters, introduced in chapter 2, to the WRF is discussed. The displacement height was added to the ground topography while the roughness length for momentum was read directly in the urban canopy model. Additional improvements in the single-layer urban canopy model were also conducted. These improvements consider other updates to parameters such as roughness length for heat and sky-view factor. Finally, these improvements were necessary for successful implementation of distributed parameters.

4 Impact of A Distribution of Improved Roughness Parameterisation on a Sea-Breeze Simulation

Most of the bulk of this research was on the application of modified WRF model into a sea breeze circulation on September 14, 2011. A highest spatial resolution of 1.2 km allowed us to resolve the roughness distribution in detail. Further, the analysis was conducted for every 5 min interval.

4.1 Numerical Settings

Except for the large domain simulation in the last chapter, all simulations were conducted using 64 cores of the TSUBAME 2.0 parallelized supercomputing system (Matsuoka, 2007).

Two types of simulations were conducted with three cases for each. The first type covers a two-month simulation for validation purposed; and the second type is a simulation mainly focusing on analysing the target sea breeze. The two-month simulation was used to validate the model before focusing on the sea breeze day. The two-month simulation covers August 1 to September 30, 2011. Outputs were provided at hourly intervals. This was enough for comparison with observation. The selected months, when the target sea breeze occurred, represent peak of summer in Central Japan. Summer of 2011 was comprised of squalls, strong winds, and extreme temperature conditions, occasionally exceeding 38° C, throughout the country.

For the second simulation, September 14, 2011 was set as the target date with a one day spin-up period. The spin-up period is typical for WRF applications. Variables were simulated at 5 min intervals to understand the sea breeze behaviour in detail. During the target day, a sea breeze front was clearly observed from ground stations and satellite cloud images in Tokyo at around 1100 LST before it converged inland of Tokyo later in the afternoon. This mesoscale wind circulation is common in Central Japan during summer. A detailed classification of the weather patterns in Central Japan is presented in Khiem et al. (2010). The topography in Central Japan is relatively flat, with increasing altitude to the north and west.

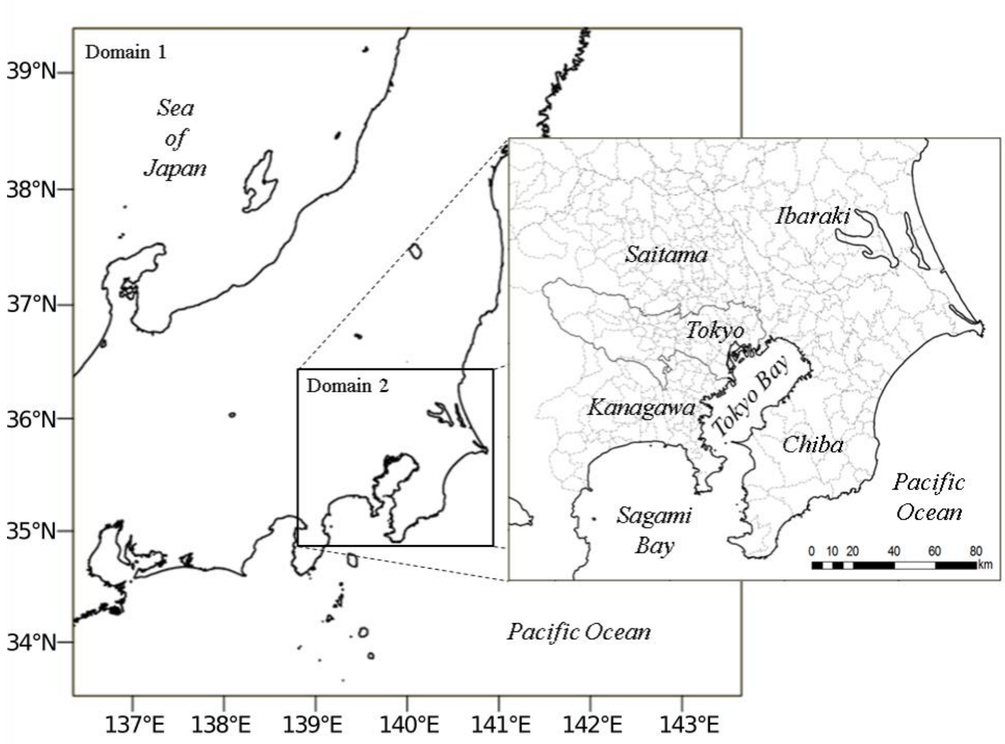

Figure 4-1 WRF Simulation domains and geographical boundaries for September 2011 simulation focused on Kanto Region.

Figure 4-1 and Table 4-1 highlight the domains and the relevant WRF simulation case settings, respectively. These settings were used by the two types of simulation mentioned earlier. The distribution of roughness parameters prepared was interpolated to match the model grid locations via nearest neighbour scheme. Three simulation cases were conducted in this study. All cases use two-way nesting, the same physics settings and meteorological boundaries. In the control case, the default WRF Version 3.3.1, was used. This case is named CTL. The case using newly modified WRF, which considers all improvements mentioned in p. 26, is named NEW. Both the CTL and NEW also included diurnal anthropogenic heat and vapour emissions based on the method of Moriwaki et al. (2008) to limit urban effect to aerodynamic roughness. The anthropogenic emissions were released at the first atmospheric level without being involved in the urban canopy model. The supplementary case refers to the vegetation case in which the default WRF was used with all urban grids revised to the grassland category. A vegetation case, named VEG, was necessary to clarify the urban effects with respect to both the default and modified WRF version.

All cases use the same meteorological boundaries and physics options. Japan Meteorological Agency's 3-hr Nonhydrostatic Mesoscale Model with 0.1 by 0.125 degrees spatial resolution for the atmospheric level and 0.05 by 0.635 degrees resolution for the surface level was used. Lack of input skin temperature, soil temperature and moisture was compensated by the 6-hr National Centre for Environmental Prediction FNL Operational Model Global Tropospheric Analyses. 1-km resolution MODIS vegetation fraction and MODIS Sea Surface Temperature was used. New Thompson et al. Scheme was used as microphysics. Rapid Radiative Transfer Model was used for the longwave radiation physics.

Table 4-1 WRF Numerical Parameters

Parameters	**CASES**		
Case ID	**CTL**	**NEW**	**VEG**
WRV Version	Default WRF Version 3.3.1	Modified WRF Version 3.3.1	Default WRF with all urban land use category replaced to grassland (no UCM)
Roughness Lengths	Fixed (0.33 m) UCM* default	Distributed z_o	
Displacement Height	Fixed (5.71 m) UCM default	Distributed *d*	
Urban Fraction	Fixed (0.90)	Modified Urban Fraction	
Plane Area Index	Fixed (0.5) UCM default	Distributed PAI	
Frontal Area Index	Fixed (0.4) UCM default	Distributed FAI	
Sky View Factor	Fixed (from PAI and FAI)	Distributed (from PAI and FAI)	
Parameters	**DOMAINS**		
ID	Domain 1	Domain 2	
spatial resolution	4.8 km	1.2 km	
east-west grid no.	171 grids	201 grids	
south-north grid no.	171 grids	181 grids	
metgrid vertical levels	17 levs	17 levs	
wrfinput vertical levels	28 levs	28 levs	
Full eta levels	1, 0.993, 0.983, 0.970, 0.954, 0.934, 0.909, 0.880, 0.837, 0.795, 0.752, 0.709, 0.633, 0.563, 0.499, 0.439, 0.384, 0.334, 0.288, 0.246, 0.207, 0.172, 0.139, 0.110, 0.083, 0.059, 0.037, 0.018, 0.		

* UCM stands for the single-layer urban canopy model incorporated in WRF

Goddard shortwave was used for the shortwave radiation. MM5 similarity was used for the surface layer. Noah Land Surface Model was used for the land surface. Single-layer urban canopy model was used for the urban surface. Mellor-Yamada Nakanishi and Niino Level 2.5 was used for the planetary boundary layer, and; Kain-Fritsch scheme was used for the cumulus parameterisation.

4.2 Model Validation

The focused meteorological parameters are wind speed, wind direction, and temperature. When discussing wind direction, show the differences in the development of the ambient winds, sea breeze wind direction in Sagami bay and Tokyo bay.

All cases were compared with observations from JMA Automated Meteorological Data Acquisition System (AMeDAS) stations using a separate 2-month simulation covering the summer period of August 1 to September 30, 2011. Hourly outputs were generated. The observation points selected for validation are shown in Figure 4-2. The selection of the observation gauges was based on the data availability and the path of the sea breeze coming from Sagami bay and Tokyo bay. To understand the effect of the aerodynamic roughness parameters, most of the points were selected in highly built up environments. Indices of *U* represents urbanised areas with urban fraction = 0.90. *R1*, *R2*, *R3*, and *R4*, corresponding to slightly urbanised grids, correspond to urban fraction of 0.24, 0.73, 0.22, and 0.55, respectively. *U1* was located in a densely built-up district of Tokyo, and was directly along the path of the sea breeze from Tokyo Bay. *U2* was located in a residential area within Tokyo. *U3* and *U4* were located in a moderately built-up area and a residential area, respectively, with both locations being away from the direct path of the target sea breeze. *R1* was southwest of *U1* and moderately urbanized, and it was located on the coastline directly along the path of the sea breeze from Sagami Bay. *R2* was also a residential area a

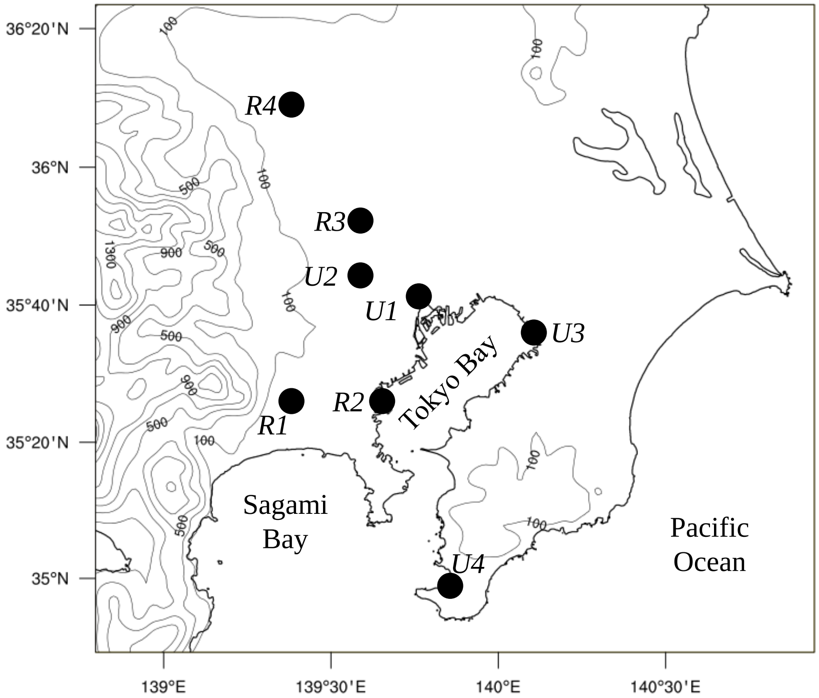

Figure 4-2 JMA observation points overlaid on model ground topography (shown in light contour lines with units = m). Topography contour starts from 100 m at 200 m intervals.

few kilometres inland from the coastline. *R3* and *R4* were both located downwind of Tokyo, and were characterized by vegetation, residential houses, and a few low-rise buildings. The relevant information is summarized in Table 4-2.

The meteorological parameters investigated were near-ground wind speed and near surface air temperature. Simulated temperatures used for comparison were the first atmospheric-level temperature (Ta) and the temperature at 2 m (T_2). The height of the first atmospheric level was around 30 m above ground level (a.g.l.). AMeDAS surface temperature observations were conducted at 1.5–2 m a.g.l., allowing direct comparison with the simulated T_2. The height of wind-speed observations differed

Table 4-2 Observation gauges information (refer to Figure 4-2 for the location)

ID	*urb_frc*	z_o	Land Use	Height
U1	0.90	7.01	URBAN	35.1
U2	0.90	1.01	URBAN	11.3
U3	0.90	1.24	URBAN	47.9
U4	0.90	0.58	URBAN	21.8
R1	0.24	0.70	CROPLAND	6.5
R2	0.73	0.66	URBAN	19.8
R3	0.22	0.58	CROPLAND	10
R4	0.55	0.58	URBAN	16.5

from the observation height for temperature and varied with location. Furthermore, the available simulated wind-speed outputs were diagnostic of the 10-m wind speed and first atmospheric wind. The first atmospheric wind was compared with a height-adjusted observation.

For consistency, a simple height adjustment for the observed wind-speed values was conducted based on the logarithmic law, except for *U1* and *U2*. Assuming H_{max} as the canopy layer height, the observation height and the first atmospheric level of *U1* and *U2* lie within the urban canopy layer. KA2013 indicated that wind speeds were homogeneous within the canopy layer, and therefore, the observed wind speed can be assumed to be the wind speed at the first atmospheric level (i.e., no height adjustment necessary) for *U1* and *U2*.

A statistical summary showing the accuracy of the cases can be seen in Table 4-3 and Table 4-4. Root mean square errors (RMSE) and biases were calculated for each selected point, comprising 705 hourly simulations and sets of observed data per station. Separate analyses were also conducted for two diurnal periods: day (D), 0500 to 1700 LST; and night (N), 1800 to 0400 LST. Observation and simulation days without precipitation were used for analysis.

4.2.1 Near-ground wind speed

As shown in Table 4-3, the over-all performance of the modified WRF case in simulating wind speed was better than that of default and vegetation cases. The lowest RMSE was observed for the NEW in most cases, mainly due to the daytime overestimation of wind speed by both the CTL and VEG (-0.91–3.17 m s^{-1} daytime and 0.15–3.80 m s^{-1} night time bias). Although slightly better performance was found for the CTL for *R1* during daytime, with all cases showing negative daytime biases, the differences in RMSE were not very significant compared with other selected points. For less urbanised grids such as *U4*, the difference in RMSE between the NEW and CTL was reduced, with both still performing better than the VEG. *U4* was the southernmost urban grid. Although most of the errors in wind speed occurred during night time due to the influence of other input conditions and model parameters not covered in this study, the NEW still produced better results for wind speed. The reason behind the improved mechanism for wind-speed simulation is discussed later.

Table 4-3 Statistical analysis of height-adjusted wind speed at selected AMeDAS stations (D = Day; N = Night)

Station ID	Case	Simulated Mean	Observed Mean	RMSE	Bias	Simulated Mean (D)	Observed Mean	RMSE (D)	Bias (D)	Simulated Mean (N)	Observed Mean	RMSE (N)	Bias (N)
U1	NEW	2.30	2.95	1.32	-0.65	2.43	3.02	1.30	-0.59	2.15	2.87	1.34	-0.72
	CNTL	4.66	2.95	2.45	1.71	4.79	3.02	2.54	1.77	4.50	2.87	2.34	1.63
	VEGE	4.22	2.95	2.21	1.27	4.42	3.02	2.39	1.40	3.97	2.87	1.98	1.10
U2	NEW	3.19	0.66	3.05	2.53	3.14	0.82	2.97	2.32	3.26	0.47	3.14	2.78
	CNTL	4.12	0.66	4.04	3.46	3.98	0.82	3.89	3.17	4.27	0.47	4.22	3.80
	VEGE	3.81	0.66	3.75	3.15	3.90	0.82	3.82	3.08	3.71	0.47	3.67	3.24
U3	NEW	3.54	3.15	1.95	0.38	3.66	3.17	1.93	0.49	3.39	3.13	1.97	0.26
	CNTL	4.40	3.15	2.47	1.24	4.40	3.17	2.40	1.23	4.40	3.13	2.54	1.27
	VEGE	4.12	3.15	2.37	0.96	4.20	3.17	2.40	1.02	4.03	3.13	2.34	0.90
U4	NEW	4.24	3.43	2.04	0.81	4.41	4.01	1.80	0.40	4.03	2.74	2.29	1.29
	CNTL	4.30	3.43	2.08	0.87	4.48	4.01	1.85	0.47	4.09	2.74	2.33	1.35
	VEGE	4.33	3.43	2.14	0.90	4.47	4.01	1.89	0.46	4.15	2.74	2.41	1.41
R1	NEW	3.93	4.93	2.41	-1.00	4.18	5.66	2.58	-1.48	3.63	4.07	2.20	-0.44
	CNTL	4.73	4.93	2.35	-0.20	4.89	5.66	2.29	-0.76	4.54	4.07	2.42	0.47
	VEGE	4.51	4.93	2.45	-0.42	4.74	5.66	2.46	-0.91	4.22	4.07	2.43	0.15
R2	NEW	4.11	3.83	1.78	0.28	4.34	3.97	1.82	0.37	3.83	3.66	1.74	0.17
	CNTL	5.02	3.83	2.32	1.19	5.09	3.97	2.28	1.13	4.93	3.66	2.35	1.26
	VEGE	4.76	3.83	2.30	0.93	4.89	3.97	2.35	0.92	4.61	3.66	2.24	0.95
R3	NEW	3.05	2.94	1.66	0.12	2.93	3.18	1.68	-0.25	3.20	2.64	1.62	0.55
	CNTL	3.80	2.94	2.09	0.86	3.55	3.18	1.91	0.37	4.09	2.64	2.30	1.45
	VEGE	3.49	2.94	1.90	0.56	3.51	3.18	1.89	0.33	3.47	2.64	1.91	0.83
R4	NEW	2.66	2.61	1.49	0.05	2.57	2.75	1.48	-0.18	2.76	2.44	1.50	0.32
	CNTL	3.14	2.61	1.72	0.53	2.92	2.75	1.55	0.17	3.39	2.44	1.91	0.95
	VEGE	3.14	2.61	1.88	0.53	3.01	2.75	1.81	0.26	3.29	2.44	1.95	0.85

4.2.2 Near-surface Temperature

Although the modified model predicts wind speed well, a difficulty remains in simulating temperature. A direct statistical comparison between the simulated T_a and the AMeDAS observed T_2 was conducted. The method was done to provide a quick-look for the simulated and observed temperatures, and to minimise the uncertainties of the diagnostically calculated T_2, explained in the succeeding statements. Direct comparison shows that the NEW performs well compared with CTL in simulating temperature. Earlier sensitivity tests indicated that an improvement in temperature was found when anthropogenic heat emission was simulated with the default WRF. When CTL is simulated without anthropogenic heating, T_a simulated from the NEW has the lowest RMSE throughout. However, when the diagnostic T_2 was used for comparison with the actual T_2 (Table 4-4), the NEW was found to perform worse than the CTL but better than VEG.

It is difficult to provide the exact reason for the NEW's T_2 mismatch with the observed T_2, but the most plausible reason lies in the differences between the measured local condition from the AMeDAS station and the assumed urban condition by the urban canopy model. The AMeDAS stations are situated in areas of green space within cities, such as the gauge for *U1* (gauge surroundings shown in Fujibe, 2011). The canopy, as defined by the new feedback parameters for urban areas, suggests limited vegetation and green space. Thus, temperature measurements within the canopy do not represent the wider area (Sugawara et al., 2004) or the WRF second-nest grid resolution and spatial variability (e.g., the urban and vegetation fraction, detailed building configuration). This results in variable heat flux, and temperature complicates the determination of a reliable measurement location. In an experiment with moving measurements conducted in one of the hottest cities in Japan (Nakayoshi et al., in preparation), it was found that the surrounding T_2 can fluctuate by approximately equal to 3°C higher than the stationary AMeDAS T_2 depending on the urban texture and morphology. Urban-wide T_2 tends to exceed gauge-observed T_2, supporting the positive bias of NEW against the negative biases observed in CTL and VEG, for both day and night. The NEW sometimes performed better during the evening (*U1*, *U3*, *R1*, and *R3*) when radiative cooling caused the NEW T_2 to fall closer to the observed values (Table 4-4).

Table 4-4 Statistical analysis of the 2-m temperature at selected AMeDAS stations (D = Day; N = Night)

Station ID	**Case**	**Simulated Mean**	**Observed Mean**	**RMSE**	**Bias**	**Simulated Mean (D)**	**Observed Mean**	**RMSE (D)**	**Bias (D)**	**Simulated Mean (N)**	**Observed Mean**	**RMSE (N)**	**Bias (N)**
U1	NEW	27.21	26.77	1.55	0.44	28.18	27.43	1.73	0.75	26.06	26.00	1.30	0.06
	CNTL	27.02	26.77	1.50	0.24	28.05	27.43	1.64	0.62	25.80	26.00	1.33	-0.20
	VEGE	25.18	26.77	2.24	-1.59	26.46	27.43	1.87	-0.97	23.68	26.00	2.61	-2.32
U2	NEW	27.14	26.72	1.78	0.42	28.49	27.81	1.88	0.67	25.54	25.43	1.66	0.11
	CNTL	26.73	26.72	1.55	0.01	27.89	27.81	1.59	0.08	25.35	25.43	1.50	-0.07
	VEGE	24.73	26.72	2.62	-1.99	26.26	27.81	2.31	-1.55	22.91	25.43	2.94	-2.51
U3	NEW	26.60	26.35	1.86	0.26	27.86	27.23	1.95	0.63	25.11	25.30	1.75	-0.19
	CNTL	25.82	26.35	1.74	-0.53	26.89	27.23	1.71	-0.34	24.55	25.30	1.78	-0.75
	VEGE	24.63	26.35	2.45	-1.72	25.99	27.23	2.10	-1.25	23.02	25.30	2.81	-2.28
U4	NEW	26.15	25.45	1.79	0.70	27.50	26.83	1.67	0.67	24.56	23.82	1.92	0.74
	CNTL	25.28	25.45	1.55	-0.17	26.36	26.83	1.48	-0.46	24.00	23.82	1.64	0.19
	VEGE	24.62	25.45	1.75	-0.83	25.78	26.83	1.83	-1.05	23.24	23.82	1.66	-0.58
R1	NEW	26.03	25.65	1.73	0.38	27.45	26.98	1.75	0.47	24.34	24.07	1.71	0.27
	CNTL	25.58	25.65	1.74	-0.07	26.90	26.98	1.76	-0.09	24.03	24.07	1.72	-0.04
	VEGE	24.72	25.65	1.95	-0.92	26.06	26.98	1.98	-0.93	23.15	24.07	1.91	-0.92
R2	NEW	26.98	26.36	1.71	0.63	28.19	27.32	1.84	0.87	25.55	25.22	1.55	0.33
	CNTL	26.48	26.36	1.43	0.12	27.40	27.32	1.48	0.08	25.39	25.22	1.36	0.17
	VEGE	25.07	26.36	1.95	-1.29	26.14	27.32	1.97	-1.18	23.80	25.22	1.94	-1.42
R3	NEW	26.51	26.17	1.82	0.34	28.10	27.36	1.94	0.74	24.62	24.76	1.65	-0.14
	CNTL	25.94	26.17	1.67	-0.23	27.43	27.36	1.64	0.07	24.17	24.76	1.70	-0.59
	VEGE	24.95	26.17	2.10	-1.22	26.48	27.36	1.94	-0.88	23.14	24.76	2.29	-1.61
R4	NEW	26.51	26.31	1.89	0.20	28.28	27.63	1.87	0.65	24.42	24.75	1.92	-0.33
	CNTL	26.22	26.31	1.72	-0.09	27.54	27.63	1.69	-0.10	24.66	24.75	1.75	-0.09
	VEGE	24.70	26.31	2.47	-1.61	26.34	27.63	2.25	-1.29	22.76	24.75	2.71	-1.99

Previous studies have also mentioned spatial variability in temperature. Similar difficulties in assigning representative temperature values for urban grids were also found in a study of an urban heat island in Seoul, South Korea (Kim et al., 2005). In that study, appreciable temperature variations within Seoul were found, and the gauge with the warmest temperature was selected because its location matched typical urban characteristics. In a 1740 x 750-m area in Singapore, temperature was found to vary spatially by 37–41°C (Tso, 1996). Williams et al. (2000) also noted differences between measurement points and suggested that 1° × 1° areal averaged measurements can be partly ascribed to the difference between point measurements and spatially integrated values. Thus, the representativeness of point measurements remains a challenge, especially for urban climate studies.

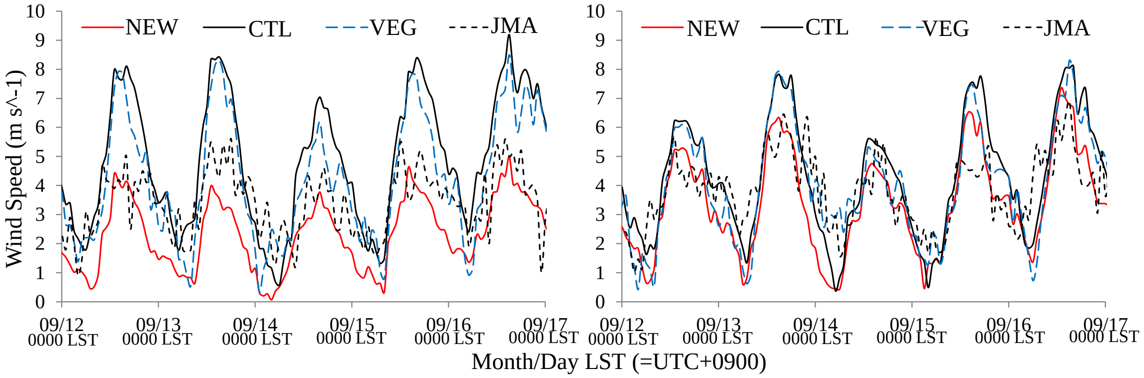

Figure 4-3 Five-day trend of hourly height-adjusted wind speed at U1 (left) and R2 (right)

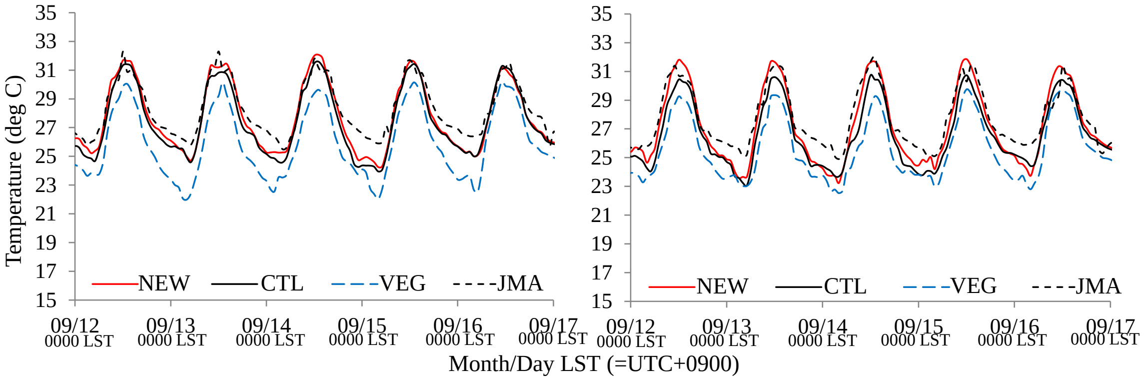

Figure 4-4 Five-day trend of hourly 2-m temperature at U1 (left) and R2 (right)

The succeeding section focuses on the sea breeze event that occurred on September 14, 2011. Figure 4-3 and Figure 4-4 show the trend of wind speed and T_2 during September 12–17, 2011, from the two-month simulation. The synoptic condition during the dates selected reveals a prevailing high pressure system very close to the eastern side of Japan. A stationary front exists at the northernmost part of Japan. These period marks the beginning of transition from summer to autumn. During this period, NEW was found to perform well when simulating higher wind speed and temperatures than the other cases. Wind speed was largely overestimated by both CTL and VEGE with a slight underestimation from the NEW. During night time, all cases underestimate the temperature in spite generally no little bias was found during night-time from the statistics shown in Table 4-4. The intensity and commonality of the large underestimations during night-time were probably brought about by other factors aside from the roughness parameters. In spite this, NEW simulated temperature approaches the observed temperature at night.

4.3 Results and Discussion

4.3.1 Sea Breeze Analysis from Clouds

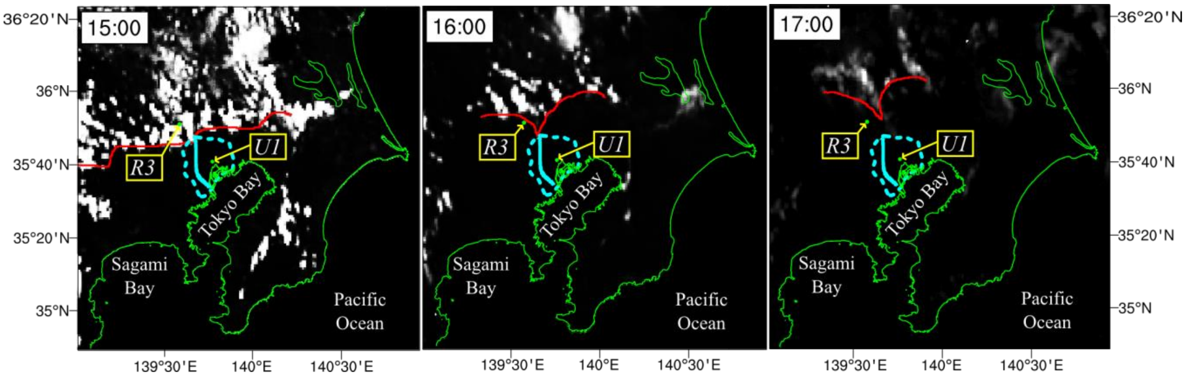

Figure 4-5 September 14, 2011, 1600 LST (UTC = LST – 9 hours) Rapidscan geostationary satellite image. White patches correspond to clouds. Sea-breeze fronts are shown with red lines. Dashed blue green lines indicate densely built-up regions with *d* > 10 m. Solid blue green line indicates location of a common cloud street.

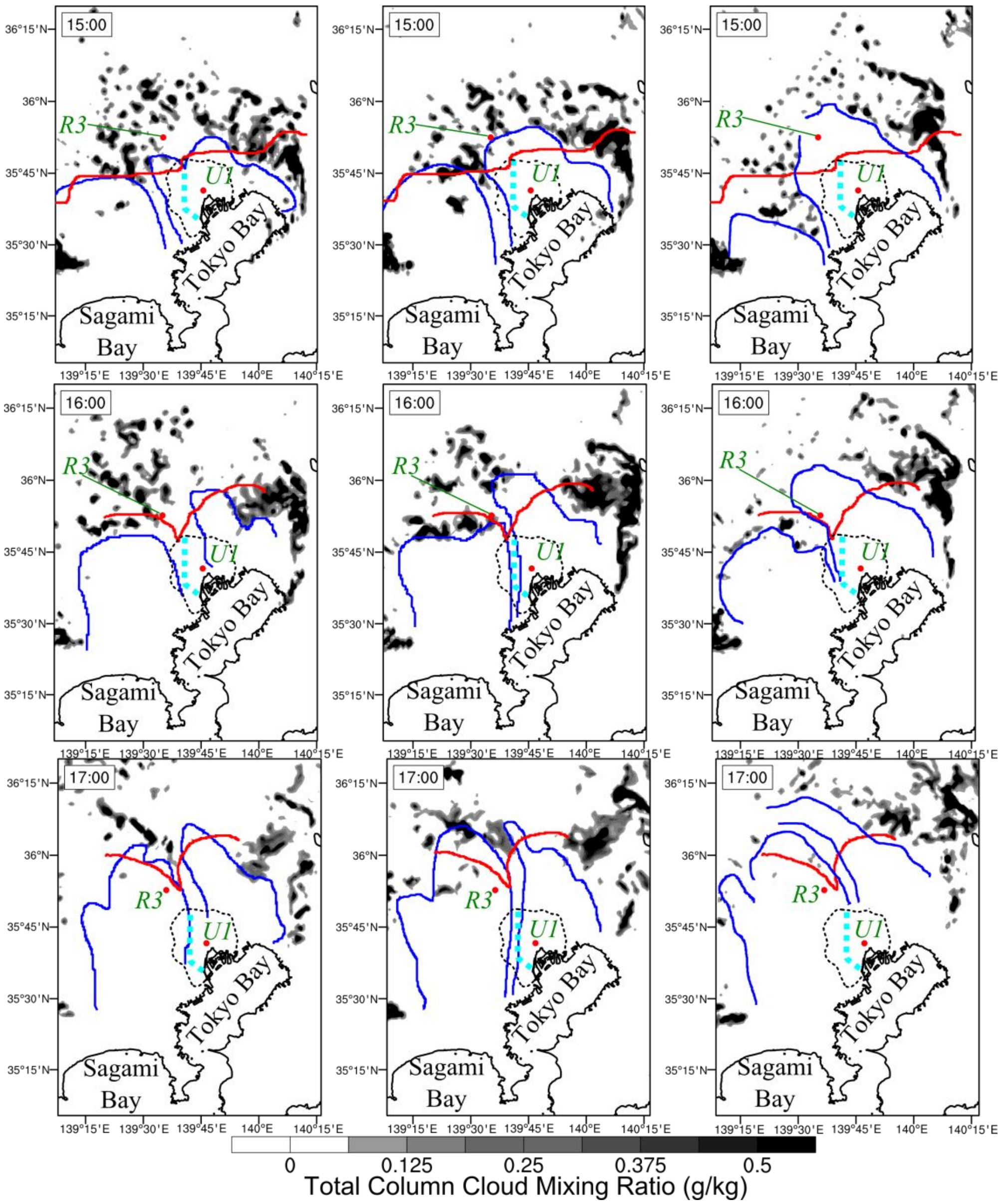

Figure 4-6 September 14, 2011, total column cloud mixing ratio from NEW (left), CTL (centre), VEG (right). Red lines represent Rapidscan geostationary satellite cloud outlines drawn from Figure 4-5. Blue lines represent the sea breeze front from the first atmospheric-level convergence. Dashed black lines indicate regions with *d* > 10 m. Red dots mark the location of *U1* and *R3* (labelled in green). Dashed light blue lines indicate the location of a common cloud street.

An approaching sea breeze can sometimes be seen from the motion of clouds during clear sunny days (Damato et al., 2003; Corpetti and Planchon, 2011; Inoue and Kimura, 2004; Kanda et al., 2001). Viewed from a high-resolution geostationary satellite (Rapidscan), the sea breeze front can be depicted as a boundary between cloudy and clear regions, such as that shown in Figure 4-5. At 1100 LST on September 14, 2011, clouds start progressing from the coastline in the direction inland, labelled *R3*. The wedge-shaped cloud line suggests two sea breeze sources, Tokyo Bay and Sagami Bay. Locally known as Kanpachi clouds (Kanda et al., 2001), a distinct cloud street occasionally forms and elongates at a distance from *U1* to *R3*. The cloud street which was not generated on the date of this simulation is commonly generated by the convergence of two sea breezes, shown in blue lines in Figure 4-6. Later in the afternoon, clouds converged above the region surrounding *R3* and dissipated before sunset. For convenience, the boundaries representing the fronts were carefully hand-drawn in red for comparison with the WRF.

Clouds were resolved well in WRF when the JMA Nonhydrostatic Mesoscale Model (MSM) was used to determine the boundary (Figure 4-6), especially in the region surrounding *U1, U2, R3* and *R4*. When the spatial distribution of the total column cloud-mixing ratios was compared with Rapidscan images, the observed clouds, which were mostly concentrated at 2 km above mean sea level (AMSL), matched the simulation well, with slight differences depending on each case. Based on the overlain snapshots of the convergence in the first atmospheric level, it can be deduced that the cloud distribution was substantially influenced by the inflow of sea breeze. Of the three cases, the VEG simulated the least cloud and predicted that the clouds would move faster than was observed.

Considering only the cloud motion and dissipation, the sea breeze front appeared earliest in the VEG case. The NEW was similar to the CTL with regards to improving cloud formation. However, in the CTL, there was an earlier advancement by a few km along the path of the sea breeze coming from Tokyo Bay and an earlier dissipation on 1600 LST. On 1500 LST, cloud formations at the south of *R3* deviate a bit farther north of the red line for the CTL. Further, clouds along the sea breeze of Sagami Bay are also slightly delayed and formed a bit south of the red line. Meanwhile on 1600 LST, the NEW also shows slightly better representation of clouds west of R3 with a shorter gap existing between the clouds north of *R3*. The improved roughness representation in Tokyo has the most dominant effect in delaying cloud advection by sea breezes. The current findings suggest that urban forcing and parameterisation in mesoscale models are quite significant for determining the accuracy of cloud distribution.

4.3.2 Near-ground Winds

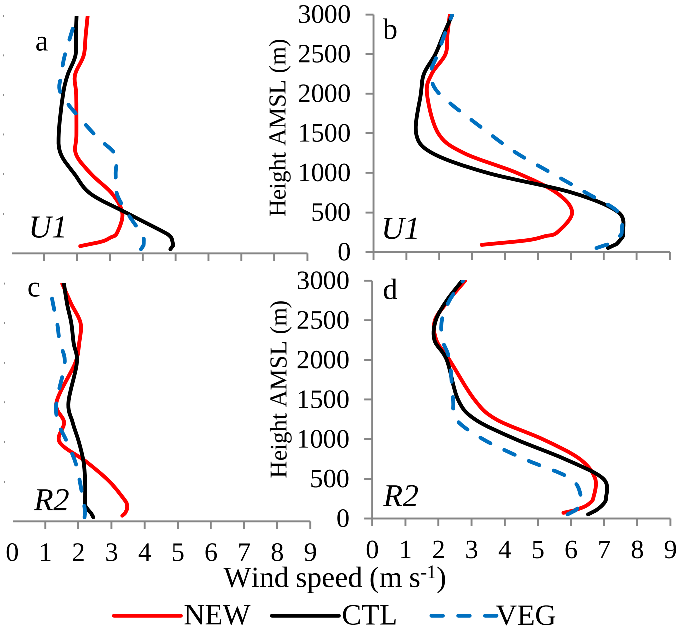

Figure 4-7 September 14, 2011, WRF hourly-averaged horizontal wind-speed vertical profiles above U1 on 1200 LST (a) and 1500 LST (b); and above R1 on 1200 LST (c) and 1500 LST (d)

The new aerodynamic parameters dramatically reduced the simulated wind speed, especially in highly urbanised areas. Around noontime, urban heat island increased the thermal low throughout Central Japan. Thus, faster wind speeds for the CTL can be seen in Figure 4-7 for both *U1* and *R1* in Figure 4-8. However, the significant roughness in *U1* reduces winds at heights of up to 500 m. Despite the faster trailing winds behind the front, surface wind speed was slowest in the NEW at 1500 LST. At *R1*, with a lower *d* and z_o compared with *U1*, the consideration of the urban fraction at predominantly non-urban grids caused the NEW to simulate faster near-surface wind speeds around noontime. At 1500 LST, the drag effect was apparent, as the CTL exceeded the wind speed in the NEW.

Wind speed differences which can also be seen at upper levels are caused not only due to the aerodynamic effect of the roughness parameters but also possibly due to the differences in the heat being released into the atmosphere by each case and to large scale effects (e.g. two-way nesting). Even if only the surface roughness is varied between NEW and CTL, to achieve an equivalent wind speed simulation at the upper levels is impossible because real WRF simulations involves various 3-dimensional processes and is non-linear.

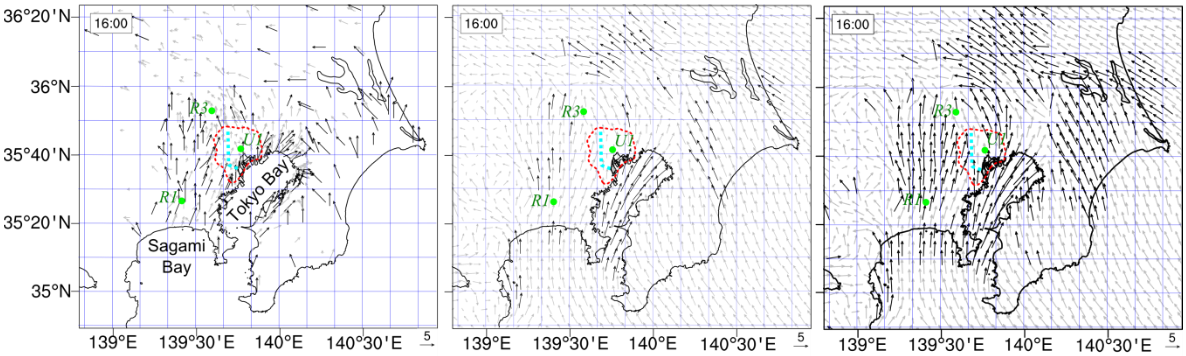

Figure 4-8 September 14, 2011, wind observed at 25 m (left), NEW 10-m wind (centre), NEW first atmospheric-level wind (right). Darker wind vectors have wind speed >= 5 m/s. Dashed red lines indicate regions with *d* > 10 m. Green dots represent AMeDAS stations. Dashed light blue lines indicate the location of a common cloud street.

Surface drag in urban areas was also captured by the Atmospheric Environmental Regional Observation System (AEROS) of the National Institute for Environmental Studies, Japan (NIES), as shown in the 1600 LST snapshot shown in Figure 4-8. The threshold of wind vector visibility was set based on the most convenient plot to analyse the sea breeze front and differentiate the cases. The drag depicted in NEW matched the observations, despite the height differences.

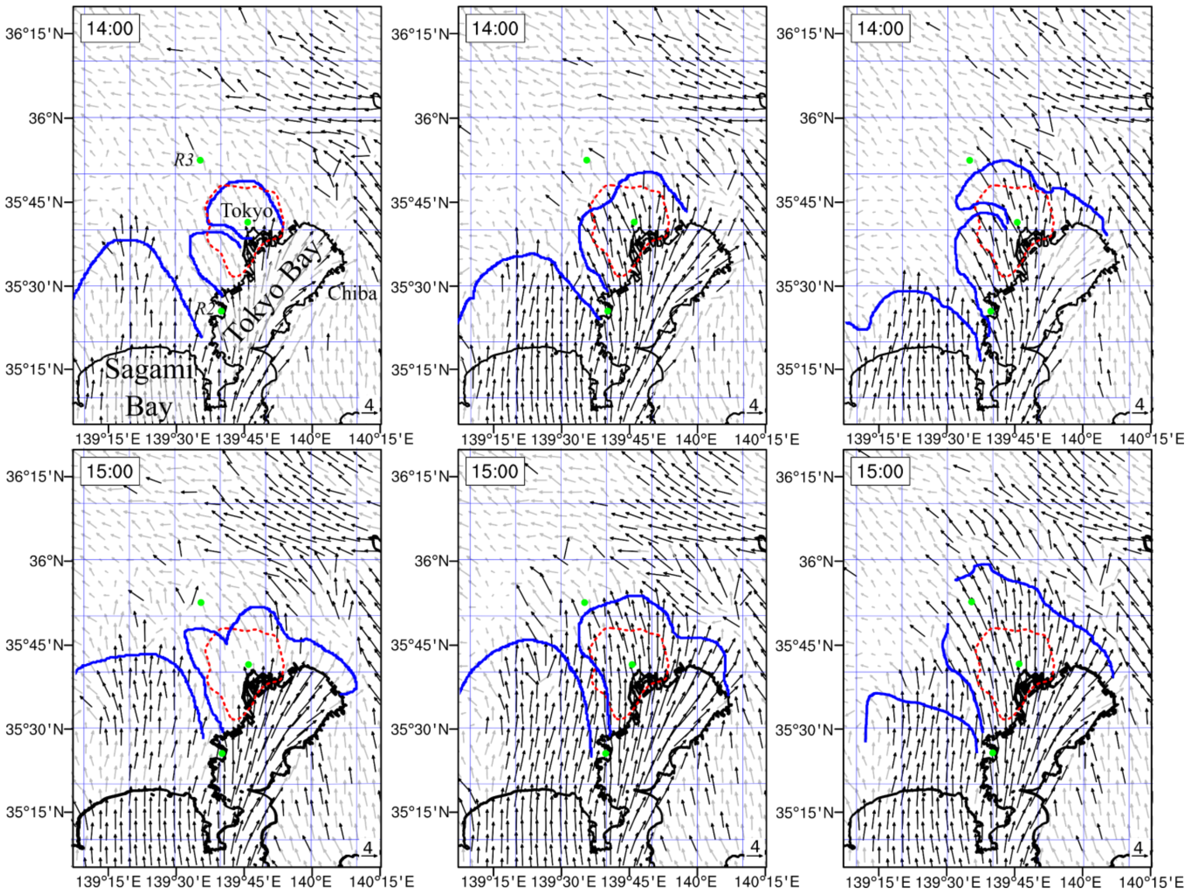

Figure 4-9 September 14, 2011, wind simulated by WRF at 10-m height (darker wind vectors >= 4 m/s) and first atmospheric-level convergence (blue lines) for NEW (left), CTL (centre), and VEG (right). Dashed red lines indicate regions with d > 10 m. Green dots represent AMeDAS stations.

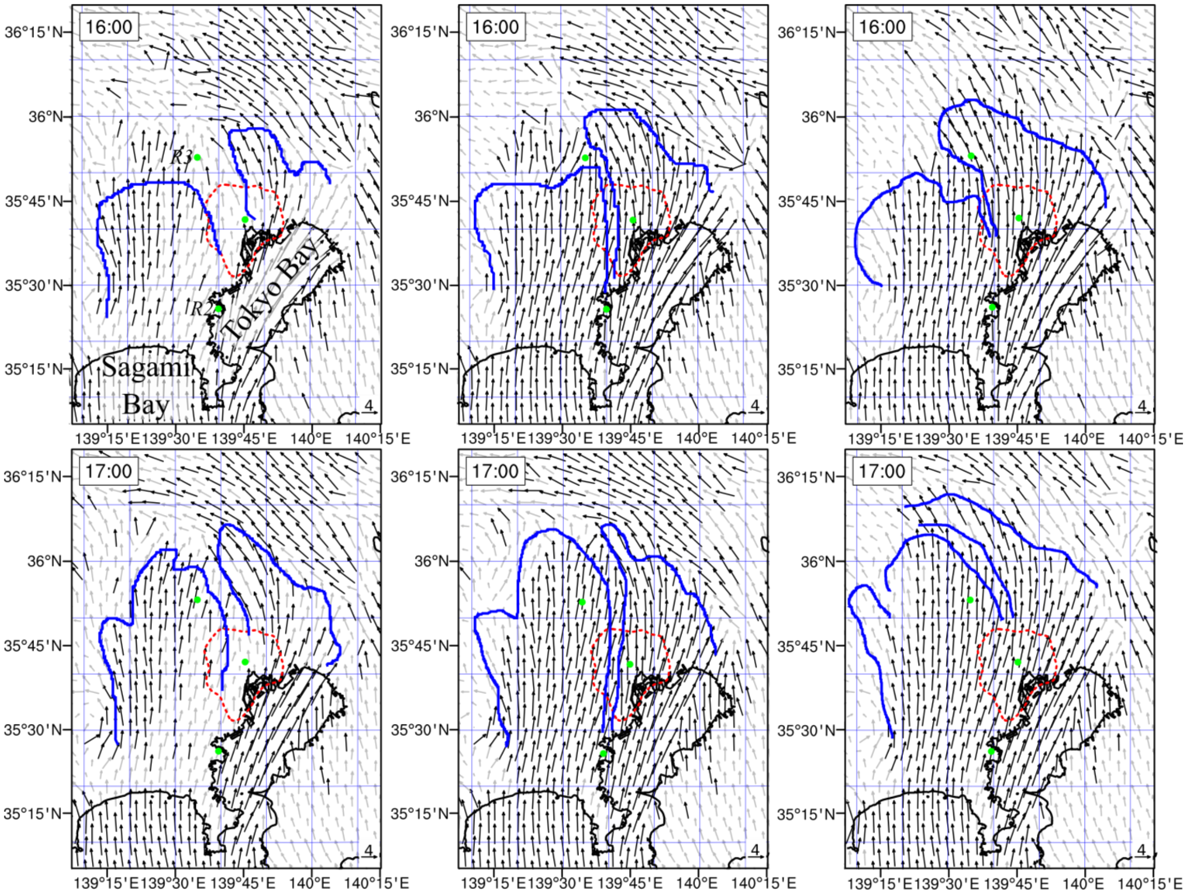

Figure 4-10 Continuation of Figure 4-9

The time-varying wind-speed distribution in Figure 4-9 and Figure 4-10 shows the delineated convergence lines denoting two sea breeze flows passing above the region surrounding *R1* and *R2* and the region surrounding *U1*. One flow arrived from Sagami Bay, and the other was from Tokyo Bay. Near the surface, the front from Sagami Bay advanced faster and was stronger than the front coming from the Tokyo Bay. The buildings of Tokyo and Yokohama, close to *R2*, obstructed the flow of the sea breeze from Tokyo Bay, making it less visible from the wind-speed distribution map (NEW). Using default roughness parameters, wind speeds were simulated to be faster, but noticeable drag was observed when no urban areas were assumed. At 1400 LST, the sea breeze front from Sagami Bay advanced earlier for the NEW, followed by the CTL and VEG, due to the higher land–sea pressure gradient. The Sagami Bay sea breeze appeared to weaken near the coastline in the NEW due to the combined effect of the roughness at the coastline facing Sagami Bay and the western slope. The sea breeze from Tokyo Bay easily penetrated inland at 1400 LST in the VEG, showing the potential of the sea breeze when no urban obstructions were considered. After 1 hour, the wind speeds passing above Tokyo remained to be weak in the NEW. With the passage of the front above the urban canopy layer at 1500 LST, faster trailing winds could be seen at the CTL that were not observed in the NEW. By 1600 LST, the winds had increased in intensity in between *To1* and *C1*. The urban heat island circulation in Tokyo, explained further in the next section, contributed to the horizontal wind reduction in the Tokyo Bay's sea breeze's wake (1600 LST for the NEW). When the easterly sea breeze from the Pacific Ocean assisted the convergence later in the afternoon, surface winds remained weak in areas with large roughness parameters and at the convergence line of the two sea breezes.

4.3.3 Sea Breeze Convergence Inland of Tokyo

Three distinct convergence/divergence regions were found to exist in the late afternoon of September 14, 2011, as shown in Figure 4-11: Region 1 – a convergence/divergence region above the inland of Tokyo; Region 2 – an eastward moving convergence line above Tokyo generated by sea breeze flows coming from Tokyo Bay and Sagami Bay; and Region 3 – an elongated convergence region east of Tokyo. Regions 1 and 2 (bounded by dashed boxes) were substantially influenced by the sea breeze and the urban parameters.

Region 3 was generated by the convergence of sea breeze from Tokyo Bay and the easterly sea breeze. Only the mechanism of regions 1 and 2 are discussed here due to their direct interaction with the urban areas.

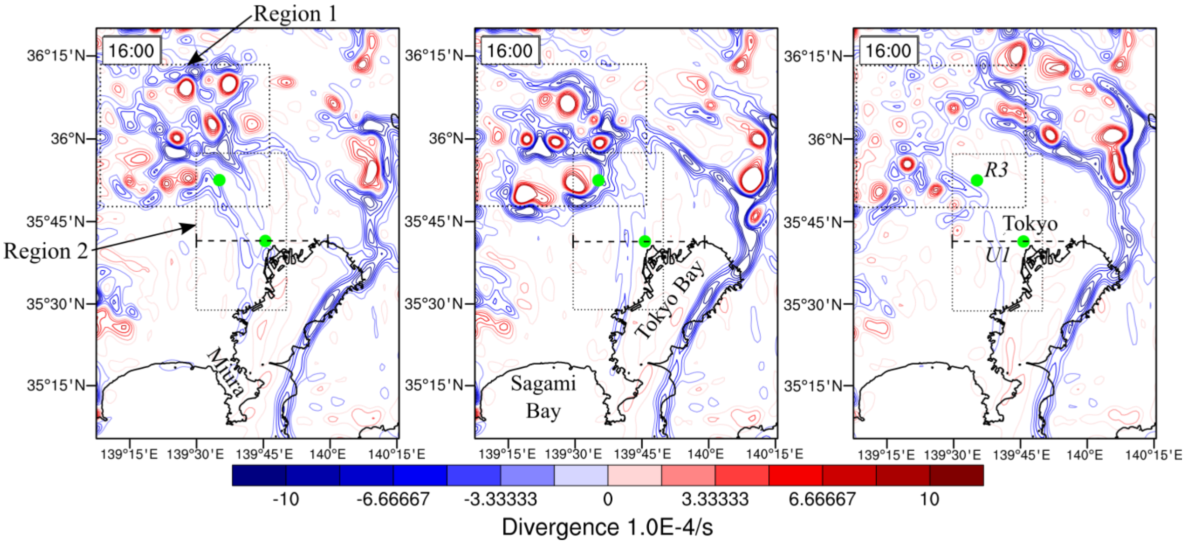

Figure 4-11 September 14, 2011, 1600 LST divergence of first atmospheric winds for NEW (left), CTL (centre), and VEG (right) at 1600 LST. Regions bounded by dashed lines represent the analysed convergence zones. The dashed line represents the location of the vertical slice used in Figure 4-12

The strong convergent/divergent region occurring inland of Tokyo later in the afternoon was caused by the incoming sea breezes from Tokyo Bay and Sagami Bay, and the easterly sea breeze (Region 1 in Figure 4-11). The convergence branches were brought about by the combination of in-land penetration of sea breeze and turbulent mixing. Ahead of the fronts (NEW and CTL), the horizontal winds were weaker and slightly more dispersed (divergent cells). Inland of Tokyo is also a region where advected heat is deposited, especially during summer, when sea breezes could not extend farther inland due to the surface frictional stress (Sato et al., 2008). The slight differences in CTL and VEG to the convergence inland can maybe affect the understanding of common extreme events in that region (e.g. heat stroke and localized heavy rainfall). When new aerodynamic roughness parameters were introduced, differences in the surrounding convergence could be seen due to the intensity of the approaching sea breeze front. The CTL had the strongest first-level convergence at the front (notice the darker blue contours compared to other cases), with wider divergent cells leeward. NEW simulated leeward divergent cells with a smaller diameter and slightly weaker convergence. In a test run, during which distributed anthropogenic heat emission was removed in the CTL, the region of convergence receded westward; thus, urban heating contributed to the delay of sea breeze penetration to the inland.

Divergent cells may be generated possibly by two mechanisms. First, weak wind regions that are also influenced by the heat island circulation and ambient winds may form ahead of the front due to the balance of vertical mixing and the horizontal pressure gradient (from idealised test simulations of Ohashi et al., 2002). On September 14, 2011, the ambient wind condition in the late afternoon is a prevailing south-easterly wind at the rate of approximately 2 m/s. The heat island circulation is described here as the strong vertical motion found at the centre of the study domain due to strong surface heating similar to Yoshikado et al. (1989) findings. The weak wind together with the displacement of air parcels above may cause subsidence and downward adiabatic transport enhancing divergence near the surface. However, results show that surface temperatures were slightly reduced close to the surface suggesting a different mechanism that idealised simulations failed to uncover. The better and second mechanism is due to the clouds generated by the front (refer to 1600 LST in Figure 4-6 for the cloud image corresponding to that of Figure

4-11). At the front, strong updrafts lift moist air upward, continually generating clouds above the boundary layer. These clouds are advected ahead of the front and above the weak-wind region due to the faster ambient wind speed above the boundary layer. As a result, shortwave radiation levels fall, blowing surface winds apart. Divergence underneath clouds was also simulated in the study by Salamanca et al. (2011). The presence of cloud contributed significantly to the simulated divergent patches found above the inland of Tokyo during this period.

4.3.4 Atmospheric Boundary Layer Structure Above Convergence Region 2

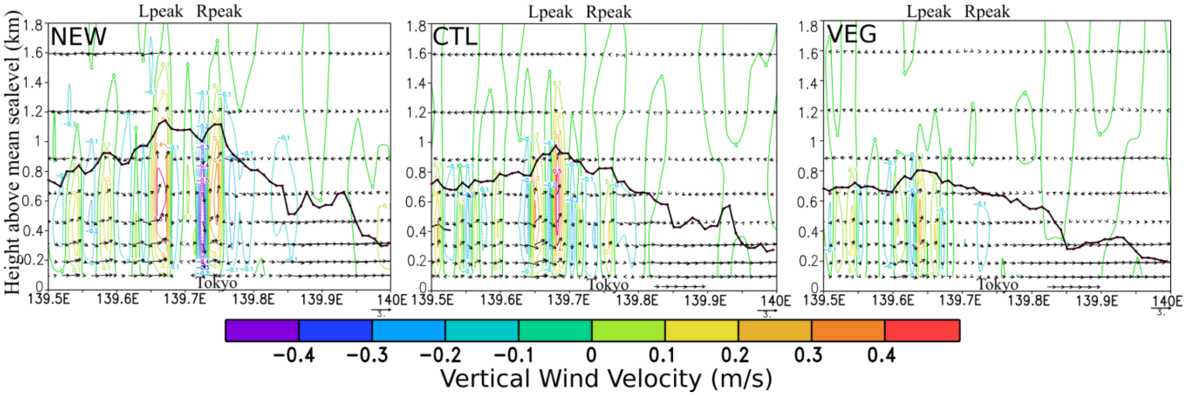

Figure 4-12 Vertical cross-section for September 14, 2011, 1600 LST (slice location shown in Figure 4-11) vertical wind (contour), wind velocity (vectors) calculated from west-to-east wind component and vertical wind component (enhanced by 2.5), and planetary boundary-layer height (solid lines)

A convergence region was found (Region 2 in Figure 4-11) extending from the convergence region 1. Although it was considerably weaker in intensity than inland of Tokyo, this region earlier extended all the way to the Miura Peninsula (see location on the left-most image of Figure 4-11) and then later receded slowly in the direction of Tokyo. Bounded by the smaller dashed box in the divergence snapshot in Figure 4-11, two distinct blue elongated cells stretching from Tokyo to the inland represent the convergence line. Above this region of convergence, the top of the boundary layer peaked (cross sections in Figure 4-12), with strong updrafts underneath. The mechanism of the elongated convergence region and its features varied for each case.

The NEW had the highest simulated planetary boundary-layer height (PBLH), followed by the CTL and VEG. The maximum PBLH simulated by NEW and CTL (> 1 km) are typical during hot days with sea breeze (Yoshikado et al., 1989). The locations with obvious PBLH peaks were situated close to each other; the leftmost (higher) moving eastward (hereinafter called Lpeak) and to the right (lower) remaining directly above Tokyo (hereinafter called Rpeak). Westward of the selected cross-section is characterised by less urbanisation. While easternmost is located near the coastline explaining the low PBLH. Within the two peaks, high vertical wind speeds (approximately equal to 0.2-0.5 m s^{-1}) were visible. The peaks varied depending on the urban parameters included. The VEG case simulated only the Lpeak. This could mean that the Rpeak only represents the urban heat island circulation, mentioned in p. 55, while the Lpeak represents the area where sea breezes coming from Tokyo Bay and Sagami Bay converged. Roughness parameters play an important role in intensifying turbulent mixing as manifested by the difference in peak height and wind-speed intensities between the NEW and CTL. With the increasing d and z_o from the southwest region to Tokyo, a transition from rough to rougher surfaces occurred. This strengthened horizontal convergence and upward motion. The Lpeak increased by approximately equal to 100 m and the Rpeak increased by approximately equal to 200 m.

This is the reason why the convergence line appears to be wider in the NEW than in the CTL.

The investigation of horizontal and vertical winds, along with their convergence, provides a clearer picture of how a sea breeze interacts with the highly urbanised area of Tokyo. The earlier development of the land-sea pressure gradient in the NEW, due to additional heating near the surface, caused the sea breeze front to pass the Tokyo Bay shoreline earlier. The densely built-up, very rough, buildings of Tokyo then tended to shift the sea breeze wind upwards, increasing the boundary-layer height. Alongside this, the Tokyo Bay's sea breeze also appeared to move around the area with the aid of the Sagami Bay's sea breeze and the easterly sea breeze, which caused the extended convergence region leeward of Tokyo. With relatively rougher areas concentrated near the coastline, the sea breeze lost its momentum due to friction, resulting in the stagnation of a weakened sea breeze inland of Tokyo.

4.4 Chapter Summary

In this chapter, the updated WRF model, introduced in chapter 3, are now evaluated and applied. A comparison between the modified model and its default version, which uses uniform roughness parameters within a conventional method, was conducted for a 2-month simulation during summer. Results showed a significant improvement in the simulation of surface wind speeds but more improvements were still necessary for temperature accuracy. A sea-breeze event was then selected from the 2-month simulation. A separate simulation was conducted for the selected event to understand the atmospheric effects of actual building roughness of Tokyo. Sea-breeze penetration weakened and was more delayed at urbanised areas in the updated model but not in the default model. Furthermore, the slow sea-breeze penetration also lessened heat advection downwind allowing stronger turbulent mixing and deeper boundary layer above urban areas. Horizontal wind speed reduction, due to the increased urban surface drag, reached several hundreds of metres above through the strong convection.

5 Improved WRF Model Application at Major Cities in Japan

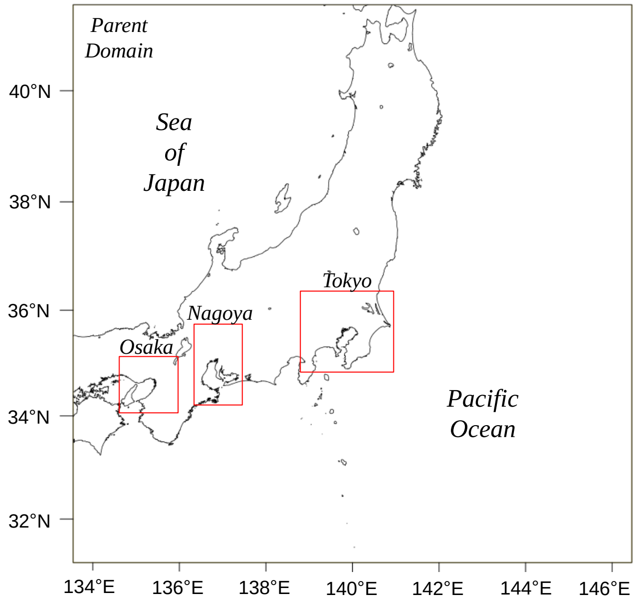

Figure 5-1 Domain coverage of WRF simulation over major cities in Honshu, Japan. Red boxes cover child domains.

After testing the model in Kanto for the summer of 2011 in the previous chapter, the applicability of the updated model at other cities and different study period are addressed. The impact of a nation-wide surface boundary distributed input prepared by Makabe et al. (2014) was initially investigated. From the ESRI Japan's 2012 detailed GIS, 1 km datasets and Cad Center of H_{ave}, H_{max}, σ_H, λ_p and λ_f were prepared for the whole Japan5). The geometric parameters were then used to estimate a nationwide d and z_o distribution. Monthly diurnal 22.5 s x 15 s. AH datasets for the whole Japan were provided by the National Institute of Advanced Industrial Science and Technology (AIST).

The target cities are Osaka, Nagoya, and Tokyo. The simulation results were compared with observation gauges. The findings focused mainly on the wind field and temperature, in general, as affected by both roughness and anthropogenic heating from the surface.

5.1 Numerical Settings

Four domains were selected with the final domains (1.2x1.2 km grid spacing) covering major cities such as Tokyo, Osaka, and Nagoya as shown in Figure 5-1. The distribution of d, z_o, and AH is shown in Figure 5-2. Japan Meteorological Agency's 3-hr. Nonhydrostatic Mesoscale Model (MSM) with 0.1x0.125 degrees spatial resolution for the atmospheric level and 0.05x0.625 degrees resolution for the surface level were used. Lacking skin temperature, soil temperature and moisture in the MSM were compensated with 6-hr. NCEP FNL Operational Model Global Tropospheric Analyses. The size and resolution of the domains used are shown in Table 5-1. Two-way nesting was used.

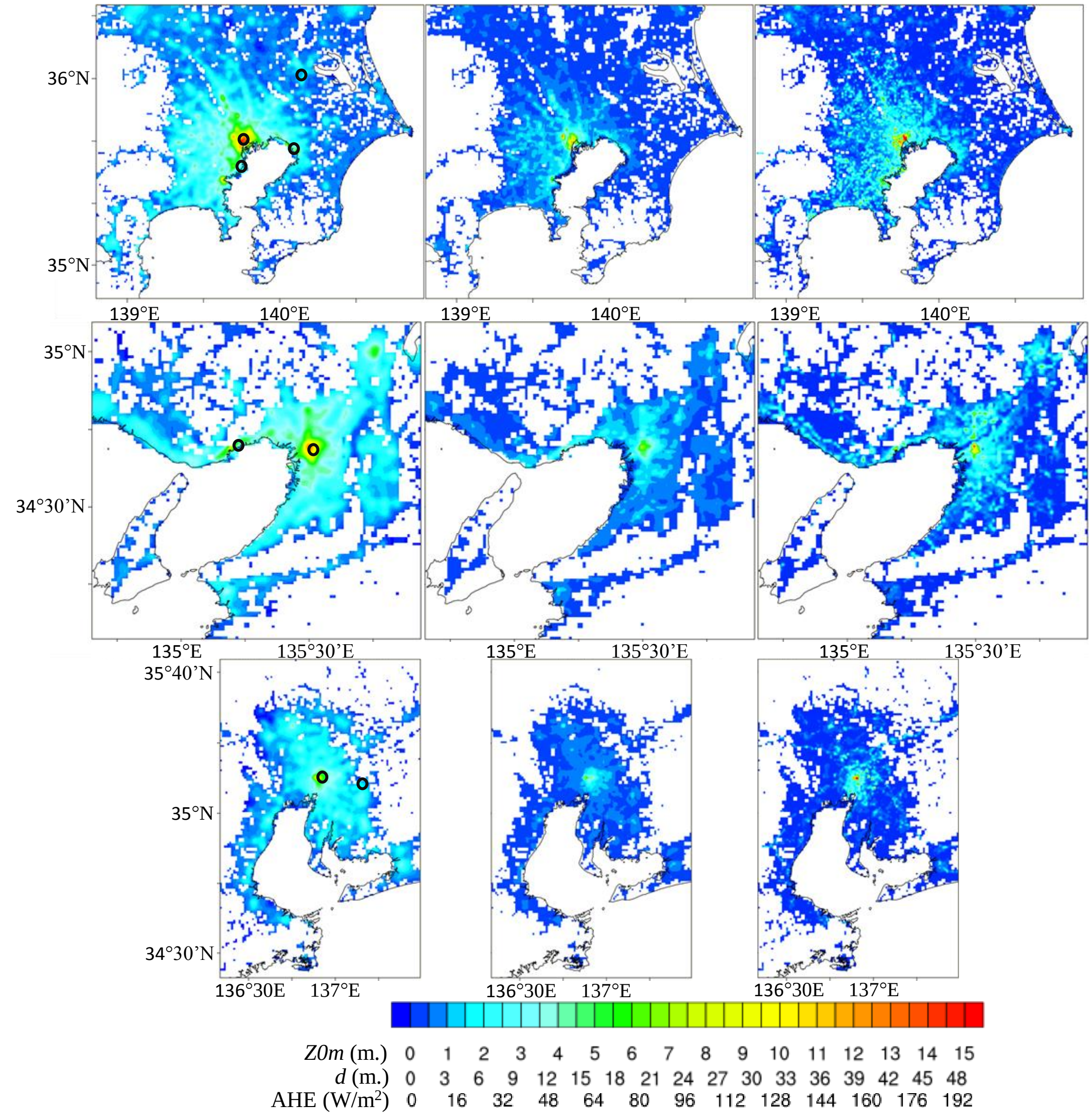

Figure 5-2 Distribution of *d*, z_o, and 1200 LST AHE for Tokyo domain (Top), Osaka domain (Middle), and Nagoya domain (Bottom) domains. The selected AMeDAS stations for comparison are encircled in the *d* distribution.

Table 5-1 Domain Settings

Domain	Tokyo	Osaka	Nagoya
Resolution	1.2 km	1.2 km	1.2 km
E-W grid size	201	121	109
S-N grids size	181	117	173
Vert levels	28	28	28
Time step	2.143 s	2.143 s	2.143 s
% Urban	50.19 %	50.32 %	44.89 %

Table 5-2 Simulation Cases

Cases	*d* and *z0m*	*AH*
NEW	GRIDDED	GRIDDED
CTL	FIXED (5.71,0.33)	None
NEWnAH	GRIDDED	None

The total simulation dates were from August 11 – 13, 2013 with a one day spin-up period using the WRFv3.3.1. These days were selected due to its country-wide high pressure condition. A localized heavy rainfall incident was recorded on August 12 in Tokyo but neglected in this study. Table 5-2 summarizes the cases. To emphasize the effect of urban areas using the gridded surface parameters, a NEW case was simulated in comparison to the CTL. NEW is the updated WRF version considering all the improvements. CTL is the default WRF version without AH. An additional NEWnAH run was conducted to clarify the effect of AH relative to the roughness parameters.

5.2 Model Validation

The simulation results were compared with the JMA Automated Meteorology Data Acquisition System (AMeDAS) stations from August 10 – 13, 2013. The selected stations are highlighted in Figure 5-2.

5.2.1 Near-ground Wind Speed

The WRF simulation outputs the wind speed at 10 m diagnostically and at the first vertical grid level, with heights approximately at 30 m. The values for comparison depend on whichever is closer to the AMeDAS observation level. Root Mean Square Error (RMSE) was calculated using 58 hourly data for each station (Figure 5-3).

RMSE is least for the NEW and NEWnAH. The little difference of accuracy between them suggests that AH has little influence in the wind speed. The large difference in RMSE values between NEW and CTL means urban roughness has a larger influence in the wind speed accuracy. Moreover, stations with *d* greater than 10 m have large RMSE differences. The top 3 locations with the largest CTL and NEW RMSE differences are Tokyo, Osaka, and Chiba. Least improvements were seen at the selected points of Nagoya domain where roughness parameters were found lower compared to other locations. Although the station at Yokohama, Kanagawa shows low roughness parameters, the 2-dimensional effect from its surroundings (e.g. Tokyo and its surroundings with significant roughness values) affect the accuracy.

The main reason behind the larger RMSE values for CTL is that it overestimates the surface wind speeds (Figure 5-4) at rough areas. NEW performs well in matching with the observed wind speeds for both Osaka and Tokyo. Both NEW and CTL remain to overestimate the winds at Nagoya. In spite this, NEW approach closer to Nagoya station's observation. Nagoya domain, with lesser roughness parameters than Tokyo and Osaka, simulated a more complicated wind circulation with winds alternating between the sea and the surrounding mountains. This suggests the possibility that the selection of domain size, target dates, and boundary conditions highly influenced the accuracy for these dates.

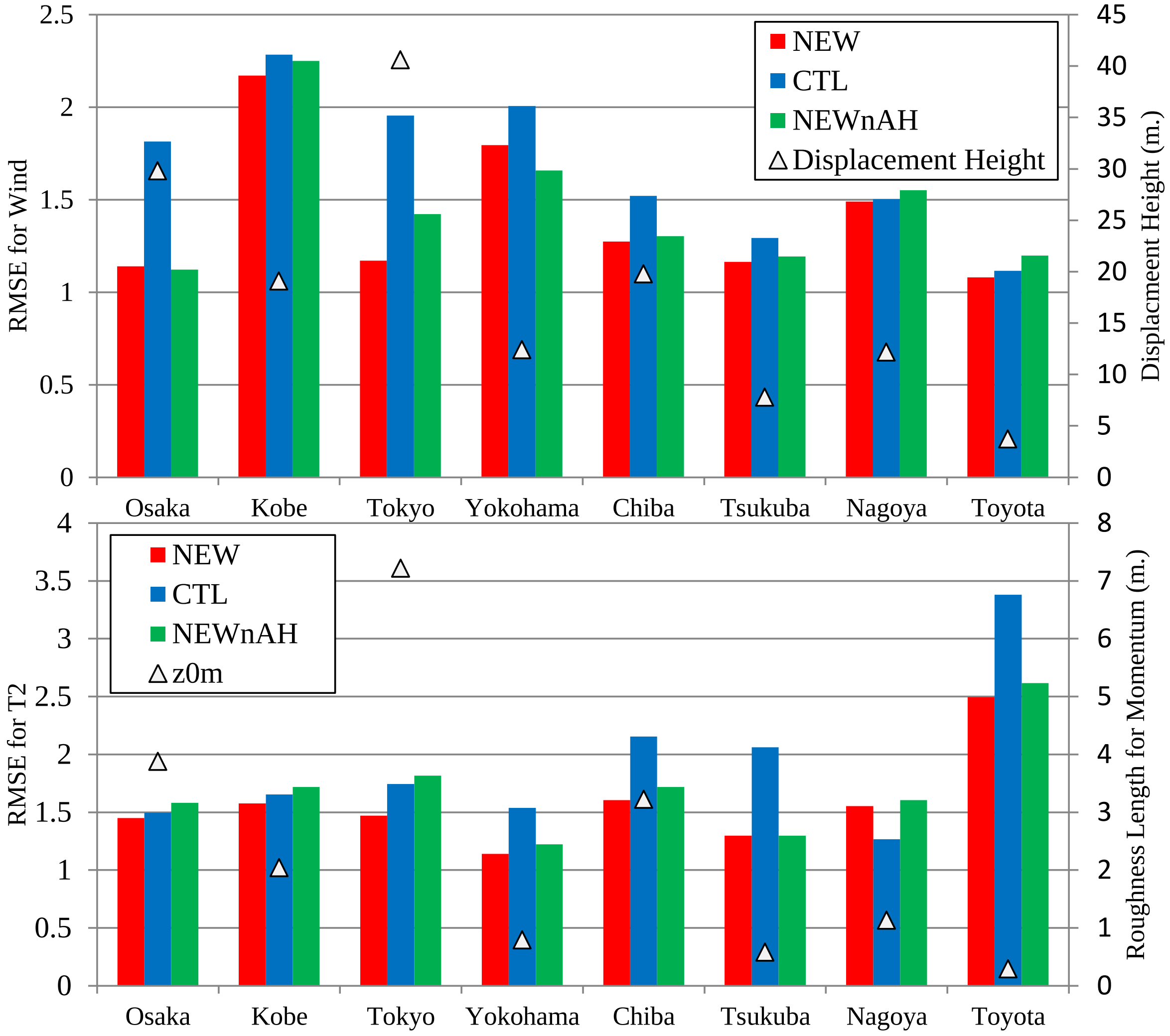

Figure 5-3 RMSE values for wind speed (Above) and 2 m temperature (Below) for each case and AMeDAS station. Corresponding d and z0m plotted in filled triangles.

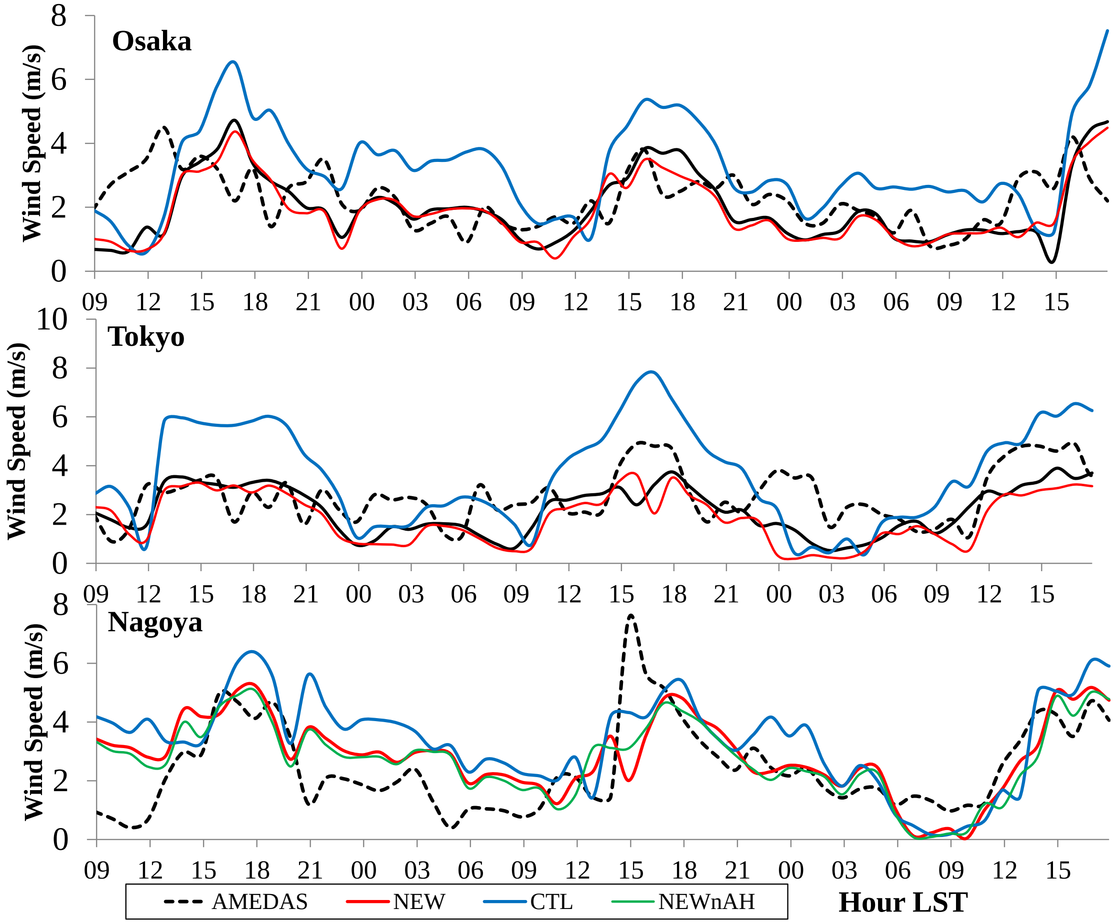

Figure 5-4 3-day observed and simulated wind speed trend from August 10 – 13, 2013

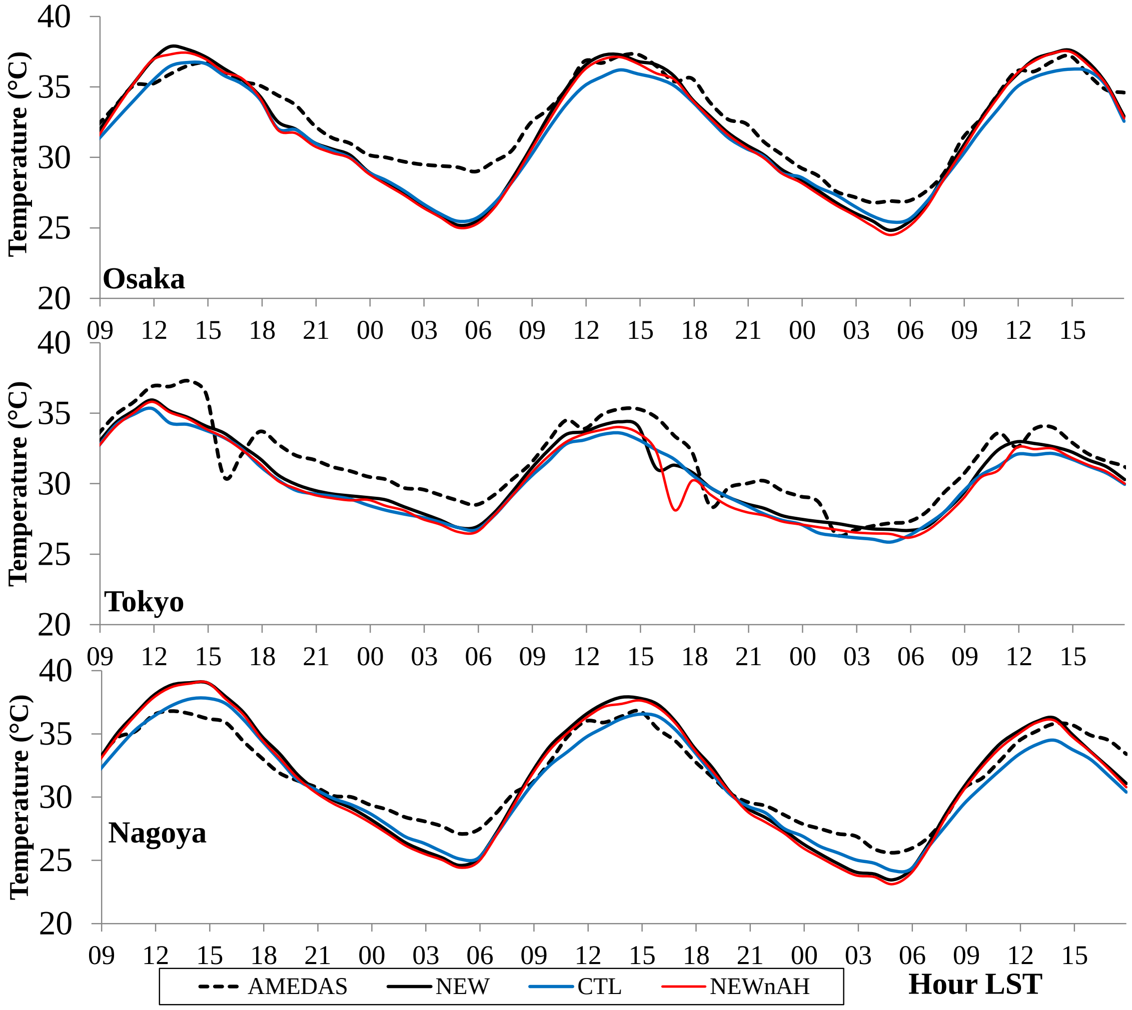

Figure 5-5 3-day observed and simulated T2 trend from August 10 – 13, 2013

5.2.2 Near-surface Temperature

When it comes to temperature simulation, the effect of other improvements aside from *d* and *z0* is also significant. It is interesting that NEW with the exception of Nagoya performs well in simulating diagnostic 2 m temperature, T_2. NEWnAH has the least accuracy for Osaka, Kobe, Tokyo, and Nagoya. This means that NEW improves the wind distribution but needs the AH to have a more accurate simulated temperature. Large differences in simulated temperature between 1500 LST and 1800 LST on August 12, 2013 in Tokyo (Figure 5-5) is brought about by the difference in localized heavy rainfall distribution, not covered in this study. Over-all, T_2 is underestimated by all cases in Osaka and Tokyo throughout the simulation period. Nagoya generally underestimates during nighttime (1800 – 0400 LST) with NEW cases overestimating during daytime (0500 – 1700 LST). Bias was calculated by averaging the difference between observed and simulated 2-m temperature (Observed T_2 – Simulated T_2). Osaka, Tokyo, and Nagoya has daytime (nighttime) biases of 0.35°C(1.40), 0.95°C(1.25), -0.42°C(0.92), respectively, for the NEW. On the other hand, CTL has corresponding daytime (nighttime) biases of 1.03°C(1.43), 1.33°C(1.64), 0.62°C(0.72). Although all cases perform worse during nighttime than daytime, NEW shows improvement throughout all selected stations except for Nagoya for the same reason mentioned in the previous section. The nighttime bias is possibly due to the long-term meteorological boundary bias or the selected physics option. The larger simulated temperature at urban areas in NEW also corresponds to a larger horizontal pressure gradient directed into rougher cities.

5.3 Results and Discussions

Similar to the sea breeze study, the surface wind speed, the wind profile, and the boundary layer height was investigated.

5.3.1 Vertical Profile of Horizontal Winds

Figure 5-6 shows the difference between CTL and NEW wind speed with height above mean sea level (AMSL) averaged throughout the simulation period. The results were interpolated from 80 m to 3000 m AMSL using the Grid Analysis and Display System (GrADS). A few hundreds of meters from the ground, significant difference in wind speed between NEW and CTL could be seen. Close to the surface, wind speed was reduced at an average of 1.75 m/s, 1.28 m/s, 0.73 m/s for Tokyo, Osaka, and Nagoya, respectively. Reduction reached heights of 400 m, 500 m, and 650 m for Nagoya, Osaka, and Tokyo, respectively. Without the AH surface wind speeds at Tokyo, Osaka, and Nagoya are further reduced by 1.89 m/s, 1.49 m/s, and 0.88 m/s, respectively. The result suggests that input roughness parameters are more dominant than AH in influencing surface wind speed. The larger the *d* and *z0m* values the higher the effect from the surface.

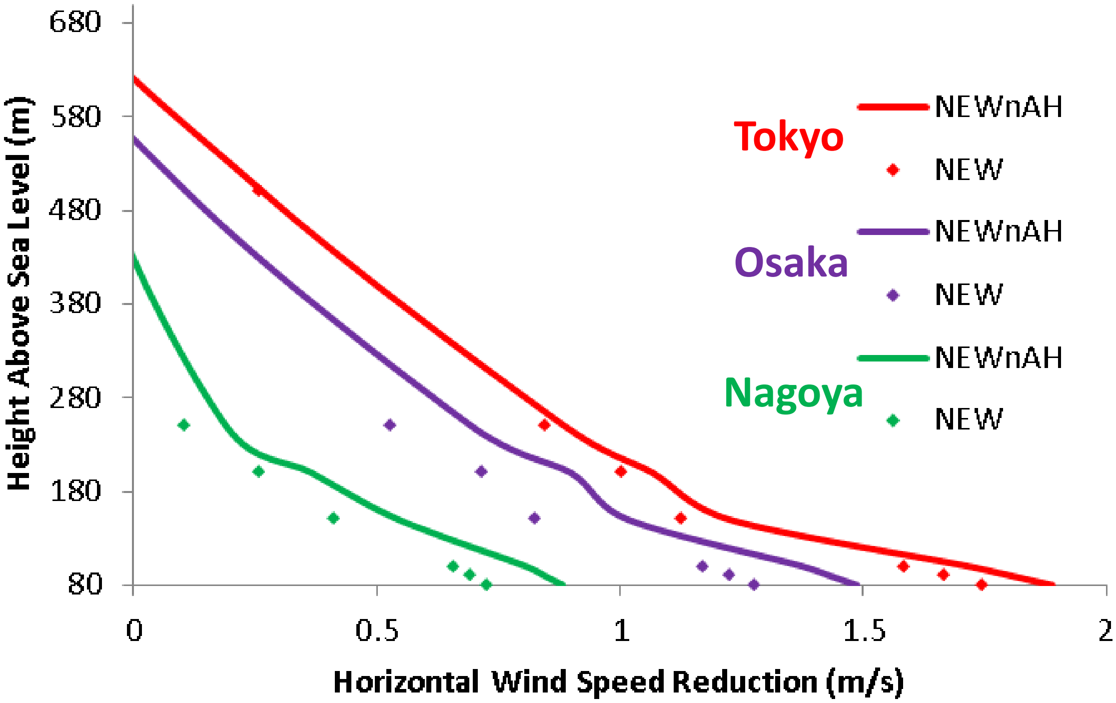

Figure 5-6 CTL and NEW horizontal wind speed difference averaged from 58 hourly data covering August 10 – 13, 2013 (dots); CTL and NEWnAH difference (lines)

Slight increase in wind speed was simulated for the NEW at locations above the reduction region. AHE causes horizontal pressure gradients toward the city. Considering only AHE effect (NEW minus NEWnAH), wind speeds were slightly faster for the NEW. The factor directly influencing the speed reduction high above the boundary layer is difficult to interpret at the current study due to the limited cases and observation capacity. Future validation high above the boundary layer is still needed.

Occasionally, NEW wind speed increases slightly compared to the CTL very close to the surface (80 m, not shown), especially when wind speeds fall below 1 m/s. The instability caused by the warmer temperatures in the NEW causes increase in downward vertical wind speeds and momentum. A similar phenomenon was also observed in an experiment conducted in Poland from 1997-2002 (Fortuniak et al., 2006).

5.3.2 Surface Drag from Roughness

Looking at the horizontal wind speed distribution, drag was intensified in the NEW throughout the simulation period. The surface drag, as shown in Figure 5-7, is significant at locations with large roughness parameters. From noon of August 12, 2013, sea breeze from Osaka Bay penetrated inland. Not depicted in CTL, the winds are reduced due to the presence of buildings (circles in Figure 5-7). As the warm land continues to promote inflow, winds leeward from the building once again increase in intensity while surface layer winds at urban areas remain to be less intense throughout for the NEW. The effect of roughness parameters to the front can be seen from the convergence line. The disturbance distorts the front on urban areas in contrast with the CTL – convergence region perpendicular to the flow remains to be obvious.

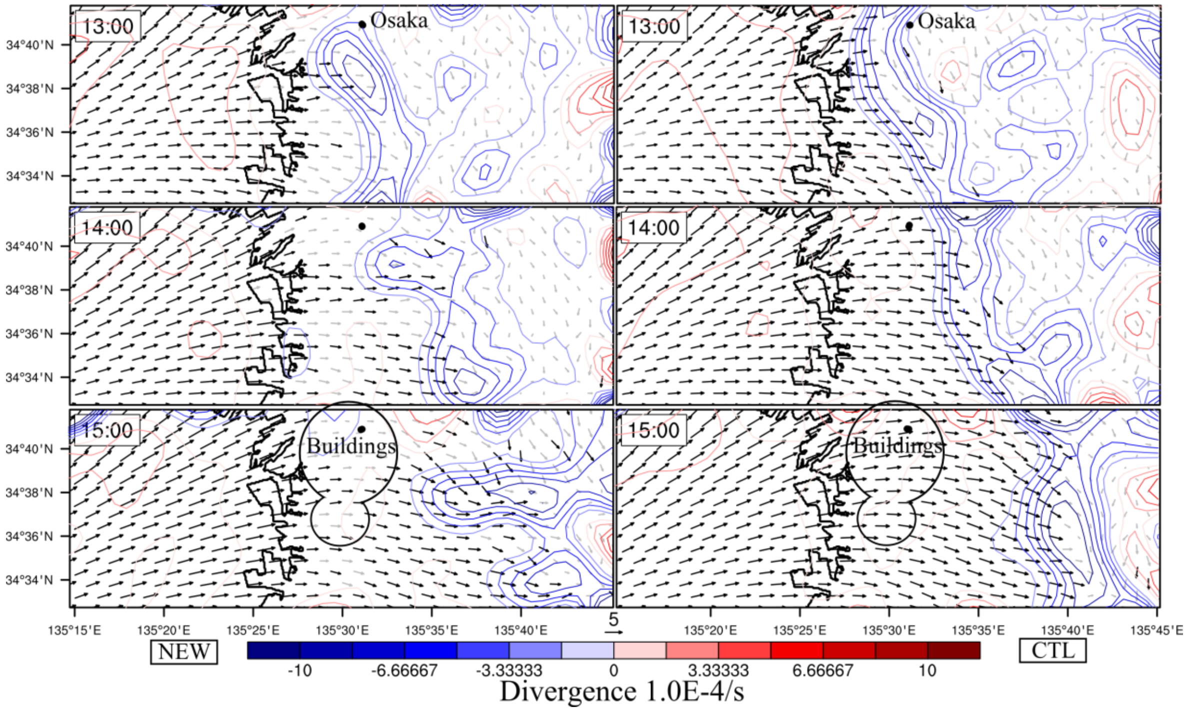

Figure 5-7 August 12, 2013 hourly snapshot of 10 m sea breeze flow (dark wind vectors > 3 m/s), and 1st atmospheric level divergence (contours) towards Osaka for NEW and CTL

The same phenomenon was observed in Tokyo and Nagoya. A convergence region (blue ovals on Figure 5-8) prevails directly at the boundary between Tokyo and its bay which was not observed in Osaka for two reasons behind this. First is because Tokyo has larger and wider *d* and *z0m* than Osaka. Second is because large *d* and z_o lies closer to the coastline blocking incoming winds. Aside from sea breeze, northwesterly wind was also reduced as it approached Nagoya city. The tall buildings at Nagoya affect the surrounding wind circulation (not shown).

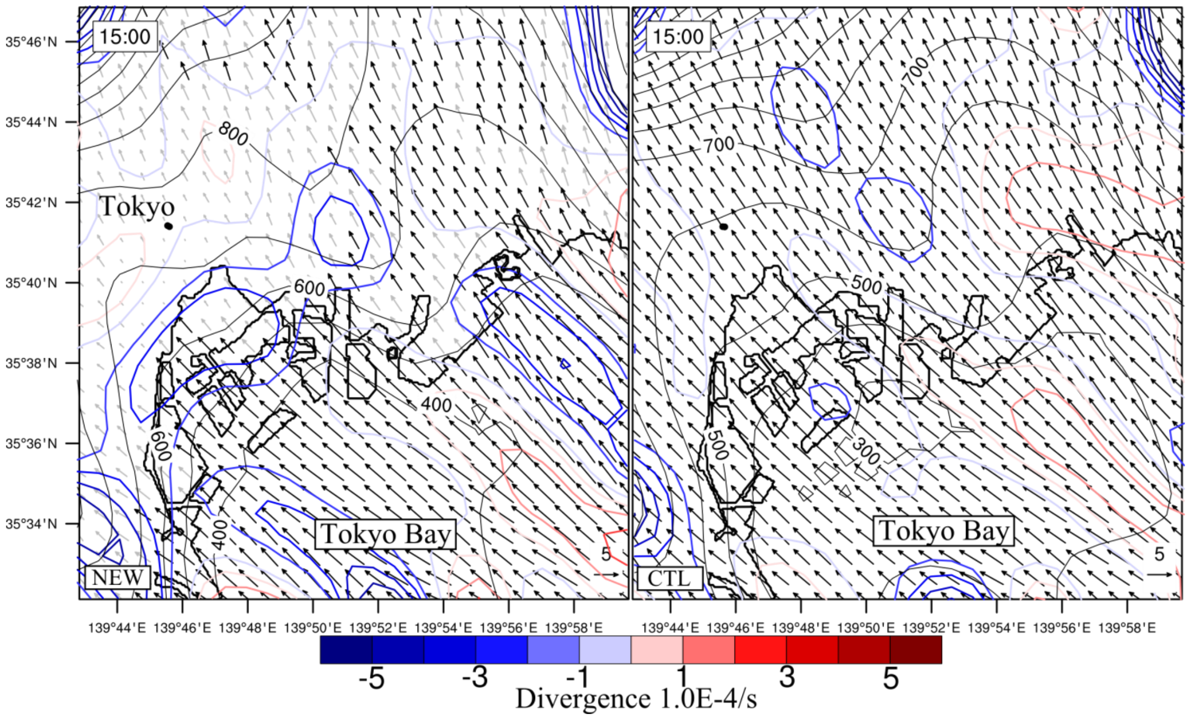

Figure 5-8 August 11, 2013 hourly snapshot of 10 m sea breeze flow (dark wind vectors > 3 m/s), PBLH (solid black lines) and 1st atmospheric level divergence (colored lines) for NEW and CTL

Fortuniak, K., Klysik, K., Wibig, J., 2006, Urban-rural contrasts of meteorological parameters in Lodz, Theor. Appl. Climatol., 84, pp. 91 – 101

5.3.3 Atmospheric Boundary Layer

NEW resulted to a higher boundary layer height (PBLH) compared to CTL. The PBL built-in physics scheme used was the Mellor-Yamada Nakanishi and Niino Level 2.5. In Figure 5-9, the Tokyo metropolitan area shows ~100 m higher for the NEW at 1500 LST. Because of the limited sensitivity cases, the individual contribution of each parameter to the PBL evolution cannot be clarified at the current study stage. Nonetheless, the little changes in heat flux and the increased 1st level convergence in NEW hints on the possibility that forced convection, directly affected by input roughness parameters, has significant influence to the PBLH. Forced convection above the city also affects the PBLH as depicted in the PBLH difference between NEWnAH and NEW (Figure 5-9).

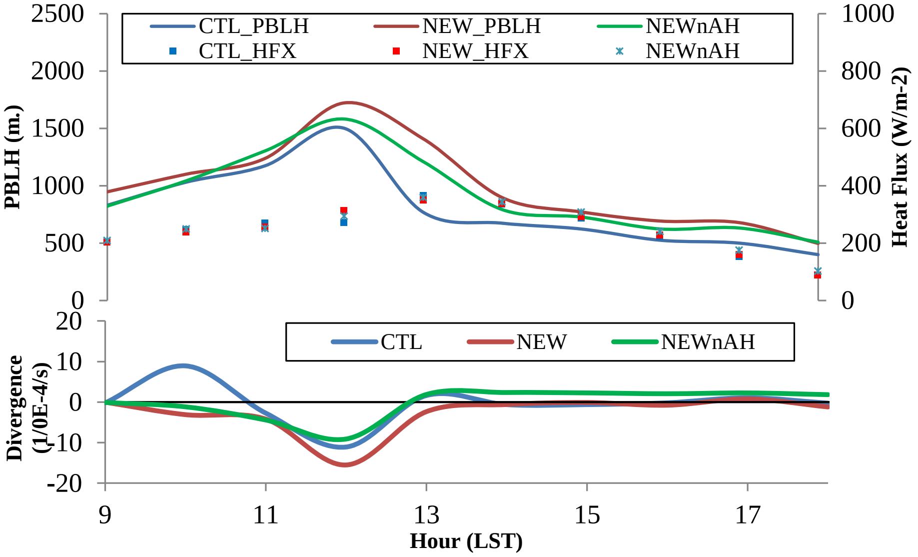

Figure 5-9 August 11, 2013 trend of PBLH, sensible heat flux (HFX), and 1st atmospheric level divergence in Tokyo AMeDAS station

5.4 Chapter Summary

After having satisfactory results in the reproducibility of near-ground winds in the previous chapter, the model application was then extended at other dates and other major cities. This was motivated by the recent development of a nation-wide distribution of roughness and anthropogenic heat parameters by Makabe et al. (2014). Furthermore, it is through this chapter where the anthropogenic influence to winds is compared to the aerodynamic roughness effects. Results show from a 3-day simulation of August 2013 that the updated WRF simulated a better near-wind compared to the default version of WRF. The drag effects are proportional to the roughness parameter values. The delay and distortion of sea breeze was also confirmed in Osaka. Finally, anthropogenic heat can increase slightly the wind speeds but was not as significant as the aerodynamic roughness.

6 Sensitivity of WRF Model to Roughness Parameters and Sky-view Factor using a 2-dimensional Idealised Case

This chapter was finally added during the latter phase of the dissertation motivated by the necessity to answer a few questions which arose from the previous chapters' findings. Although roughness was found to largely reduce the wind speed (for urbanized areas due to momentum drag brought about by large roughness length for momentum) and slightly increase temperature gradient (due to the reduced heat exchange brought about by lesser roughness length for heat) in major cities in Japan, the proportions of influence of each urban parameters, d, z_o, and sky-view factor were not fully discussed.

There are three reasons why the contribution of each parameter was not clearly established in the previous chapters. First and foremost, the focus was to showcase the improvements of the modified WRF model proposed. The modified WRF showed better results in terms of wind field accuracy as proven in the previous chapters. Second, the most significant improvement was on the parameterisation of d and z_o owing to the works of Kanda et al. (2013). Third, the test simulations highlighted in the previous chapters were based on real weather phenomena with a lot of factors affecting the results such as land use distribution, initial and lateral boundary conditions, the influence of other physics, and so on. This non-linear nature of the model was the reason why moisture, energy balance, or humidity, was not taken into account in the validation.

In this chapter, three sensitivity studies were conducted by idealizing the modified WRF model. The meteorological parameters analysed are wind speed, mixing ratio, and heat and momentum fluxes. It is to be carefully noted that this idealized WRF is not similar to the available ideal cases of WRF (e.g. em_b_wave, em_fire, em_heldsuarez, em_les, em_seabreeze2d_x) mainly because the provided WRF ideal cases do not allow flexibility in setting up physics and the domains. The procedure for doing this is discussed in the numerical settings.

6.1 Numerical Settings

The WRF version used was the modified WRF model represented by the NEW cases in the previous chapters. The first step was to remove the coriolis and curvature effects in the model to create a sea breeze front parallel to the coastline throughout. Doing this was done through the adjustment of the map scale factor (responsible for the location and projections) to 1.0 and setting the earth's radial influence and coriolis terms to zero.

After removing coriolis and curvature effects, static surface boundaries and meteorological boundaries were adjusted to simulate desired weather condition. To control the domain without adjusting the external datasets, output netcdfs from geogrid.exe and metgrid.exe (refer to Figure 3-1) were revised directly using a programming language.

6.1.2 Geographical set-up

Relevant to this study is the land use and urban parameter distribution. To simplify the surface domain, only two land use classifications were considered: homogeneous urban surface for land, and water for the sea. The ratio between sea and land is 1:3 as shown in Figure 6-1. The scale of the domain was retained such that the horizontal coordinates are in degrees longitude (for *x*) and degrees latitude (for *y*). With 150 grids in both *x* and *y*, the grid spacing was set to 1.0 km. The vertical resolution is also decreasing with height similar to previous chapters (refer to Table 4-1 for eta levels). The geographic coordinates are necessary to estimate the incoming shortwave radiation. Because of this, land was situated at the eastern side of the domain to ensure that it is heated a few minutes earlier than the sea. The urban area has a 0.90 urban fraction with 0.10 allotted for grassland. The ground surface height above mean sea level is 1.0 m. The albedo set for urban land and sea were 15 % and 8 %, respectively. The emissivity was 0.88 for land and 0.98 for water.

To understand the influence of each parameter, sensitivity studies were conducted by varying displacement height (4 cases), varying roughness length for momentum (3 cases), and varying sky-view factor (3 cases). In setting up the displacement height, the same method introduced in chapter 3.2 was used. The default value of 5.731 m was added to the ground topography for all cases except for the cases with varying displacement heights. A default value of 0.33 m for the z_o was used except for the cases with varying z_o. A default value of 0.48 m was used for the sky-view factor except for the cases with varying sky-view factor.

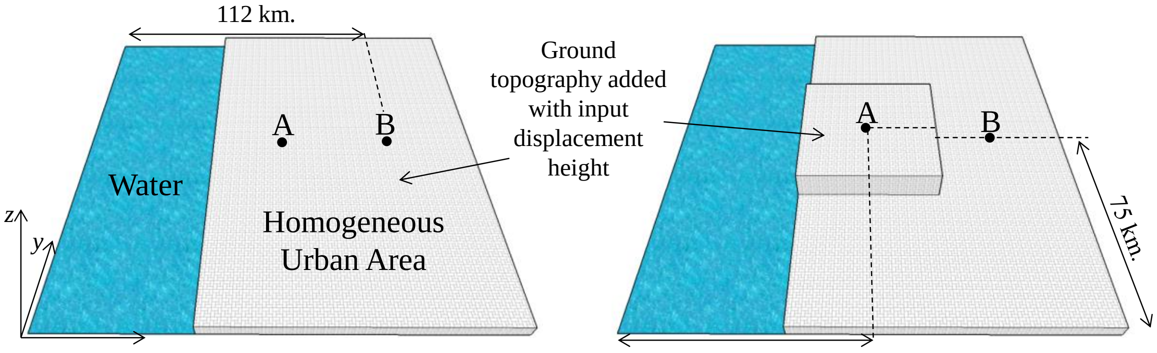

Figure 6-1 General domain configuration. (Left) Cases with no varying displacement heights. (Right) Cases with varying displacement height.

For the cases investigating the effect of *d*, the values of no displacement (nodisp), 5.71 m (displow), 25 m (dispmid), and 50 m (disphigh) were tested. For the cases investigating the effect of z_o, the values of 0.33 m (zlow), 5 m (zmid), and 10 m (zhigh) were tested. Lastly, the values of 0.23 m (svflow), 0.48 m (svfmid), and 0.65 m (svfhigh) for the sky-view factor were tested. Each effect is discussed in the next sections.

It must be carefully noted that in reality the roughness parameters and sky-view factor are inseparable parameters; such that, large *d* corresponds to a larger z_o but never exceeding it; and, rough grids tend to have lower sky-view factor values. Since the aim of this chapter is to determine how each parameter affects the model, their relationship is temporarily neglected and extreme values are used. A careful consideration of this issue is recommended, however, in the future analyses.

6.1.3 Meteorological set-up

Prior to running wrf.exe, 16 vertical levels of meteorological inputs were considered. Meteorological parameters were acquired from the background meteorology of the sea breeze simulation in chapter 4. In other words, the meteorology for September 13 and 14, 2011 were used as reference. Spatially uniform time-varying (three hour interval) values were assigned for each level. Trends for pressure, relative humidity, and input potential temperature (decreasing with height) are shown in

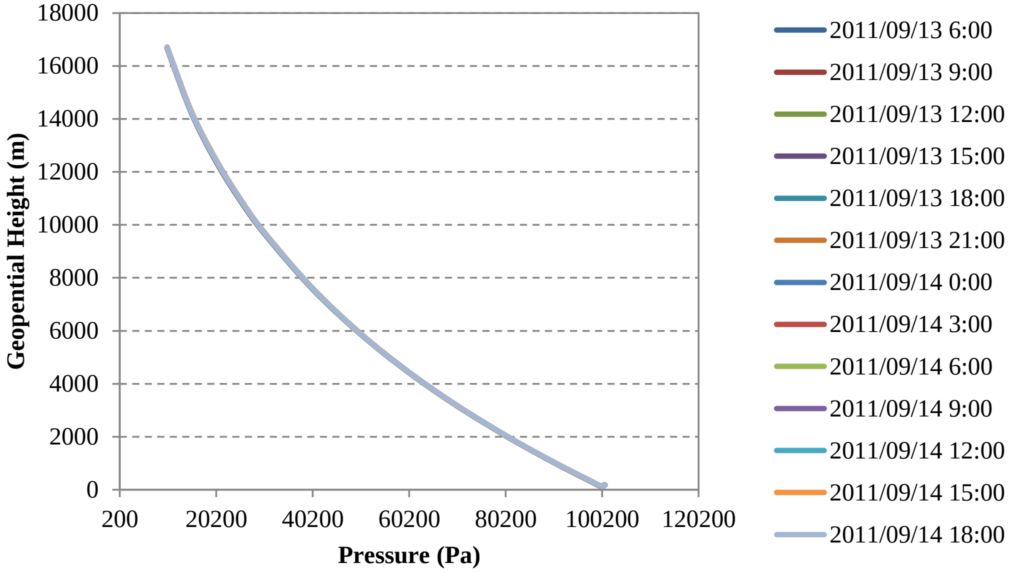

Figure 6-2, Figure 6-3, and Figure 6-4, respectively. Inflow winds (UU and VV) were set to 0 m/s. Only the sea surface temperature and skin temperature vary between land and sea (refer to Figure 6-5). The same meteorological inputs were used for all cases employed in this chapter. All simulations had a one day spin-up period.

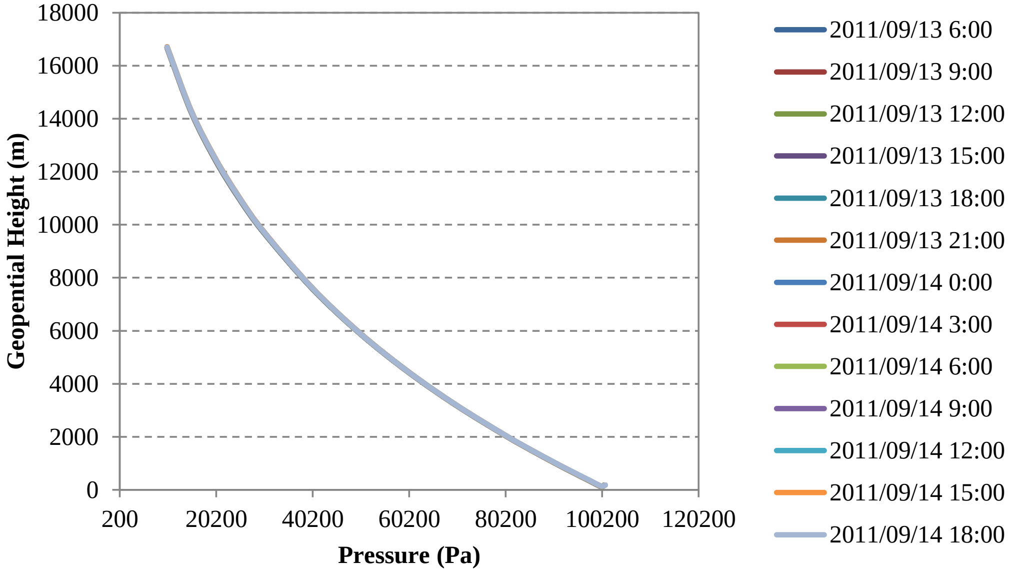

Figure 6-2 Input pressure. Time is in UTC (LST minus 9 hours)

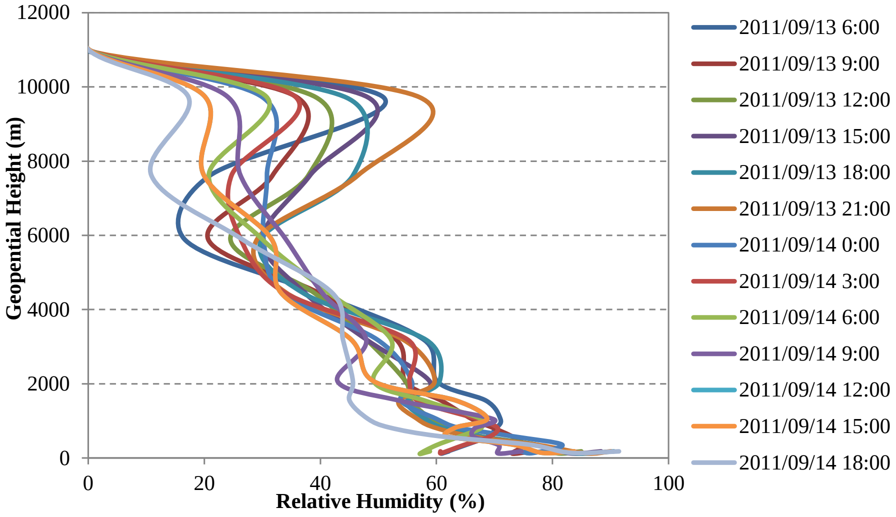

Figure 6-3 Input relative humidity. Time is in UTC (LST minus 9 hours)

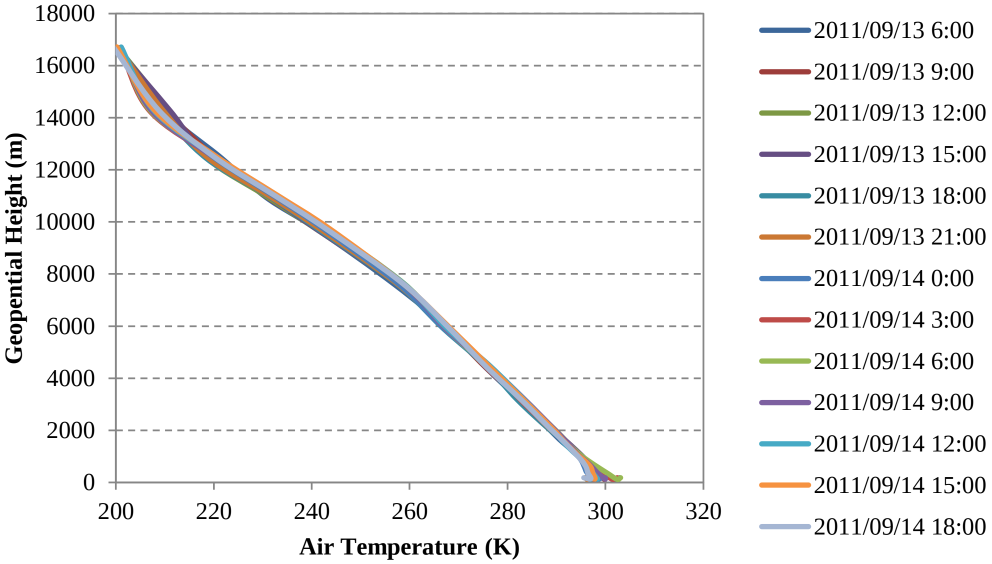

Figure 6-4 Input air temperature. Time is in UTC (LST minus 9 hours)

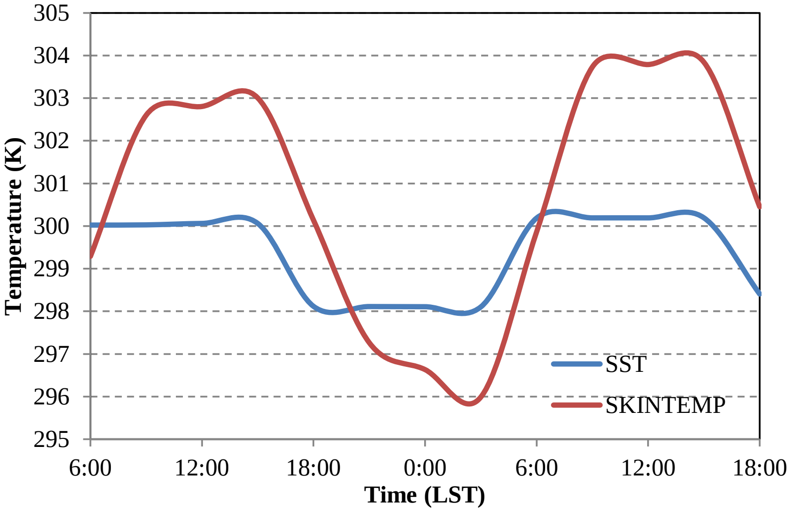

Figure 6-5 Input sea surface temperature (SST) and land skin temperature (SKINTEMP) from 6 AM of September 12, 2011 to 6 PM of September 14, 2011

6.2 Results and Discussion

6.2.1 Effect of Roughness Parameters *d* and *z0m*

Previous chapters mention the combined effect of *d* and z_o because of in real conditions they are indeed inseparable. Rough buildings, brought about by the height variability and the average height, displaces the logarithmic wind profile from the surface at the same time affect its structure by reducing the speed. Through the idealization of WRF, the separate influence of *d* and z_o can be assessed. Which between the two parameters is the model more sensitive to?

First, varying *d* was tested using the default z_o (0.33 m). Refer to section 6.1.2 for the case nomenclature. Since the effect of *d* becomes similar to topography and has little purpose when added throughout urban domain, only a selected region was considered for *d* to vary, as shown in Figure 6-1. The influence to the parameters above region of varying *d* (upper figures of Figure 6-6) is less significant as compared to the cases of varying z_o and sky-view factor (shown later). Vapor mixing ratio drops from 7 in the morning to 0.015 kg / kg, and remaining constant to this level from 10 in the morning similar for all cases at pt. A. Wind steadily increases with slightly faster wind speeds at higher displacement height values. A *d* of 50 m (disphigh) shows minimal differences compared with calses of small *d* values. Heat flux differences could also be seen during mid-day but still not very significant due to the meagre height displaced compared to the height of the planetary boundary layer. The differences are probably caused by the unstable boundary layer during daytime.

The *d*, however, affects significantly the surrounding areas from the displaced region, such as pt. B (bottom figures of Figure 6-6). For example, large differences in wind speed and heat flux could be seen above pt. B due to the differences in convergence occurring behind the displaced area. This is similar to a hill’s influence to an incoming breeze where the impact is mostly observed behind the hill. This was the case for Tokyo and Saitama where sea breeze convergence behind Tokyo was affected by the large *d* values.

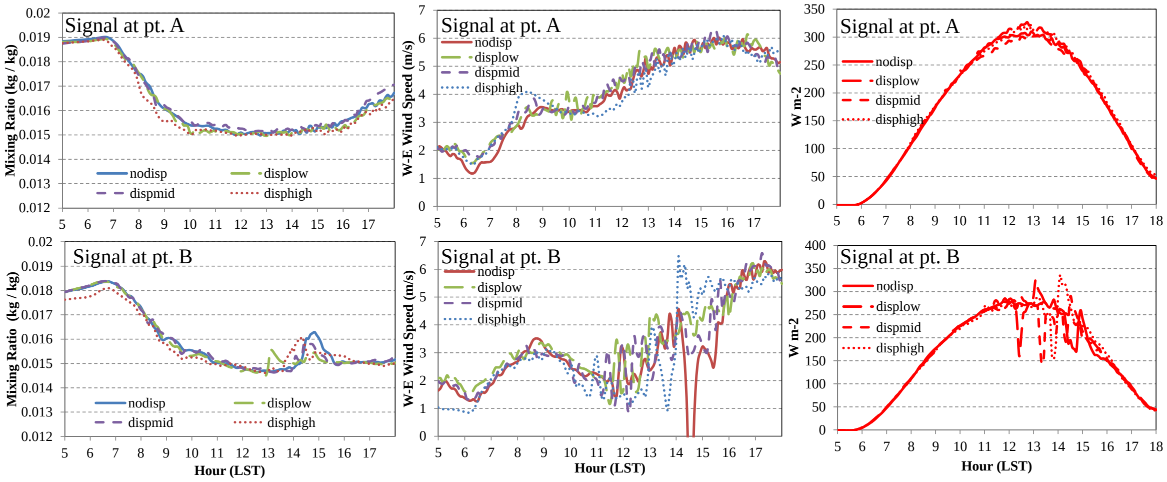

Figure 6-6 Simulated meteorological parameters for each case and location, where: (Leftmost) first atmospheric level vapor mixing ratio; (Middle) first atmospheric level west-east wind component; (Rightmost) sensible heatflux. Top and bottom figures are hourly signals for pt. A and pt. B, respectively.

From the findings about *d*, it can be deduced that z_o has larger influence to the wind speeds and momentum fluxes at pt. A. Refer to section 6.1.2 for the case nomenclature. zhigh is typical value for Shinjuku, zmid is typical for Tokyo metropolitan area, and zlow is typical for rural areas and default WRF. Truly, the impact of z_o is much more significant (see the case differences in Figure 6-7) to reduce the wind speed for both points A and B up to as high as 3 m/s. Results to differences in wind speed less than 1.0 m/s. The large reduction of wind speeds reflects to lesser heat and momentum exchange in the surface (smaller values of vapor mixing ratio and sensible heat flux). Sudden drops or breaks in the heat flux can be attributed to the cloud formation. It must be carefully noted that in spite the reduced heat flux, there is still a tendency for zhigh to have a larger thermal low than zlow due to the larger skin temperature (and thus air temperature).

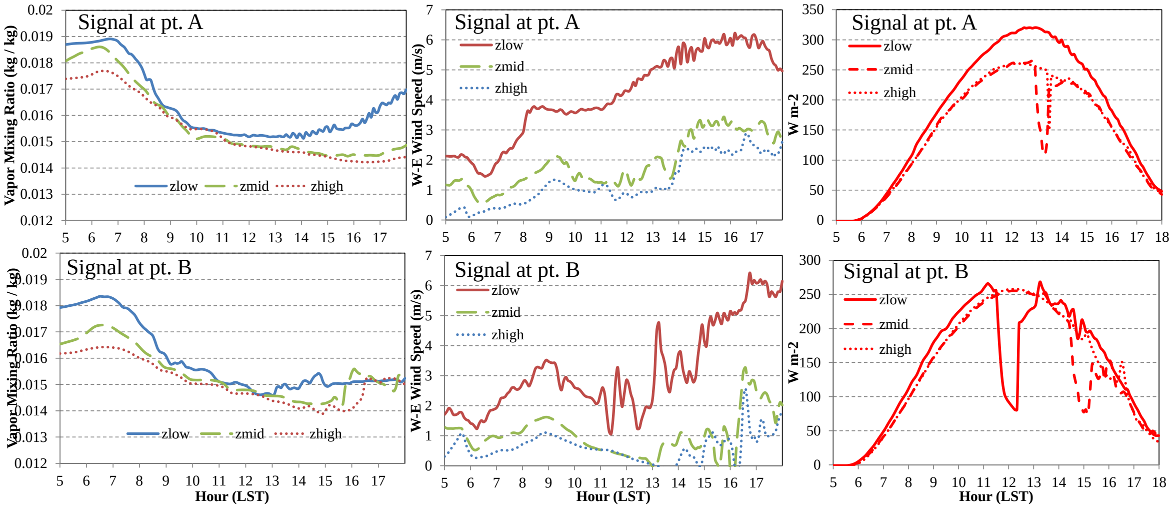

Figure 6-7 Simulated meteorological parameters for each case and location, where: (Leftmost) first atmospheric level vapor mixing ratio; (Middle) first atmospheric level west-east wind component; (Rightmost) sensible heatflux. Top and bottom figures are hourly signals for pt. A and B, respectively.

Obeying to the logarithmic wind assumption, effects brought about by z_o lessen with larger z_o. For example, large differences in heat flux could be seen (around 50 W m-2) between zlow and zmid but almost no differences (unless clouds form) between zmid and zhigh. In Figure 6-8, the dominant influence of z_o over *d* could also be seen. Delays and reduction to the trailing winds could be seen for zmid and zhigh but not prominent for cases of varying displacement heights. The slower winds above the sea for the zmid and zhigh are brought about by feedback from the previous day's simulation. In zhigh, the reduction in heat flux from the surface reduces free convection which is why clouds, unless at the front, are not formed compared to the other cases.

To confirm the findings in *d*'s minor influence to the intensity of meteorological parameters, spatial average of the simulated values at the first atmospheric level over land was calculated. It can be seen in Figure 6-9 that the differences are not very significant when the whole domain is considered for each case. Slight differences in the wind speed can be distinguished due to the effect of *d* to the terrain.

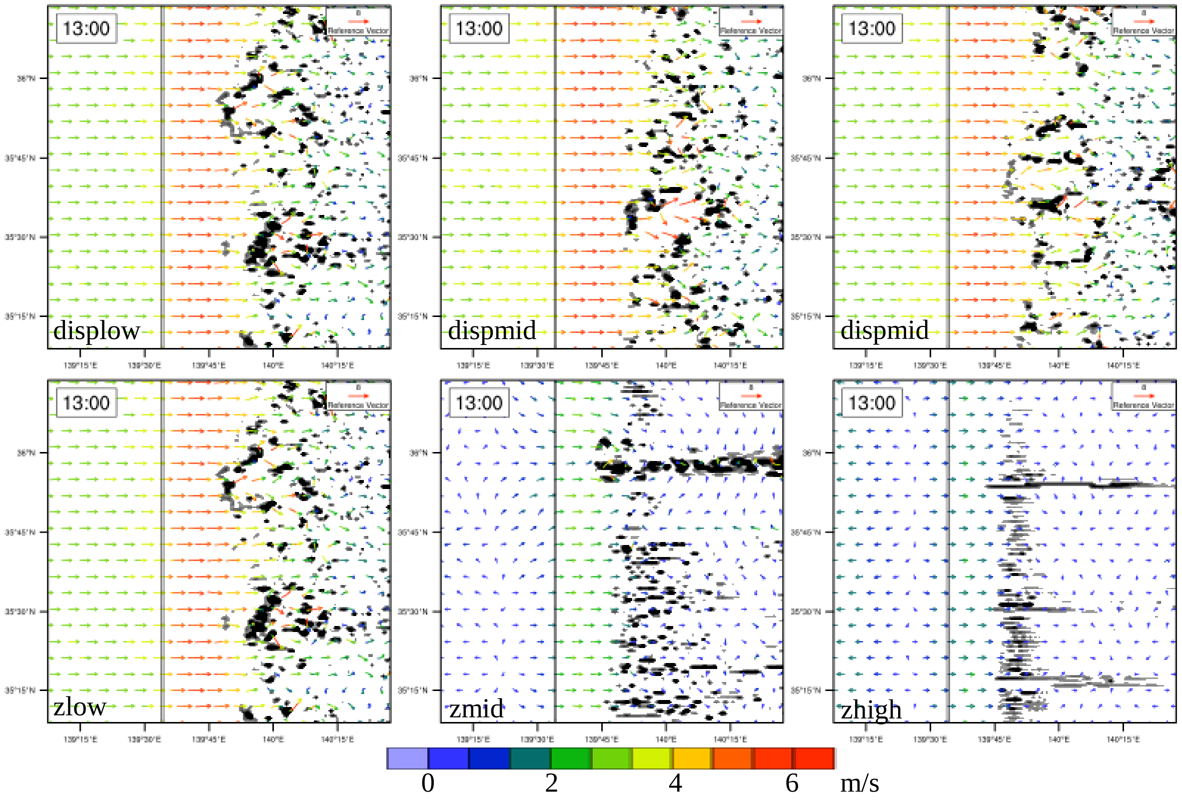

Figure 6-8 Simulated first atmospheric winds (colored vectors) and total colulmn cloud mixing ratio (shaded) for various cases at 1300 LST.

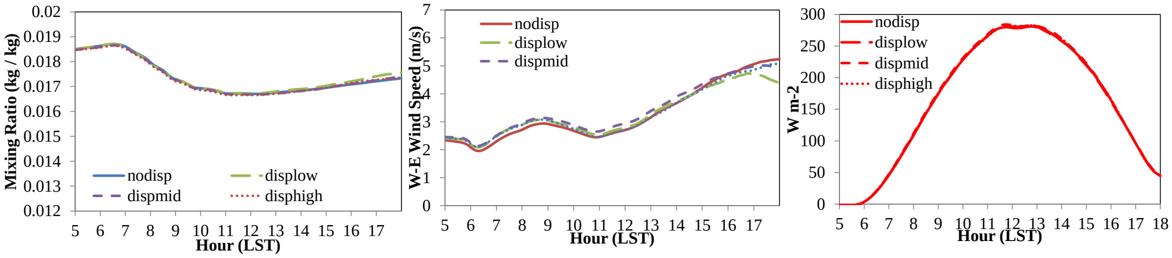

Figure 6-9 Simulated meteorological parameters spatially averaged over land, where: (Leftmost) first atmospheric level vapor mixing ratio; (Middle) first atmospheric level west-east wind component; (Rightmost) sensible heatflux.

6.2.2 Effect of Sky-view

As mentioned in section 3.3.3, the sky-view factor is estimated in the UCM using the λ_p and the λ_f. λ_p and λ_f are also invoked in eqn. 2, 3, 4 and 5 of section 2.3.3 which were used to estimate *d* and z_o. This analogy suggests the close relationship of aerodynamic roughness parameters, *d* and z_o, and sky-view factor. Using the similar analysis procedure from the previous section, the sky-view factor effects can be assessed by fixing the aerodynamic parameters. Refer to section 6.1.2 for the case nomenclature.

The sky-view factor has a slightly reverse effect to z_o. The larger the sky-view factor, the more radiation released via heat flux (Figure 6-10). The higher the heat flux, by 50 W m-2, being released also generates faster winds due to the enhance temperature gradient between land and sea. With barely 0.40 difference between svflow and svfhigh, 1 m/s can be observed at pt. A. However, there’s almost no difference in intensity between zmid and zhigh.

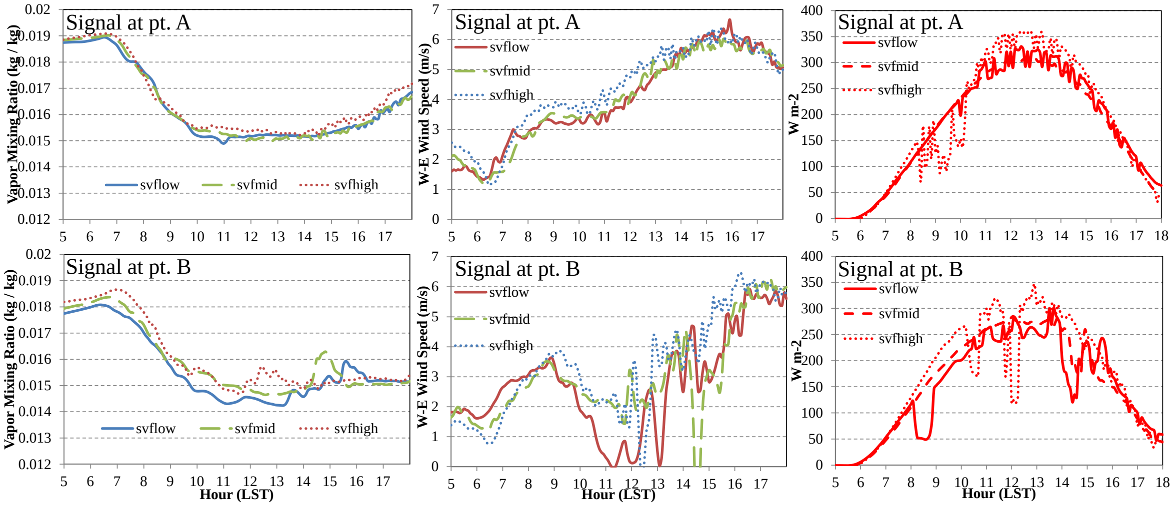

Figure 6-10 Simulated meteorological parameters for each case and location, where: (Leftmost) first atmospheric level vapor mixing ratio; (Middle) first atmospheric level west-east wind component; (Rightmost) sensible heatflux. Top and bottom figures are hourly signals for pt. A and B, respectively.

Knowing that the sky-view factor has an influence in the aerodynamic field, the question how significant the effect is in actual urban setting arises. To understand this requires the merging of the previous section's findings regarding the variations of d and z_o. It is understood that the z_o is more dominant over d. Consequently, the influence of z_o in urban areas is also more dominant than the sky-view factor. Why is this? At urban areas such as Tokyo, the sky-view factor is low with higher z_o. Further, there is little difference in the default sky-view factor and the revised one (Figure 3-5) than the default z_o and its revised value (Figure 3-2) at urban areas. Along with the statements in section 3.3.3 regarding the reduced influence of larger and revised sky-view factor at non-urban dominant grids due to the *urb*_frc, the finding in this section supports the bold assumption that the improvements mentioned in section 3.3 have lesser impact to the simulation than the improved aerodynamic roughness parameters, themselves. In spite this, it is still recommended to use the revised version of sky-view factor with the realistic aerodynamic roughness parameters.

6.2.3 Sensitivity of Boundary Layer Height

The sensitivity of the simulated boundary layer height to the parameters is discussed. This section is important to determine up to which extent above ground each parameter affects the atmosphere. The evolution of the boundary layer for selected cases can be seen in Figure 6-11. Depressions are brought about by the clouds. The terrain-like effect of d can be seen in the development and decline of boundary layer height. An earlier jump downwind of the displaced region can be seen in the morning (see B at 10:00 LST). The delayed penetration of sea breeze brought about by the blocking of the displaced area in the afternoon also tends to hinder the suppression of the boundary layer (see B at 17:00 LST).

The effect of z_o again makes the largest impact to the boundary layer height. Due to the higher transfer coefficient of heat, lower z_o tends to have a faster boundary layer growth in the morning (see C and D on 10:00 and 12:00 LST). The higher z_o continues to supply heat into the urban boundary layer at a steady rate until later in the afternoon even at lower heat flux. At 17:00 LST, the lower z_o allows a faster sea breeze penetration compared to the higher z_o. This phenomenon contributes to the finding that rough areas tend to have higher boundary layer in spite lower heat flux late in the afternoon. The drag effect on sea breeze and the steady supply of heat from the surface result to a higher boundary layer. Finally, the differences in the sky-view factor have some influence similar to z_o but not as much. The smaller the sky-view factor the shorter and slower the boundary layer height becomes.

6.3 Chapter Summary

To understand the individual effect of the urban parameters, and idealized simulation of sea breeze was conducted. This idealized model utilizes the full features of WRF, with the same domain resolution, and model physics options as the previous chapter. Until the previous chapters, roughness was defined by the combined effect of inseparable parameters, displacement height and roughness length for momentum. Furthermore, any sensitivity to the sky-view factor was not considered. This chapter answers the question how the three parameters (displacement height, roughness length for momentum, or sky-view factor) influence WRF. It was found that the displacement height tends to create a terrain effect but has negligible effects to the energy balance. Large roughness length for momentum is the most dominant parameter which influences the simulated wind field thereby also affecting the boundary layer height evolution the most A lower sky-view factor at urban areas also may reduce the wind speed compared to the default value due to the trapping of radiation near the surface but not as significant as the roughness length for momentum (chapter 6).

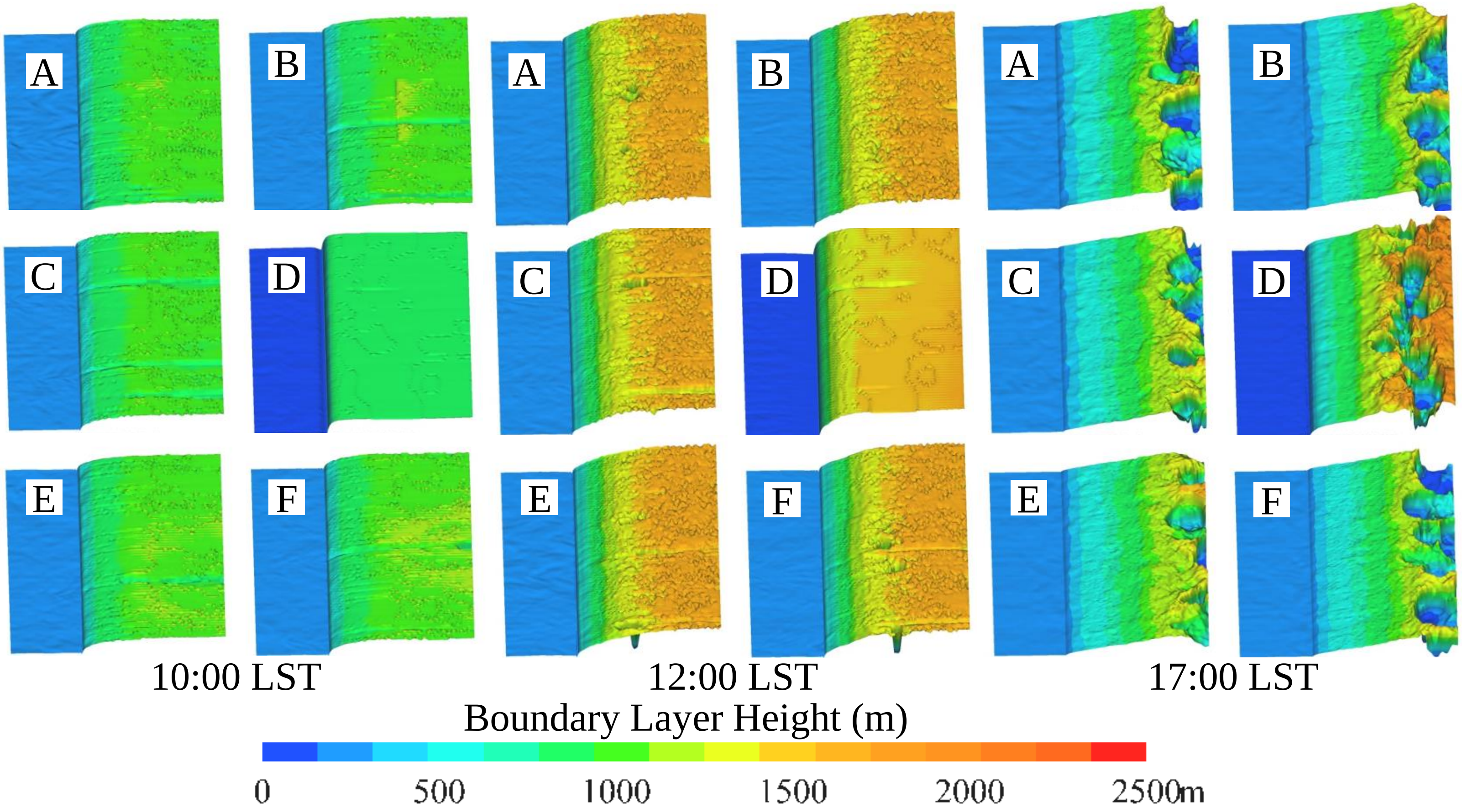

Figure 6-11 1000 LST, 1200 LST, and 1700 LST snapshots of the distribution of boundary layer height for cases: displow (A), disphigh (B), zlow (C), zhigh (D), svmid (E), and svfhigh (F)

7 Conclusion

There remains limited understanding regarding the impact of buildings to weather at the mesoscale level due to inadequate representation of weather models. This study addressed the issue of wind field inaccuracy by weather models through the incorporation of new aerodynamic roughness parameters and its advance parameterisations into the Weather Research and Forecasting Model (WRF).

A distribution of aerodynamic roughness parameters, derived from new LES-derived aerodynamic feedback parameterisation, was prepared and included into the single-layer urban canopy model. A 1-kilometre distribution of d and z_o was prepared for Japan and tested on a sea breeze event using the WRF model (Objective 1 and Objective 2). The new values of d and z_o that were calculated for Tokyo reached around three times larger than the conventional values used in WRF. The updated model, comprising the new aerodynamic parameters, and the default WRF model (difference between default and updated model shown in Table 4-1) were compared.

The updated model was evaluated (Objective 3) using a two-month simulation focused on dry days. Simulated wind speeds were found to match ground observations well especially at urban areas. A difficulty remains in the calculation of the diagnostic 2-m temperature, with the updated version overestimating observed values. The deviations were possibly due to the representativeness of 2-m temperature observation gauges. The new parameters improved the simulation of clouds compared with images from a high-spatial-resolution geostationary satellite.

The influence of the distribution of new aerodynamic roughness parameters are listed as follows (No. 1– 6 achieved objective 4; No. 6–9 achieved objective 5) :

1) Surface wind speeds behind the sea breeze front weaken in highly urbanised areas like Tokyo and its neighbouring cities due to the significant drag from the surface (chapter 4 and chapter 5).
2) Wind speed can be affected up to significant heights within the boundary layer, also affecting cloud formation (chapter 4 and chapter 5).
3) The strong convergence/divergence region to the north of Tokyo widens due to the weakened sea breeze (chapter 4).
4) A more intense elongated convergence region caused by increased roughness, sea breeze, and heat island circulation was simulated and extended from Tokyo to the inland (chapter 4).
5) The findings in Tokyo were also confirmed in other major cities throughout Japan, such as Osaka and Nagoya (chapter 5).
6) The influence of anthropogenic heat emission was found to be subordinate to the proposed aerodynamic roughness parameters in simulating the wind field (chapter 5).
7) The displacement height tends to create a terrain effect but has negligible effects to the energy balance (chapter 6).
8) Large roughness length for momentum is the most dominant parameter which influences the simulated wind field thereby also affecting the boundary layer height evolution the most (chapter 6).

9) A lower sky-view factor at urban areas also may reduce the wind speed compared to the default value due to the trapping of radiation near the surface but not as significant as the roughness length for momentum (chapter 6).

Inaccuracies in the simulation of wind and cloud in some areas were generated by insufficient roughness parameter data and model sensitivity to the assumed settings (e.g., meteorological and surface boundary conditions, physics options, domain size). Although beyond the scope of this study, the possible causes of prevalent inaccuracies need to be addressed and further testing on other parameters such as moisture and rainfall is necessary.

The contributions of this research to the research community and society are as follows:

1. Knowing that sea breeze penetration inland can be influenced largely by the urban conditions upstream, conventional models might be underestimating the actual impact of urban areas to extreme weather conditions like localized heavy rainfall and heat wave;
2. Due to the ability to vary the roughness distribution of the single-layer urban canopy model, the updated model can be a wise alternative for developing countries where observations and research are limited;
3. Propose improvements to the widely used open-source WRF model;
4. In terms of urban planning, the improved model can allow testing of various building configurations unlike the former single-layer urban canopy model where this option is previously unavailable;

5. With the improvements and findings contained in this study, the model usage will also enable decision makers to create policies that will counter the negative effects of urbanization.
6. The findings in this study could assist in the determination of appropriate representative sites for observation.

Appendix

A. Individual influence of geometrical parameters to *d* and z_o

Tests were conducted using the equation introduced in chapter 3. Figure A-1 shows the possible combination of *d* and z_o with increasing H_{ave} (5 m to 50 m at 5 m interval), increasing λ_p and λ_f (0.1 to 1.0 at 0.1 m interval). For KA2013, H_{max} was set equal to H_{ave} and σ_H set to zero to look only at uniform arrays. Increasing frontal area index increases the magnitude of the z_o at a given *d*. Increasing the plane area index increases the *d* at a given z_o. Increasing the H_{ave} increases both *d* and z_o.

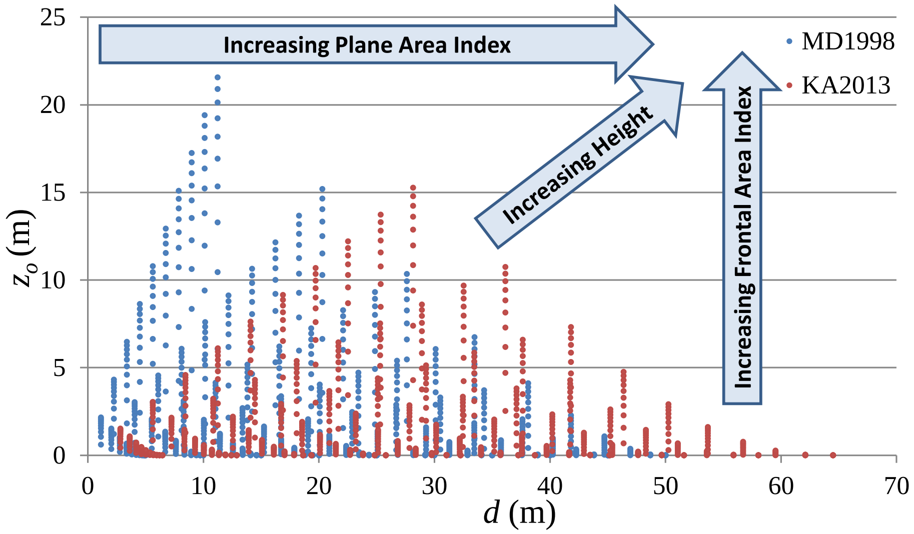

Figure A-1 Combination of possible values of *d* and z_o for uniform arrays using MD1998 and KA2013

Figure A-2 shows the possible combination of *d* and z_o for increasing H_{max} and σ_H while fixing other geometrical properties. H_{ave} was set to 10 m while λ_p and λ_f were set to 0.5. The difference between H_{max} and H_{ave} increases the magnitude of *d*. However, the influence of a very tall H_{max} decreases as it departs to far from the H_{ave}. On the other hand, large σ_H tends to have a larger z_o.

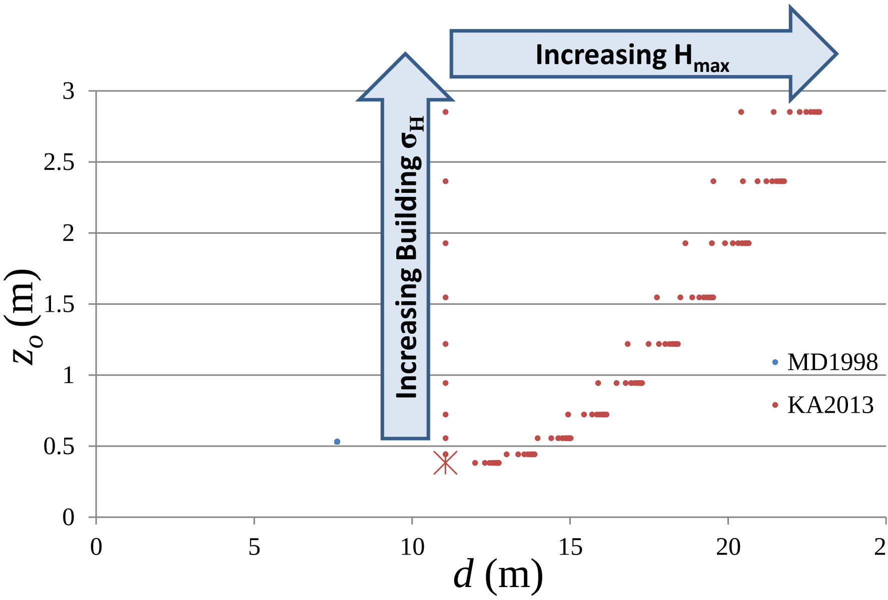

Figure A-2 Combination of possible values of d and z_o using MD1998 and KA2013 with varying H_{max} and σ_H for fixed H_{ave}, λ_p and λ_f. Red asterisk represents uniform array condition.

B. Default vs. proposed estimation of sky-view factor

The default sky-view factor used in this study, 0.48, was based on a formulation by Kusaka et al. (2001) for a 2-dimensional canopy. It was calculated from the normalized height (roof height divided by the sum of road width and roof width) and the normalized roof width (roof width divided by the sum of road width and roof width). The assumed roof height, road width, and roof width, are 7.5 m, 9.4 m, and 9.4 m, respectively.

Comparing with the proposed calculation of sky-view factor in section 3.3.3, the λ_p and λ_f can be used as substitute for the normalized roof width and normalized height, respectively. Figure B-1 was created by varying values of λ_p and λ_f, ranging from 0.1 to 0.9 at 0.1 intervals, into the default and proposed equation. Slight overestimation in the 2-dimensional assumption of sky-view factor can be seen when compared with the method of Kanda et al., 2005a. Based on the correlation plot, a quadratic correction can be applied in the future to the default sky-view factor in the UCM.

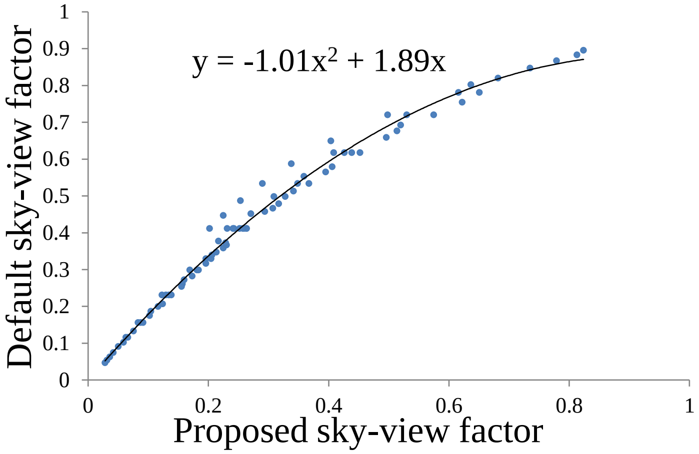

Figure B-1 Comparison of sky-view factor derived from the default UCM and the proposed update from section 3.3.3

C. The Single-layer Urban Canopy Model by Kusaka et al. (2001)

The model description of the single-layer urban canopy model proposed by Kusaka et al. (2001) is summarized herein. This section include excerpts of the following interactions modelled within or directly above the urban canopy: sensible heat flux, wind speed in the canyon, and surface temperatures. The model assumes a representative infinitely uniform street canyon for a model grid. The parameterization of solar fluxes and longwave fluxes is left for the readers to refer to Kusaka et al. (2001).

1. Sensible heat flux

Sensible heat flux from the building roof, building wall, and road was estimated at each surface separately. The equations are,

$$H_W = C_W\left(T_W - T_S\right), \tag{C-1}$$

$$H_G = C_G\left(T_G - T_S\right). \tag{C-2}$$

If $U_S > 5\,\mathrm{m\,s^{-1}}$ then,

$$C_W = C_G = 7.51U_S^{0.78}, \tag{C-3}$$

else,

$$C_W = C_G = 6.15 + 4.18U_S\,. \tag{C-4}$$

Here, T_W and T_G are surface temperatures at the wall and road, respectively. T_S is the replaced canyon surface temperature defined at a certain height within a canopy and above the displacement height. The U_S is the wind speed at z_o + d. The sensible heat exchange between the canyon space and the overlaying atmosphere is the heat flux through the canyon top, and is,

$$H_a = \rho c_p \frac{ku_*}{\psi_h}\left(T_S - T_a\right). \tag{C-5}$$

Here, u_* is the friction velocity and k is the Von Karman constant, ρ and c_p are the air density at the reference height and the heat capacity of dry air, respectively. Ψ_h is the integrated universal function,

$$\psi_h = \int_{\varsigma_T}^{\varsigma'} \frac{\phi_h}{\varsigma'} \mathrm{d}\varsigma', \tag{C-6}$$

where $\varsigma_T = z_T / L$ and $\varsigma = \left(z_a - d\right)/ L$ and L is the Obukhov stability length, computed from iterations.

The sensible heat flux from the building wall H_W and from the road H_G must be balanced by the sensible heat flux to the atmosphere from the canyon space. In other words, the total heat flux to the atmosphere from the urban area is the area-weighted average from the roof and that through the canyon top. If the ground surface area is classified into urban and vegetated with specific area ratios, the total heat fluxes at the grid points are the averaged heat fluxes weighted by their areas.

2. Wind speed

The mean wind speed in the canyon was used as a reference to calculate H_G and H_W. The wind speeds at the roof level U_r and within the canyon U_S are

$$U_r = U_a \frac{\psi_{mr}}{\psi_m}, \tag{C-7}$$

and

$$U_S = U_r \, exp\left(-0.386\frac{h}{w}\right). \tag{C-8}$$

Here, *h* and *w* are the normalized building height and width, respectively. The integrated universal functions above are calculated using

$$\psi_m = \int_{\varsigma_0}^{\varsigma'} \frac{\phi_m}{\varsigma'} \mathrm{d}\varsigma', \tag{C-9}$$

$$\psi_{mr} = \int_{\varsigma_0}^{\varsigma'} \frac{\phi_m}{\varsigma'} \mathrm{d}\varsigma', \tag{C-10}$$

$$\psi_r = (z_r - d)/L \tag{C-11}$$

3. Surface temperatures

The ground heat flux $G_{Z,I}$ and interior temperature $T_{Z,i}$ at the depth *z* to the *i* surface are calculated by the following equations,

$$G_{z,i} = -\lambda_i \frac{\partial T_{z,i}}{\partial z}, \tag{C-12}$$

and

$$\frac{\partial T_{z,i}}{\partial z} = -\frac{1}{\rho_i c_i}\frac{\partial G_{z,i}}{\partial z}. \tag{C-13}$$

The λ_i is the interior thermal conductivity and $\rho_i c_i$ is volumetric heat capacity that are specific to surface *i*. The subscript *i* indicates roof, wall, or road.

Acknowledgments

Special thanks to my very supportive supervisor, Prof. Manabu Kanda, for the continual support and enthusiasm for research. I also owe the success to my mentor, Prof. Makoto Nakayoshi. His supervision was the reason for the smooth progress of research. Their knowledge and experience is indeed an inspiration. Finally, I dedicate this dissertation to my family, my friends in the laboratory and outside, my girlfriend, the Kanda laboratory staff, and most especially to God.

This research was supported by the Research Program on Climate change Adaptation (RECCA) Fund from the Ministry of Education, Culture, Sports, Science and Technology (MEXT) of Japan and the Grant-in-Aid for Scientific Research (A): 25249066

References

Abbe C (1901) The physical basis of long-range weather forecasts, Mon. Weather Rev. 29, pp. 551 – 561

Arakawa H (1937) Increasing air temperatures in large developing cities, Beitr. Geophys., 50(1937), pp. 3 – 6

Burian SJ, Brown MJ, Linger SP (2002) Morphological analysis using 3D building databases. Los Angeles, California. Los Alamos National Laboratory, LA-UR-02-0781,73

Burian SJ, Ching JK (2009) Development of Gridded Fields of Urban Canopy Parameters for Advanced Urban Meteorological and Air Quality Models. U.S. Environmental Protection Agency, Washington, DC, EPA/600/R-10/007,2009

Burian, S.J., Han, W.S., (2003) Morphological analyses using 3D building databases: Houston, Texas. Los Alamos National Laboratory Rep. LA-UR-03-8633

Burian, S.J., Velugubantla, S.P., Maddula, S.R.K., (2003) Development of gridded fields of urban canopy parameters for models-3/CMAQ/MM5. EPA Internal Rep. for Contract PO-2D-6217-NTEX, 89

Carlton, T.N., Ripley, D.A., (1997) On the relation between NDVI, fractional vegetation cover, and leaf area index. *Remote Sensing of Environment*, 62, 241 – 252.

Changnon, S.A., (1973) Inadvertent Weather and Precipitation Modification by Urbanization. Journal of the Irrigation and Drainage Division, Vol. 99, No. 1, pp. 27 – 41.

Chen F, Janjić Z, Mitchell K (1997) Impact of Atmospheric Surface-layer Parameterisations in the new Land-surface scheme of the NCEP Mesoscale Eta Model. Boundary-Layer Meteorol 85: 391-421.

Chen F, Miao S, Tewari M, Bao JW, Kusaka H (2011a) A numerical study of interactions between surface forcing and sea breeze circulations and their effects on stagnation in the greater Houston area. J Geophys Res-Atmos (1984-2012) 116: 27. DOI: 10.1029/2010JD015533

Chen F, Kusaka H, Bornstein R, Ching J, Grimmond CSB, Grossman-Clarke S, Loridan T, Manning KW, Martilli A, Miao S, Sailor D, Salamanca FP, Taha H, Tewari M, Wang X, Wyszogrodzki AA, Zhang C (2011b) The integrated WRF/urban modelling system: development, evaluation, and applications to urban environmental problems. Int J Climatol 31: 273-288. DOI: 10.1002/joc.2158

Childs PP, Raman S (2005) Observations and Numerical Simulations of Urban Heat Island and Sea Breeze Circulations over New York City. Pure appl. geophys. 162: 1955-1980. DOI: 10.1007/s00024-005-2700-0

Ching J, Brown M, McPherson T, Burian S, Chen F, Cionco R, Hanna A, Hultgren T, Sailor D, Taha H, Williams D (2009) National Urban Database and Access Portal Tool. B Am Meteorol Soc 90: 1157-1168. DOI: http://dx.doi.org/10.1175/2009BAMS2675.1

Ching JKS (2013) A perspective on urban canopy layer modelling for weather, climate and air quality applications. Urban Climate 3: 13-39. DOI: http://dx.doi.org/10.1016/j.uclim.2013.02.001

Ching, J., Brown, M., McPherson, T., Burian, S., Chen, F., Cionco, R., Hanna, A., Hultgren, T., Sailor, D., Taha, H., Williams, D. (2009) National Urban Database and Access Portal Tool, *Bull. Amer. Meteor. Soc.*, 90, pp. 1157 – 1168

Chuan-Yao L, Chen F, Huang JC, Chen WC, Liuo YA, Chen WN, Liu SC (2008) Urban heat island effect and its impact on boundary layer development and land-sea circulation over northern Taiwan. Atmos Environ 42: 5635-5649. DOI: http://dx.doi.org/10.1016/j.atmosenv.2008.03.015

Corpetti T, Planchon O (2011) Front detection on satellite images based on wavelet and evidence theory: Application to the sea breeze fronts. Remote Sensing of Environment 115: 306-324. DOI: http://dx.doi.org/10.1016/j.rse.2010.09.003

Damato F, Planchon O, Dubreuil V (2003) A remote sensing study of the inland penetration of sea breeze fronts from the English channel. Weather 58(6): 219-226. DOI: 10.1256/wea.50.02

Dandou A, Tombrou M, Soulakellis N (2009) The Influence of the City of Athens on the Evolution of the Sea-Breeze Front. Boundary-Layer Meteorol 131(1): 35-51 DOI: 10.1007/s10546-008-9306-x

Ek, M.B., Mitchell, K.E., Lin Y., Rogers, E., Grunmann, P., Koren, V., Gayno, G., and Tarpley, J.D., (2003) Implementation of Noah land surface model advances in the National Centers for Environmental Prediction operational mesoscale Eta model, J. Geophys. Res., 103(D22), 8851, doi:10.1029/2002JD003296

Flagg DD, Taylor PA (2011) Sensitivity of mesoscale model urban boundary layer meteorology to the scale of urban representation. Atmos Chem Phys 11: 2951-2972. DOI: 10.5194/acp-11-2951-2011

Fujibe F (2011) Review Urban Warming in Japanese cities and its relation to climate change monitoring. Int J Climatol 31: 162-173. DOI: 10.1002/joc.2142

Grimmond S, and Oke T (1999) Aerodynamic properties of urban areas derived from analysis of surface form. J. Applied Meteorology 38: 1262-1292. DOI: http://dx.doi.org/10.1175/1520-0450(1999)038<1262:APOUAD>2.0.CO;2

Inoue T, Kimura F (2004) Urban effects on low-level clouds around the Tokyo metropolitan area on clear summer days. Geophysical Research Letters 31: L05103. DOI: 10.1029/2003GL018908

Kanda M, Inagaki A, Miyamoto T, Gryschka M, Raasch S (2013) A New Aerodynamic Parameterisation for Real Urban Surfaces. Boundary-Layer Meteorol 148: 357-377. DOI: 10.1007/s10546-013-9818-x

Kanda M, Inoue Y, Uno I (2001) Numerical Study On cloud Lines Over An Urban Street In Tokyo. Boundary-Layer Meteorol, 98, 251-273

Kanda M, Kawai T, Nakagawa K (2005a) A Simple Theoretical Radiation Scheme For Regular Building Arrays. Boundary-Layer Meteorol, 114, 71-90

Kanda M, Moriwaki R, Kimoto Y (2005b) Temperature Profiles Within And Above An Urban Canopy. Boundary-Layer Meteorol 115: 499-506. DOI: 10.1007/s10546-004-5644-5

Kanda M, Kawai T, Kanega M, Moriwaki R, Narita K, Hagishima A (2005c) A Simple Energy Balance Model For Regular Building Arrays. Boundary-Layer Meteorol 116: 423-443. DOI:10.1007/s10546-004-7956-x

Kanda M, Moriwaki R, Kasamatsu F (2006) Spatial Variability of Both Turbulent Fluxes and Temperature Profiles in an Urban Roughness Layer. Boundary-Layer Meteorol 121: 339-350. DOI: 10.1007/s10546-006-9063-7

Kawai T, Ridwan MK, Kanda M (2009) Evaluation of the Simple Urban Energy Balance Model Using Calculated Data from 1-yr Flux Observations at Two Cities. J Appl Meteorol Climatol 48: 693-715. DOI: http://dx.doi.org/10.1175/2008JAMC1891.1

Khiem M, Ooka R, Hayami H, Yoshikado H, Huang H, Kawamoto H (2010) Process analysis of ozone formation under different weather conditions over the Kanto region of Japan using the MM5/CMAQ modelling system. Atmos Environ 44: 4463-4473. DOI: http://dx.doi.org/10.1016/j.atmosenv.2010.07.038

Kim YH, and Baik JJ (2005) Spatial and Temporal Structure of the Urban Heat Island in Seoul. J Appl Meteorol 44: 591-605. DOI: http://dx.doi.org/10.1175/JAM2226.1

Kim Y, Sartelet K, Raut Jean-Christopher, Chazette, P (2013) Evaluation of the Weather Research and Forecast/Urban Model Over Greater Paris. Boundary-layer Meteorol 149:105 – 132

Kondo H, Genchi Y, Kikegawa Y, Ohashi Y, Yoshikado H, Komiyama H (2005) Development of a multi-layer urban canopy model for the analysis of energy consumption in a big city: structure of the urban canopy model and its basic performance. Boundary-layer Meteorol 116: 395-421. DOI: 10.1007/s10546-005-0905-5

Kondo H, Tokairin T, Kikegawa Y (2008) Calculation of wind in a Tokyo urban area with a mesoscale model including a multi-layer urban canopy model. J Wind Eng Ind Aerodyn 96: 1655-1666. DOI: http://dx.doi.org/10.1016/j.jweia.2008.02.022

Kusaka H, Kondo H, Kikegawa Y, Kimura F (2001) A Simple Single-Layer Urban Canopy Model For Atmospheric Models: Comparison With Multi-Layer and Slab Models. Boundary-Layer Meteorol 101: 329-358. DOI: 10.1023/A:1019207923078

Kusaka H., Kimura F. (2004) Coupling a single-layer urban canopy model with a simple atmospheric model: impact on urban heat island simulation for an idealized case. Journal of the Meteorological Society of Japan, 82, pp. 67 – 80

Lo JCF, Lau AKH, Chen F, Fung JCH, and Leung KKM (2007) Urban modification in a mesoscale model and the effects on the local circulation in the Pearl River Delta region. J Appl Meteorol Climatol 46: 457-476.

Lynch, P. (2008) The origins of computer weather prediction and climate modelling, Vol. 227, No. 7, pp. 3431 – 3444.

Macdonald RW, Griffiths RF, Hall DJ (1998) An improved method for the estimation of surface roughness of obstacle arrays. Atmos Environ 32: 1857-1864. DOI: http://dx.doi.org/10.1016/S1352-2310(97)00403-2

Martilli A (2003) A Two-Dimensional Numerical Study of the Impact of a City on Atmospheric Circulation and Pollutant Dispersion in a Coastal Environment. Boundary-Layer Meteorol 108: 91-119. DOI: 10.1023/A:1023044100064

Martilli A, Clappier A, Rotach MW (2002) An urban surface exchange parameterisation for mesoscale models. Boundary-Layer Meteorol 104: 261-304. DOI: 10.1023/A:1016099921195

Matsuoka, S. (2007), The TSUBAME Cluster Experience a Year Later, and onto Petascale TSUBAME 2.0, Proceedings of the 14th European PVM/MPI User's Group Meeting on Recent Advances in Parallel Virtual Machine and Message Passing Interface, pp. 8 – 9

Miao S, Chen F, LeMone MA, Tewari M, Li Q, Wang Y (2009) An observational and modeling study of characteristics of urban heat island and boundary layer structures in Beijing, J Appl Meteorol 48: 484-501. DOI: http://dx.doi.org/10.1175/2008JAMC1909.1

Moriwaki R, Kanda M, Senoo H, Hagishima A, Kinouchi T (2008) Anthropogenic water vapor emissions in Tokyo. Water Resour Res 44: W11424. DOI: 10.1029/2007WR006624

Nakayoshi M, Kanda M, Shi R, De Dear R (in preparation) Experiment of outdoor thermal physiology along human pathway using wearable measurement system. for submission

Ohashi Y, Kida H (2002) Numerical Experiments on the Weak-Wind Region Formed Ahead of the Sea-Breeze Front. J Meteorol Soc Jpn 80: 519-527

Oke TR (1973) City size and the urban heat island. Atmos Environ, Volume 7, Issue 8, August 1973, Pages 769-779, ISSN 0004-6981, 10.1016/0004-6981(73)90140-6.

Prtenjak MT (2002) Idealised Numerical Simulations of Aerodynamic Roughness Length Effects on Sea Breeze Characteristics. Proceedings Second Conference on Air Pollution Modelling and Simulation, APMS'01 Champs-sur-Marne, April 9-12, 2001. Air Pollution Modelling and Simulation. 553-556

Salamanca F, Martilli A, Tewari M, Chen F (2011) A Study of the Urban Boundary Layer Using Different Urban Parameterisations and High-Resolution Urban Canopy Parameters with WRF. J App Meteorol Climatol 50: 1107-1128. DOI: http://dx.doi.org/10.1175/2010JAMC2538.1

Sato T, Murakami S, Ooka R, Yoshida S (2008) Analysis of regional characteristics of the atmospheric heat balance in the Tokyo metropolitan area in summer. J Wind Eng Ind Aerod 96: 1640-1654. DOI: http://dx.doi.org/10.1016/j.jweia.2008.02.004

Shafir, H. and Alpert, P., (1989) On the Urban Orographic Rainfall Anomaly in Jerusalem – A Numerical Study. Atmos Environ 24B(3):365 – 375

Skamarock WC, Klemp JN, Dudhia J, Gill DO, Barker DM, Wang W, Powers JG (2005) A description of the Advanced Research WRF Version 2. NCAR Tech Notes-468+STR

Sugawara H, Narita K, Mikami T (2004) Representative Air Temperature of Thermally Heterogeneous Urban Areas Using the Measured Pressure Gradient. J Appl Meteorol 43: 1168-1179. DOI: http://dx.doi.org/10.1175/1520-0450(2004)043<1168:RATOTH>2.0.CO;2

Tewari, M.F., Chen, F., Kusaka, H., Miao, S. (2008) Coupled WRF/Unified Noah/urban-canopy modelling system, NCAR WRF Documentation, NCAR, Boulder, pp. 1 – 20.

Tso CP (1996) A survey of urban heat island studies in two tropical cities. Atmos Environ 30: 507-519. DOI: 10.1016/1352-2310(95)00083-6

Wang, Z.H., Bou-Zeid, E., Smith, J.. (2012) A coupled energy transport and hydrological model for urban canopies evaluated using a wireless sensor network. *Q. J. R. Meteorol. Soc.* 139, 1643 – 1657

Warner, T.T., (2011)Numerical Weather and Climate Prediction, Cambridge University Press, Cambrige, UK. ISBN: 987-0-521-51389-0. Hardback, 526 PP.

Williams CN, Basis A, Peterson TC (2000) Calibration and Verification of Land Surface Temperature Anomalies Derived from the SSM/I. B Am Meteorol Soc 81: 2141-2156. DOI: http://dx.doi.org/10.1175/1520-0477(2000)081<2141:CAVOLS>2.3.CO;2

Yamashita S (1996) Detailed structure of heat island phenomena from moving observations from electric tram-cars in metropolitan Tokyo Atmos Environ, 30 (3), pp. 429 – 435

Yoshikado H, Kondo H (1989) Inland penetration of the sea breeze over the suburban area of Tokyo. Boundary-Layer Meteorol 48: Issue 4, 389-407. DOI: 10.1007/BF00123061

下重　亮，仲吉信人，神田　学：都市要因を考慮した夏季関東における都市型集中豪雨の多事例解析，水工学論文集，第 54 巻，349-354．2010

仲野久美子，仲吉信人，Alvin C.G. Varquez，神田　学，足立幸穂，日下博幸：最新の都市パラメタリゼーションを導入した集中豪雨シュミレーション，　土木学会論文集 B1(水工学)，69 巻，4 号，I335-I360，2013

真壁拓也，仲吉信人，Varquez, A.C.G.，神田学：気象解析のための全日本都市幾何データベースの構築と世界への拡張可能性，土木学会論文集 B1（水工学），Vol.70，No.4，I_325-I_330，2014